**DEPARTMENT OF ELECTRIC DRIVES AND TRACTION**

## CZECH TECHNICAL UNIVERSITY IN PRAUE

**FACULTY OF ELECTRICAL ENGINEERING**

## DESIGN AND CONSTRUCTION OF WIRELESS CHARGER FOR CTU SPACE RESEARCH

**MASTER THESIS**

**MAY 2023**

**ADAM PEŠEK**

# ZADÁNÍ DIPLOMOVÉ PRÁCE

## I. OSOBNÍ A STUDIJNÍ ÚDAJE

| | | | |
|---|---|---|---|
| Příjmení: | **Pešek** | Jméno: **Adam** | Osobní číslo: **475377** |

Fakulta/ústav: **Fakulta elektrotechnická**

Zadávající katedra/ústav: **Katedra elektrických pohonů a trakce**

Studijní program: **Elektrotechnika, energetika a management**

Specializace: **Elektrické pohony**

## II. ÚDAJE K DIPLOMOVÉ PRÁCI

Název diplomové práce:

**Návrh a realizace bezdrátové nabíječky pro CTU Space Research**

Název diplomové práce anglicky:

**Design and Construction of Wireless Charger for CTU Space Research**

Pokyny pro vypracování:

1) Proveďte studii literatury a dostupných technických podkladů k problematice bezkontaktního přenosu.
2) Navrhněte systémovou architekturu založenou na standardu Qi, která by umožňovala přenos výkonu 30 W a obousměrnou komunikaci.
3) Proveďte návrh obvodového řešení a programového vybavení.
4) Navrhněte testovací přípravek, který by bylo možné zabudovat do rakety navrhované CTU Space Research.
5) Ověřte navržené řešení.

Seznam doporučené literatury:

[1] The Wireless Power Consortium, "Qi Specification, Communications Protocol," Version 1.3, 2021.
[2] G. A. Covic and J. T. Boys, "Inductive Power Transfer," Proc. IEEE, vol. 101, no. 6, pp. 1276–1289, Jun. 2013.
[3] Z. Zhang, H. Pang, A. Georgiadis, and C. Cecati, "Wireless Power Transfer - An Overview," IEEE Trans. Ind. Electron., vol. 66, no. 2, pp. 1044–1058, Feb. 2019.
[4] M. Košík, "Bifurcation Analysis and Control Methods for Inductively Coupled Power Transfer", PhD Thesis, CTU in Prague, Nov. 2021.

Jméno a pracoviště vedoucí(ho) diplomové práce:

**Ing. Michal Košík, Ph.D.     katedra elektrických pohonů a trakce   FEL**

Jméno a pracoviště druhé(ho) vedoucí(ho) nebo konzultanta(ky) diplomové práce:

Datum zadání diplomové práce: **31.01.2023**     Termín odevzdání diplomové práce: **26.05.2023**

Platnost zadání diplomové práce: **22.09.2024**

_____          _____          _____
Ing. Michal Košík, Ph.D.                  podpis vedoucí(ho) ústavu/katedry          prof. Mgr. Petr Páta, Ph.D.
podpis vedoucí(ho) práce                                                                              podpis děkana(ky)

## III. PŘEVZETÍ ZADÁNÍ

Diplomant bere na vědomí, že je povinen vypracovat diplomovou práci samostatně, bez cizí pomoci, s výjimkou poskytnutých konzultací.
Seznam použité literatury, jiných pramenů a jmen konzultantů je třeba uvést v diplomové práci.

_____          _____
.
Datum převzetí zadání                              Podpis studenta

## ACKNOWLEDGEMENT

I want to thank my thesis advisor Ing. Michal Košík, Ph.D., and Ing. Pavel Skarolek, who taught me the necessary skills used during the work on this thesis. I would also like to thank the Department of Electric Drives and Traction for providing the financial support that allowed this thesis to participate in the student competition at IEEE WPTCE 2023. The last thanks belong to my family, who supported me throughout my studies.

## DECLARATION

I hereby declare that I have written my master thesis on my own and I have used only the literature listed at the end of the master thesis in the references.

Prague, 26. May 2023

.......................................................................................

# ABSTRAKT

Tato diplomová práce popisuje návrh a konstrukci bezdrátové nabíječky pro raketu inspirované Standardem Qi. Účelem bezdrátové nabíječky je dobíjení akumulátoru v raketě a zprostředkování komunikace mezi hlavní řídící jednotkou rakety a pozemní stanicí. Projekt rakety je více popsán v úvodu této práce.

Dále je uveden stručný přehled technologie induktivního bezdrátového přenosu s důrazem na systémy s proměnlivou frekvencí a Standard Qi.

Koncepční část popisuje klíčové funkční bloky bezdrátové nabíječky pomocí systémové a softwarové architektury a analyzuje provozní stavy zařízení. Představen je i počáteční 3D model bezdrátové nabíječky.

Koncept je realizován v části implementace, kde jsou jednotlivé funkční bloky implementovány ve skutečném zařízení.

Funkce zkonstruované bezdrátové nabíječky je ověřena pomocí několika testovacích scénářů a měření.

Výsledky této práce jsou diskutovány v poslední kapitole této práce.

**Klíčová slova:** bezdrátové nabíjení, Qi Standard, aerokosmické aplikace, induktivní bezdrátový přenos, diplomová práce

# ABSTRACT

This diploma thesis describes designing and constructing a Qi-inspired wireless charger for a rocket. The purpose of the wireless charger is to charge the rocket's battery pack and mediate communication between the main MCU of the rocket and the ground station. The rocket project is described more at the beginning of this thesis.

Next, a brief overview of IPT technology focusing on variable frequency systems and the Qi Standard is presented.

The design concept section describes the key functional blocks of the wireless charger using system and software architecture and analyzes the operating states of the device. Additionally, an initial 3D model of the wireless charger is presented.

The design concept is realized in the implementation part, where the functional blocks are implemented in a real device.

The operation of the constructed wireless charger is verified using several testing scenarios and measurements.

The obtained results are discussed in the last chapter of this thesis.

**Keywords:** Wireless Charging, Qi Standard, Aerospace Industry, Inductive Power Transfer, Master Thesis

# LIST OF CONTENT

## LIST OF FIGURES

# LIST OF TABLES

# 1 INTRODUCTION

Inductive Power Transfer (IPT) technology has gained significant popularity in various domains. It finds applications in low-power devices like consumer and industrial electronics and high-power systems such as electric vehicle charging [1], [2].

This thesis focuses on exploring the potential of IPT in the aerospace industry by designing and constructing a wireless charger for a rocket. Additionally, the project presented in this thesis validates a novel optimization procedure for variable frequency IPT systems, which is thoroughly described in a subsequent paper and will be presented together with this project at IEEE WPTCE 2023 [3].

The rocket is being developed by CTU Space Research, a student team, for the European EUROC competition. The author's contribution to the rocket project involves the hardware and software design as well as the construction of the IPT System. This system consists of a Power Transmitter, part of the Ground Station, and a Power Receiver, part of the rocket. The proposed IPT system ensures both the charging of the rocket's battery pack and the secure transfer of data between the Head Unit and the Ground Station until liftoff. Note that capital letters distinguish specific modules, components, or concepts. For clarity, the capital letters will be used throughout the rest of this text.

To facilitate our work, we have decided to base the design of the IPT system on the existing Qi Standard for IPT. The Qi Standard is a widely adopted IPT standard primarily used in consumer electronics. Since the wireless charger will be used exclusively for this specific application, we have omitted certain standard features to simplify the implementation.

## 1.1 Description of the Rocket Project

The newly developed rocket aims to elevate to an altitude of 3 km, conduct scientific experiments and return safely to the surface. The first experiment uses a specially designed device to collect air samples at different altitudes during the descent. These captured air samples will be analyzed for the presence of microbes in the different atmospheric layers, such as bacteria and fungi or other species capable of surviving in adverse conditions and spreading over long distances. The second experiment aims to expose the selected microbes to high levels of acceleration and general conditions prevailing at high altitudes and observe how this condition affects the physiology and metabolism of these microorganisms.

The rocket is powered by a hybrid rocket engine of its own design, using 3D-printed fuel made from ABS material and nitrous oxide as the oxidizer. The planned thrust of the engine is approximately 1.25 kN, with a burn-time of slightly over 10 seconds. The rocket has an overall height of 4 meters and an outer diameter of 160 mm. The rocket shell is made of 2 mm thick glass fiber. The rocket body is divided into individual segments connected using the RADAX joint system, allowing for easy detachment, transport, and customization of the entire structure.

The long-term objective of CTU Space Research is to develop a reliable platform capable of delivering CubeSats to low Earth orbit.

## 1.2 Motivation

The proposed wireless charger aims to replace the solution from the previous version of the rocket. The previous approach, as illustrated in Fig. 1 (b and c), involved cable connectors housed beneath a flip-up cover within the rocket shell. The connectors were used for both charging and communication purposes.

The primary challenges associated with the cable connections are as follows:
1. Human intervention is required to plug and unplug the cables before the rocket's launch, which represents a safety risk given the presence of preheated explosive rocket fuel. Additionally, the Rules & Requirements of EUROC forbid the presence of any person from the engineering crew at the launch site during the launch [4].

2. Another alternative is to let the rocket detach the cables using drag force during launch. However, this may impact the flight path, creating an additional problem.
3. Implementing the flip-up cover and cable connectors requires modification to the rocket's structure, reducing the rocket shell's overall firmness and rigidity and negatively impacting the aerodynamics.



(a)                                    (b)                                    (c)
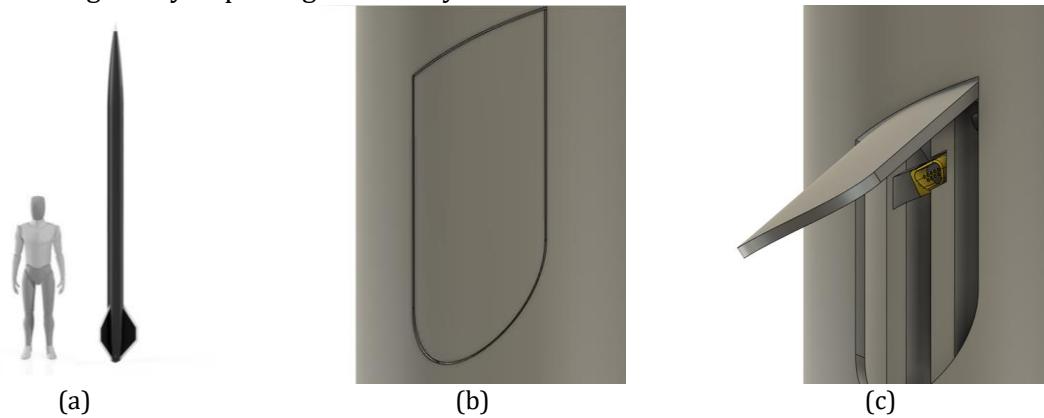
Fig. 1 The 3D Model of the Rocket a) Size Comparison (b) The flip-up cover in the rocket shell (c) Exposed connectors under the cover. The pictures were provided by CTU Space Research.

The designed wireless charger addresses the issues listed above while simultaneously integrating power transfer and communication into a single device. Human intervention is unnecessary since the whole charging process can be controlled remotely. The power transfer will occur through the rocket shell, obviating the need to penetrate it, which improves the rocket shell's firmness and aerodynamics.

## 1.3    Project Requirements

In the project's initial phase, requirements for the designed device were discussed with the CTU Space Research team members. As a result, a comprehensive set of requirements and a project schedule were established. The main project objectives are the following.

1. The wireless charger shall maintain a constant DC voltage of 30 V on the receiver's output.
2. The receiver's nominal output power shall be 30 W, maximal 35 W, and minimal 1.5 W, which is 5 % of the nominal output power).
3. The rocket's battery management system (BMS), which is not part of the designed wireless charger, shall control the charging process. BMS shall give the commands to the wireless charger to start and end charging.
4. The wireless charger shall transfer the data between the Head Unit (main MCU of the rocket) and the Ground Station (PC located on the ground station). The communication canal between the rocket and the Ground Station shall be controlled from the Ground Station. The Ground Station shall initiate the power transfer and open a communication canal to transfer the flight data or adjust the settings of the rocket's system. The Ground Station shall send a final command for the safe termination of power transfer and removal of the transmitter to a safe distance from the rocket.
5. The Receiver shall be powered from the same series of accumulators which power the main head unit of the rocket. The accumulators are 2 LiFePo cells connected in series with a nominal voltage of 7.4 V DC. The Transmitter shall be powered from the power supply located at the liftoff platform with a DC voltage of 48 V.
6. The maximal weight of the receiver shall not exceed 250 grams.

# 2     THEORETICAL BACKGROUND OF WIRELESS POWER TRANSFER

This section briefly overviews wireless power transfer technology (WPT), specifically focusing on inductive power transfer. It starts with an introduction to the history of WPT and its general classification. Then, the typical structure of a wireless charger is presented, highlighting important components like coil pads and compensation circuits. An equivalent circuit model is introduced to explain the physical processes and functionality of the wireless charger. The optimization method used to determine the key parameters of the wireless charger is described. Finally, a brief introduction to the Qi Standard, which inspired the proposed wireless charger, is provided.

## 2.1     History of WPT

The history of wireless power transfer is closely tied up with discovering the fundamentals of electromagnetics. Thus, the first demonstration of WPT can be dated to the discovery of the relationship between current and magnets by André-Marie Ampère in 1826 and the electromotive force driving a current in a conductor loop by a time-varying magnetic flux by Michael Faraday in 1831. Since then, several demonstrations of wireless transmission of electrical energy have been carried out. However, a coherent theory unifying electricity and magnetism was not published until the 1860s when James Clerk Maxwell wrote A Dynamical Theory of the Electromagnetic Field, known for the famous Maxwell's equations [5], [6].

However, Maxwell's equations were validated 28 years later, in 1888, when Heinrich Hertz and the University of Berlin produced an apparatus capable of generating and detecting electromagnetic waves in the microwave spectrum. Several successful experiments with pulsed wireless energy transfer proved the validity of Maxwell's equations [7].

However, the first actual application of wireless power transfer was introduced by Nikola Tesla in 1891 when he patented the famous Tesla coil, which can be classified as the first resonant transformer with inductive and capacitive coupling [6]. Nikola Tesla introduced a series of demonstrations of wireless power transfer, for example, powering the lighting systems at the Columbian Exposition in the 1893 Chicago World Fair. [8] Through resonant inductive coupling, Tesla discovered that he could increase the range at which a lamp could be powered by tuning receiving LC circuit to resonance with the transmitter LC circuit. At the time, Tesla was unable to develop a commercial product from his discovery, however, the resonant coupling of LC circuits in transmitter and receiver is used in all inductive power transfer (IPT) systems as described in 2.3 [5], [8].

## 2.2     General Classification of WPT

WPT technology allows power to be transmitted from a power source to an electrical load without physical contact. This technology has gained significant attention due to its potential for providing wireless charging solutions for various applications, ranging from consumer electronics to electric vehicles.

Several factors can classify WPT, such as the type of energy transferred, the distance between the transmitter and receiver, and the method of energy transfer. However, a typical classification of a wireless power transfer using the electromagnetic field is into two main types, namely far-field and near-field power transfer. Far-field power transfer, or radiative power transfer, uses electromagnetic waves to transfer energy over long distances. This type of power transfer is mainly used in long-range applications, such as powering remote sensors or charging electric vehicles wirelessly [2], [9].

Far-field WPT operates in the microwave frequency range (typically between 300 MHz and 300 GHz), which enables energy to be transferred over long distances. This method uses directional antennas to focus the electromagnetic waves onto the receiving device. However, due to the inverse-square law, the amount of energy transferred decreases rapidly as the distance between the transmitter and receiver increases. Therefore, far-field WPT is less efficient than

near-field power transfer and is mainly used for applications that require low power transfer rates [10].

Near-field-based WPT can be further divided into capacitive and inductive power transfer. Capacitive Power Transfer (CPT) uses an electric field to transfer energy between two pairs of electrodes separating the transmitter and the receiver. Between the electrodes, typically consisting of two metal plates, is a dielectric in the form of an air gap, and together form a capacitor. The transmitter generates an alternating voltage that is applied to the transmitting plate. An alternating voltage is induced on the receiver plate through electrostatic induction. This induction causes an alternating current to flow in the load circuit. The CPT is not commonly used due to the hazardous high voltages on the electrodes, the interaction of the electric field with its surroundings, and generally its low efficiency and limited range [2], [11], [12].

Inductive Power Transfer (IPT) is the most widely used technology for WPT due to its numerous advantages. IPT uses magnetic fields to transfer power wirelessly, making it a safer option than CPT because magnetic fields are non-ionizing, and overall operating voltages within the IPT system are lower. Additionally, IPT is highly efficient, achieving up to 95% efficiency [13]. It is also highly scalable, transferring power over various power levels, from milliwatts to kilowatts [14]. Another advantage of IPT is that it can be designed to operate at higher frequencies, enabling the use of smaller and lighter components in the system. These benefits have made IPT the preferred method for near-field WPT used in a broad range of applications, including low-power devices such as consumer electronics and biomedical implants, as well as high-power devices like industrial automation and electric vehicle charging [2], [9], [10].

## 2.3    The Structure of IPT-Based Wireless Charger

The core of an IPT-based wireless charger is the charging pad equipped with a transmitter coil and the target device fitted with a receiver coil. An alternating current is applied to the transmitter coil, generating a magnetic flux that flows through the air gap and penetrates the receiver coil, inducing an AC voltage across the receiver coil terminals. The power transferred between the transmitter and receiver depends on the strength of the magnetic field and the coupling between the coils defined by the position of the coils. To reduce losses and thus maximize efficiency, resonant circuits are used in the form of the transmitter or the receiver coil and additional compensation [2], [15].

The typical structure of an IPT wireless charger is illustrated in a block diagram in Fig. 2. Based on the functionality, the standard wireless charger consists of the following parts:

- DC Power supply – provides an input DC voltage of the required voltage level with sufficient power. The power supply does not necessarily have to be a part of the wireless charger and can be a standalone device.
- Input filter – ensures input voltage stabilization and smoothest input current peaks.
- High-Frequency Inverter – converts the DC to AC voltage of the typically square waveform. The duty cycle and frequency of the square wave can vary with the transmitted power.
- The Resonant Circuits – one on the transmitter and the other on the receiver. The resonant circuits consist of the following:
    - o Transmitter/Receiver Coil - typically planar coils with a pad from a magnetic material and possibly a shielding
    - o Transmitter/Receiver Compensation – a capacitor connected in series or parallel to the coil forming a series or parallel resonant circuit.
- Rectifier – rectifies the AC voltage on the receiver's side induced in the resonant circuit.
- Output filter – stabilizes the output voltage to minimize the voltage ripple and filters the current peaks.

- Load – a battery with or without a dedicated battery management system (BMS) or other load types.
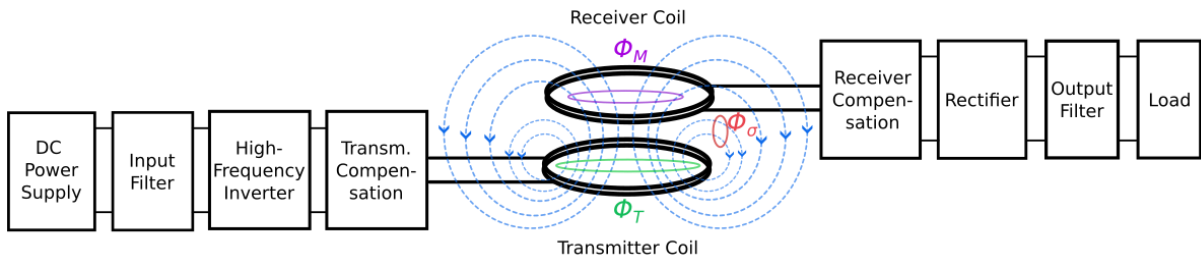


Fig. 2 Block Diagram of an IPT System. Blue dotted lines indicate magnetic flux paths. However, the direction is alternating.

In the following sections, the core parts of the wireless charger specific to the IPT system are widely described, namely the parts of the resonant circuits: the coils and the compensation topologies.

## 2.3.1 Coil pads

### 2.3.1.1 Coupling Coefficient

As depicted in Fig. 2, the magnetic flux generated by the transmitter coil $\phi_T$ is a sum of a mutual magnetic flux $\phi_M$ which links with the receiver coil and the leakage magnetic flux $\phi_\sigma$ which does not follow the particularly intended path. The proportion of the $\phi_T$ and the $\phi_M$ is known as the primary coupling coefficient (often shortened to only coupling coefficient) expressed by [16]:

$$k = \frac{\phi_M}{\phi_T} \tag{2-1}$$

The better the ratio of the mutual to leakage magnetic flux, the better the coils are coupled. The coupling factor achieves values from 0 to 1, where 1 represents the perfect coupling, i.e., all flux generated by the transmitter coil is linked with the receiver coil, and 0 represents a situation where transmitter and receiver coils are independent of each other [17]. The coupling factor depends strongly on the coil's position.

The coil's position can be expressed with axial and radial displacement and the angle between them. The axial distance (or simply the air gap) refers to the distance between the centers of the primary and secondary coils along the axis perpendicular to the plane of the coils. The radial distance, on the other hand, refers to the distance between the center of the transmitter coil and the center of the transmitter coil along a plane parallel to the coils. In the Fig. 3 we can see how the coupling coefficient differs with different radial and axial displacements (described by "zshift") [18].
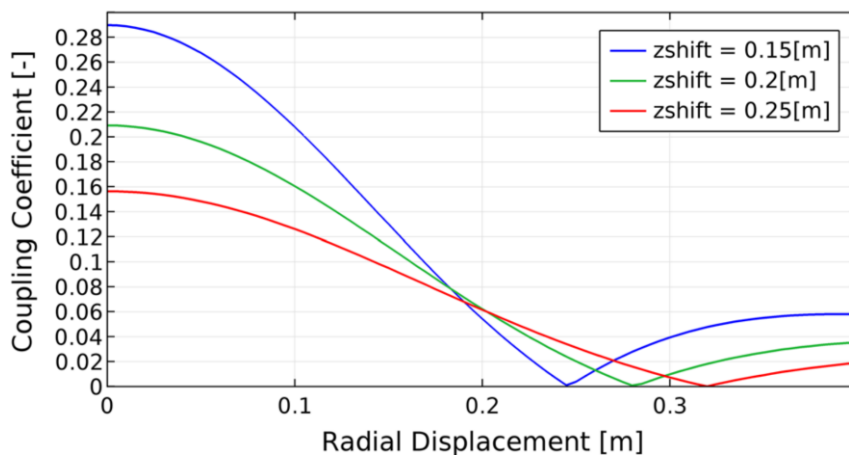


Fig. 3 Coupling coefficient dependency on radial displacement considering different axial displacements. Source [18].

The coupling factor is further determined by the coils' relative size and shape[17].

The equation (2-1) can be expressed as:

$$k = \frac{M}{\sqrt{L_p L_s}} \tag{2-2}$$

Where $M$ is the mutual inductance of the transmitter and receiver coil, $L_p$ and $L_s$ are self-inductances of transmitter and receiver coils, respectively.

### 2.3.1.2    Quality Factor

Considering the simplified version of the coil equivalent circuit model, the parameters of coils are given by their self-inductance and equivalent series resistance (ESR). Assuming the power supply providing the current to the coil is a purely sinusoidal AC source, both parameters can be expressed with a single one, the quality factor:

$$Q = \frac{\omega L}{R} \tag{2-3}$$

Where $\omega = 2\pi f$ is the circular frequency, $L$ is the self-inductance of the coil, and $R$ is the resistance of the coil, expressed as ESR.

The quality factor $Q$ can have a value between 0 and infinity. The higher the number, the higher the "quality" of the coil, i.e., the coil acts more as an inductor and less as a resistance. Although it is difficult to obtain values above 1000 for coils, most mass-produced coils used in IPT have values of $Q$ around 100. The quality factor value is dependent on the frequency. However, for a fixed operating frequency, the quality factor Q mainly depends on the shape and size of the coil and the materials used [19].

### 2.3.1.3    Ferrite and Aluminum Pads

Only standalone coils would be ineffective in terms of power transfer since the quality factor of such coils would be small. The magnetic core is added as a pad to minimize the leakage magnetic flux and increase the inductance of the coil by forcing the flux radiating on one side. This increases the coils' quality factors and thus increases the overall efficiency [20].

The magnetic pad is typically made of ferrite, and it is manufactured as one plate covering the whole coil or as multiple squares or stripes placed in various formations respecting the magnetic flux orientation. A ferrite is a ceramic material made from iron oxide and other metals such as nickel, zinc, manganese, or magnesium. It is a very fragile material that must be protected from possible damage [21].

The thickness of the ferrite pads is typically only a few millimeters since the ferrite has a large density, so the ferrite pad mostly gives the overall weight of the coil pad. However, by lowering the thickness of the ferrite pad, core losses increase, leading to reduced quality factor value of the coil pad. Additionally, by reducing the ferrite thickness, the coupling coefficient is reduced as well. Thus, choosing the thickness of the ferrite pad for the coil design is a balance of cost, efficiency, and robustness [22].

In some applications, an extra shielding (usually in the form of a thin aluminum or copper sheet) is placed on the ferrite pad (on the side where winding is not occurrent) to reduce EMC radiated to the coil's surroundings. However, the high conductivity of the metal sheets produces relevant eddy current losses, reducing the IPT system's efficiency[22], [23].

### 2.3.1.4    Arrangement of Coil Pads

In IPT, planar coils are typically used with one or more layers to optimize the coupling between the coils.  The coils are wound with Litz wire suitable for high frequencies, typically with polymer-based insulation between individual wires within the strand and additional possible insulating coating.

The coil arrangement can be found in various forms. Fig. 4 is a table of the most used coils arrangements and their pros and cons. The most common form is a circular pad where coils are wound in a circle, and the ferrite pad is also circular or square. This arrangement has low leakage

flux and high efficiency; however, it is prone to misalignment of coils. For that reason, it is widely used primarily on stationary applications. On the other hand, the arrangements with multiple coils are less prone to misalignment, but they often require multiple inverters for powering, e.g., Bi-Polar Pad, DDQ Pad, or Tri-Polar Pad [9].
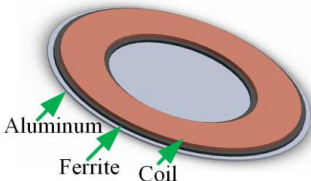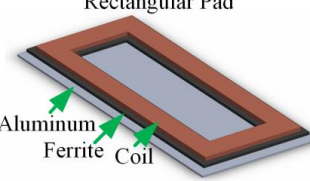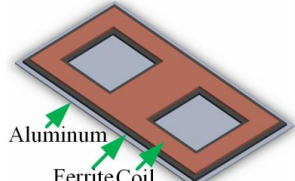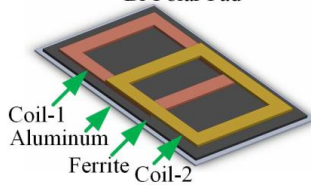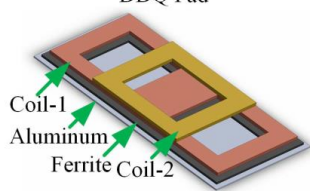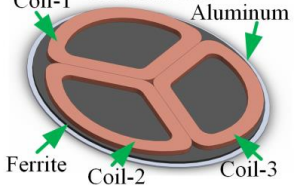


| Circular Pad | Rectangular Pad | DD Pad |
|---|---|---|
| A CP is the most common pad for stationary WPT applications due to high efficiency and low leakage field. | An RP is the most common pad for dynamic WPT applications due to its cost-effective and compact structure. | A DD pad generates a parallel flux component that offers higher tolerance to horizontal misalignment. DD pads can be either single-coil or multi-coil pads. |
| Bi-Polar Pad | DDQ Pad | Tri-Polar Pad |
| A BP pad is interoperable with other pads and offers good misalignment tolerance. In some designs with two independent windings, it requires two synchronized inverters for powering. | A DDQ pad is interoperable with other pads and offers good misalignment tolerance. In some designs with multiple windings, it requires two synchronized inverters for powering. | A TP pad demonstrates a higher coupling factor and lower leakage field compared to a CP. It requires three single-phase synchronized inverters or one three-phase inverter for powering. |

Fig. 4 Different Coil Pads Arrangements. Source [9].

### 2.3.2 Compensation Topologies

The resonant circuit design, formed by capacitors and the transmitter or receiver coil, is known as the compensation topology. Without this additional capacity forming the resonant circuit, power transfer efficiency would be low, and the VA ratings required for the same transferred power would be much higher. Additionally, the configuration of the resonance topology determines the voltage and current stress across semiconductor components, which also affects their rating. By forming the resonant circuit, the power supply's VA rating can be reduced, power transfer efficiency increased, and energy losses in the system minimized. To achieve high efficiency in IPT systems, the transmitter and receiver coils should operate at frequencies close to the common resonance frequency [24].

The arrangement of energy storage elements plays a significant role in shaping the size, order, and waveform. There are four main types of compensation topologies based on the placement of the compensation capacitor within the resonant circuit forming the series (S) or parallel (P) resonant circuit.

By varying the capacitor position, we get those four basic topologies: series-series (SS), series-parallel (SP), parallel-series (PS), and parallel-parallel (PP) [24].
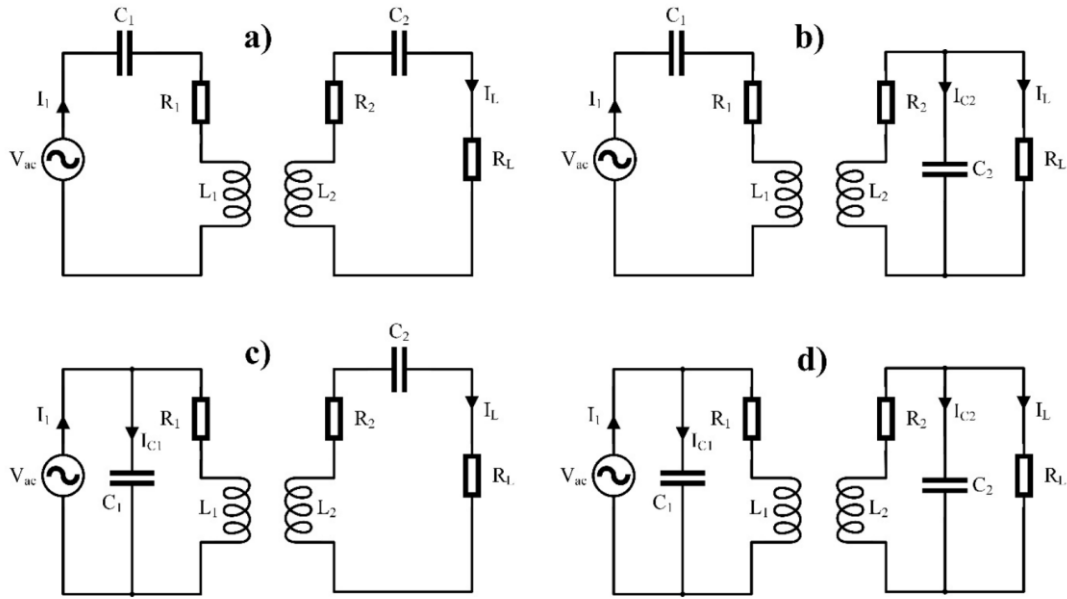
Fig. 5 Four basic compensation topologies a) SS, b) SP, c) PS, d) PP. Source [1].

The SS topology, characterized by the connection of the primary and secondary coils in series with a compensation capacitor, is ideal for applications with a wide load variation. It offers a stable transfer efficiency, even at low mutual inductances, and enables the transmission of the highest output power for a fixed input power. Consequently, this versatile topology finds application across various power levels.

In contrast, the SP topology features a series connection of the primary coil with a compensation capacitor and a parallel connection with the secondary coil. While it provides high power transfer efficiency, it demands a higher input power than the SS topology. Moreover, the primary capacitance relies on the coupling coefficient and load resistance, affecting both resonance frequency and transfer efficiency. Hence, this topology suits less-power applications.

For the PS topology, the primary coil is connected in parallel with a compensation capacitor, and the secondary coil is connected in series with a compensation capacitor. Similar to the SP topology, the primary capacitance depends on the coupling coefficient and load resistance, impacting resonance frequency and transfer efficiency. However, this topology is exclusively used in high-power applications.

Lastly, the PP topology involves parallel connections of both primary and secondary coils with a compensation capacitor. The primary capacitance is also influenced by the coupling coefficient and load resistance, affecting resonance frequency and transfer efficiency. While this topology provides the lowest power transfer efficiency among all the options, it is well-suited for high-power applications only[1], [16], [24].

Tab. 2-1 Primary and Secondary Capacity Calculation for Different Topologies

| Type of Topology | $C_p$ equation | $C_S$ equation |
|:---:|:---:|:---:|
| SS | $C_p = \dfrac{1}{\omega_0^2 L_p}$ | $C_S = \dfrac{1}{\omega_0^2 L_s}$ |
| SP | $C_p = \dfrac{1}{\omega_0^2 L_p}\dfrac{1}{1-k^2}$ | $C_S = \dfrac{1}{\omega_0^2 L_s}$ |
| PS | $C_p = \dfrac{1}{\omega_0^2 L_p}\dfrac{1}{Q_S^2 k^4 + 1}$ | $C_S = \dfrac{1}{\omega_0^2 L_s}$ |
| PP | $C_p = \dfrac{1}{\omega_0^2 L_p}\dfrac{1-k^2}{Q_S^2 k^4 + (1-k^2)^2}$ | $C_S = \dfrac{1}{\omega_0^2 L_s}$ |

If the primary side has a topology where the capacitor is connected in series, the resonant circuit can be powered directly from an inverter representing a voltage source. However, if the primary side is compensated with a capacitor connected in parallel with the coil, an inductor must be inserted between the inverter and the resonant circuit since the parallel resonant circuit needs to be powered from a current source. This favors SS and SP topology useince they do not require powering from a current source [24].

If the secondary side is compensated with a capacitor connected in series with the coil, the secondary circuits form a voltage source, and similarly, when the capacitor on the secondary side is connected in parallel, the output acts like s a current source [1], [25].

In addition to these four basic topologies, there are other topologies proposed in the literature, such as LCL compensation and LCC compensation. The choice of compensation topology depends on various factors, such as the type of application, load variability, input power requirements, and transfer efficiency [14].

The SS compensation topology was chosen for the design as it is best suited for this application where the load is going to differ (from the state where the battery is deeply discharged to the state where it is almost charged), for its best overall efficiency and because of that the primary compensation capacity is not affected by a coupling coefficient or quality factor of the secondary coil.

## 2.4 Equivalent Circuit Model

In the Fig. 6 is illustrated the equivalent circuit model of the proposed IPT system from Fig. 2. It is a model of a two-coil IPT system coupled with mutual inductance $M$. The input DC voltage $V_{iDC}$ is converted to a square wave by a full-bridge inverter formed by MOSFET transistors $T_{1-4}$. The series-series compensation is used within the transmitter (primary) and the receiver (secondary) resonant circuits formed by capacities Cp, Lp, and Cs, Ls, respectively. The AC voltage at the output of the secondary resonant circuit is rectified by a full-bridge rectifier formed by Schottky diodes $D_{1-4}$. The BMS is neglected, and the output of the rectifier is directly connected to the battery.
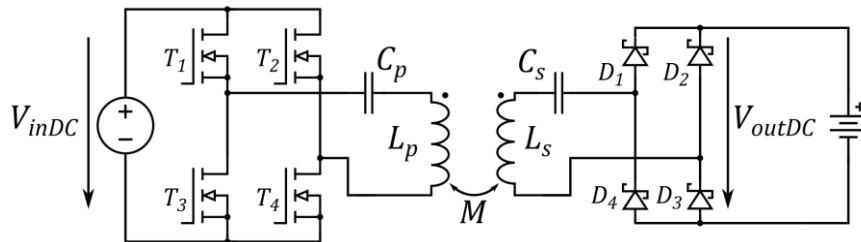


Fig. 6 The equivalent circuit model of the proposed IPT system. Source [3], edited.

To determine voltages and current within the circuit, it is appropriate to simplify the model to an AC model and use vectors. Modelling the IPT system can vary with a different approach to coupling effect between the secondary and the primary networks. In the following sections, a mutual inductance model and the reflected impedance model are used as they provide a good overview of the coupling effect between the primary and the secondary.

## 2.4.1    Mutual Inductance Model

The mutual inductance model in Fig. 7 describes the coupling effect between the primary and secondary with mutual inductance. The main advantage of this model is that the leakage inductance is not modeled separately from the mutual inductance, and the coupling effect between the primary and secondary is more visible.

Using the First Harmonic Approximation (FHA), the inverter from the Fig. 6 is simplified to an ideal AC voltage source $\hat{V}_{in}$ with amplitude $V_{in}$, frequency $f$ (equal to the switching frequency), and a phase $\varphi_{in}$ with respect to the input current $\hat{I}_{in}$. Note that by using the FHA, we can express the voltages and currents within the circuit in Fig. 7 as phasors. The next assumption is that the operating frequency within the IPT system remains constant.
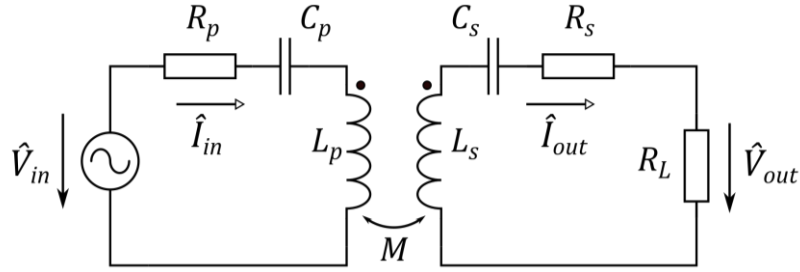


Fig. 7 Mutual inductance model.

The current $\hat{I}_{in}$ flows through the series resonant circuit where $R_p$ is the total resistance of the primary side, including equivalent series resistance (ESR) of the coil and the capacitor and all additional resistance, such as resistance of wires and connectors.

The primary and secondary compensation capacity of the capacitors $C_p$ and $C_s$ are calculated according to Tab. 2-1 as follows:

$$C_p = \frac{1}{\omega_0^2 L_p}, \tag{2-4}$$

$$C_S = \frac{1}{\omega_0^2 L_s} \tag{2-5}$$

where $\omega_0 = 2\pi f_0$ and $f_0$ is the resonant frequency to which both the primary and the secondary resonant circuits are tuned.

The voltages on the primary and secondary capacitors are calculated as:

$$V_{Cp} = j\frac{\hat{I}_{in}}{\omega C_p}, \tag{2-6}$$

$$V_{Cs} = j\frac{\hat{I}_{out}}{\omega C_s} \tag{2-7}$$

where $\hat{I}_{out}$ is the current in the secondary. The primary and secondary coil inductances are depicted with $L_p$ and $L_s$ and the dot at the top of the inductor symbol indicates that the current flowing into the coil end marked with the dot will generate a magnetic field with the same orientation.

The coupling effect is respected with mutual inductance M which can be expressed by rewriting the equation (2-2) as:

$$M = k\sqrt{L_p L_s}. \tag{2-8}$$

The voltage on the primary and the secondary inductors are then:

$$V_{Lp} = j\omega L_p \hat{I}_{in} - j\omega M \hat{I}_{out}, \tag{2-9}$$

$$V_{Ls} = j\omega L_s \hat{I}_{out} + j\omega M \hat{I}_{in}. \tag{2-10}$$

The second term in (2-9) $-j\omega M \hat{I}_{out}$ is the induced voltage in primary, and it is labeled as $\hat{V}_{ip}$. Similarly, the second term in (2-10) $j\omega M \hat{I}_{in}$ is the induced voltage in secondary and is labeled as $\hat{V}_{is}$. The $R_L$ in the scheme is equivalent load resistance which simplifies the rectifier and the battery into a single equivalent resistance. We can now describe the circuits with the following two voltage equations:

$$\hat{V}_{in} = R_p \hat{I}_{in} + j\left(\omega L_p - \frac{1}{\omega C_p}\right)\hat{I}_{in} - j\omega M \hat{I}_{out}, \tag{2-11}$$

$$j\omega M \hat{I}_{in} = (R_s + R_L)\hat{I}_{out} + j\left(\omega L_s - \frac{1}{\omega C_s}\right)\hat{I}_{out}. \tag{2-12}$$

## 2.4.2 Reflected Impedance Model

By modifying the mutual inductance model, we get a reflected impedance model (Fig. 8 (a)), which shrinks the two separate circuits coupled with mutual inductance into one circuit where the effect of the secondary is represented by the single equivalent reflected impedance.

To determine the reflected impedance, we need to first express the impedance of the secondary, often referred to as a lumped impedance. We can sum all the impedances on the secondary connected in series to one single secondary side impedance $\hat{Z}_s$ as follows:

$$\hat{Z}_s = R_s + R_L + j\left(\omega L_s - \frac{1}{\omega C_s}\right). \tag{2-13}$$

Similarly, we can sum all the components' impedances on the primary to one primary impedance $\hat{Z}_p$ as:

$$\hat{Z}_p = R_p + j\left(\omega L_p - \frac{1}{\omega C_p}\right). \tag{2-14}$$

According to [27], the reflected impedance $\hat{Z}_r$ in the primary side is given by:

$$\hat{Z}_r = \frac{\omega^2 M^2}{\hat{Z}_s} = \frac{\omega^2 M^2}{R_s + R_L + j\left(\omega L_s - \frac{1}{\omega C_s}\right)}. \tag{2-15}$$

The reflected impedance is another way to express the coupling between the secondary and the primary. The reflected impedance is a complex variable in which real and imaginary parts can be described as:

$$\text{Re } Z_r = \frac{\omega^4 C_S^2 M^2 (R_S + R_L)}{(\omega^2 C_S L_S - 1)^2 + \omega^2 C_S^2 (R_L + R_L)^2}, \tag{2-16}$$

$$\text{Im } Z_r = \frac{-\omega^3 C_S M^2 (\omega^2 C_S L_S - 1)}{(\omega^2 C_S L_S - 1)^2 + \omega^2 C_S^2 (R_S + R_L)^2} \tag{2-17}$$

The series combination of $\hat{Z}_p$ and $\hat{Z}_r$ is the impedance seen by the source and is labeled as input impedance:

$$\hat{Z} = \hat{Z}_p + \hat{Z}_r = R_p + j\left(\omega L_p - \frac{1}{\omega C_p}\right) + \frac{\omega^2 M^2}{R_s + R_L + j\left(\omega L_s - \frac{1}{\omega C_s}\right)} \tag{2-18}$$

11
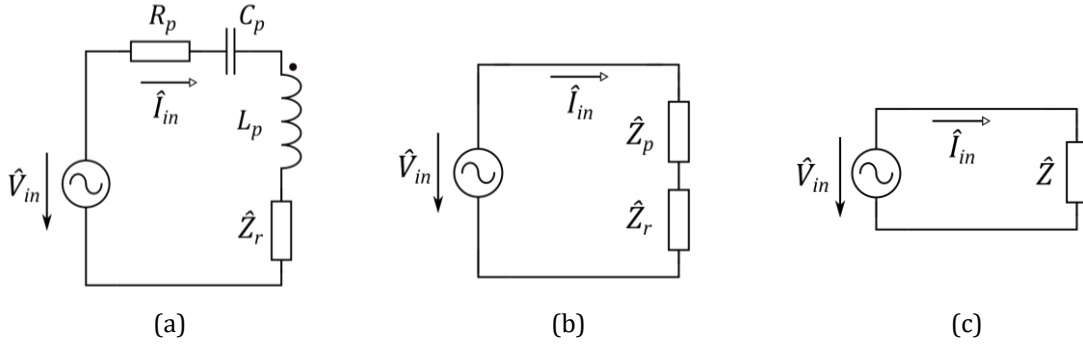
Fig. 8 Simplification of the mutual inductance model to (a) reflected impedance model, (b) model with primary and reflected impedance and (c) model with only input impedance.

Using the input impedance $\hat{Z}$ we can calculate the input current $\hat{I}_{in}$ as:

$$\hat{I}_{in} = \frac{\hat{V}_{in}}{\hat{Z}} = \frac{\hat{V}_{in}}{R_p + j\left(\omega L_p - \frac{1}{\omega C_p}\right) + \frac{\omega^2 M^2}{R_S + R_L + j\left(\omega L_S - \frac{1}{\omega C_S}\right)}} = \frac{\hat{V}_{in}\left(R_S + R_L + j\left(\omega L_S - \frac{1}{\omega C_S}\right)\right)}{\left(R_p + j\left(\omega L_p - \frac{1}{\omega C_p}\right)\right)\left(R_S + R_L + j\left(\omega L_S - \frac{1}{\omega C_S}\right)\right) + \omega^2 M^2} \qquad (2\text{-}19)$$

And similarly, the output current in the secondary and the output voltage can be expressed using the secondary impedance $\hat{Z}_s$ as:

$$\hat{I}_{out} = \frac{\hat{V}_{is}}{\hat{Z}_s} = \frac{j\omega M}{\hat{Z}\hat{Z}_S} V_{in}, \qquad (2\text{-}20)$$

$$\hat{V}_{out} = R_L \hat{I}_{out} = \frac{j\omega M R_L}{\hat{Z}\hat{Z}_S} V_{in}. \qquad (2\text{-}21)$$

The reflected impedance model is useful as we can describe the input and output voltages and currents by coupling with a single reflected impedance.

To express the output power $P_{out}$, as a product of $V_{out}$ and $I_{out}$, we need to consider the phase shift between $I_{out}$ and $V_{out}$, as well as the phase shift between $I_{out}$ and $I_{in}$. At the resonance frequency $f_0$ the phase shift between $I_{out}$ and $I_{in}$ is 90° in the case of positive coupling of coils, as shown in the Fig. 7. However, outside of the resonance frequency, the phase shift between $I_{out}$ and $I_{in}$ depends on the $R_L$ and the difference between $f$ and $f_0$. Assuming that the output of the Receiver is loaded by a pure resistance $R_L$, we can determine the output active AC power as:

$$P_{out} = \frac{1}{2}\left|\hat{V}_{out}\hat{I}_{out}^*\right| = \frac{1}{2}\frac{\omega^2 M^2 R_L}{\left|\hat{Z}\hat{Z}_S\right|^2} V_{in}^2. \qquad (2\text{-}22)$$

We can see that the output power of an IPT system depends on various factors that may change during power transfer. These factors include the mutual inductance $M$, equivalent load resistance $R_L$, the absolute value in the denominator, input voltage $V_{in}$, and the frequency.

The absolute value in the denominator of (2-22) refers to the absolute value of a product of input impedance and secondary impedance. It must be taken into consideration that the load, input impedance, and secondary impedance are already part of the input impedance. This makes the output power strongly dependent on the frequency since primary and secondary are formed by resonant circuits.

### 2.4.3 Bifurcation

The idea that we can summarize the effect of secondary on the primary with a single impedance $\hat{Z}_r$ is pleasing. However, as we can see in (2-16) and (2-17), its real and imaginary parts are not exactly simple. Summed with the primary impedance $\hat{Z}_p$ to a single impedance $\hat{Z}$ we get even a more complex term. The impedance-frequency characteristic of a series resonant circuit is well known. It has a typical "V" shape with a minimum where the resonant frequency is. However, the

impedance-frequency characteristics of an absolute value of input impedance $|\hat{Z}|$ may not be that simple due to the reflected impedance $\hat{Z}_r$.

The illustrated problem is visible in the following example of a typical IPT system built on the Qi Standard as described in [28]. This IPT system was designed for a common resonant frequency of 100 kHz and equivalent load resistance range from 1 to 50 Ω. In the Fig. 9 is an impedance-frequency graph of the absolute value of the input impedance $|\hat{Z}|$ of this system for different values of load $R_L$. Since the $R_L$ is part of the $\hat{Z}_r$, the $|\hat{Z}|$ curve is changing as well.
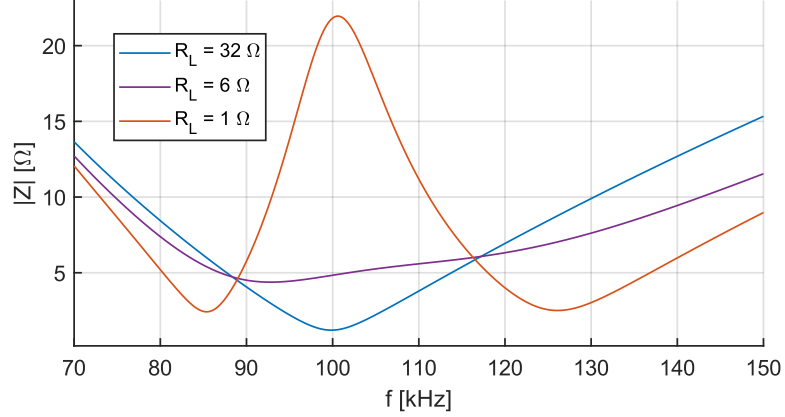


Fig. 9 Impedance-frequency curve of an exemplary IPT system. Source [28].

Going with the $R_L$ from the maximum value (corresponding to a light load) to the minimum value (corresponding to a heavy load), we observe how the shape of the $|\hat{Z}|$ curve is changing. For the lightest load, its shape is like a series resonant circuit since the effect of the reflected impedance is negligible. However, for the lowest $R_L = 1\ \Omega$ the corresponding $|\hat{Z}|$ minimum is splitting to two, and in the original resonant frequency, where was a minimum before is now a maximum of $|\hat{Z}|$.

It is important to realize that the splitting of $|\hat{Z}|$ minimum impacts the input current $\hat{I}_{in}$ and both output voltage $\hat{V}_{out}$ and current $\hat{I}_{out}$ resulting in the frequency splitting of the output power $P_{out}$ maximum as well, as shown in Fig. 10 (a).

Additionally, the phase shift $\varphi_{in}$ between the input current $\hat{I}_{in}$ and input voltage $\hat{V}_{in}$ is also affected by the secondary side influence. In this frequency range, the frequencies of zero crossings of $\varphi_{in}$ referred to as zero phase angles (ZPA), are different for different values of $R_L$, see Fig. 10 (b). The $\varphi_{in}$ is equal to zero when the imaginary part of the input impedance $\hat{Z}$ is equal to zero [27]. We can see that for low values of the load resistance, the single maximum of the output power $P_{out}$ splits from one to two, and the input phase $\varphi_{in}$ zero crossings from one to three.



(a)                                                                    (b)
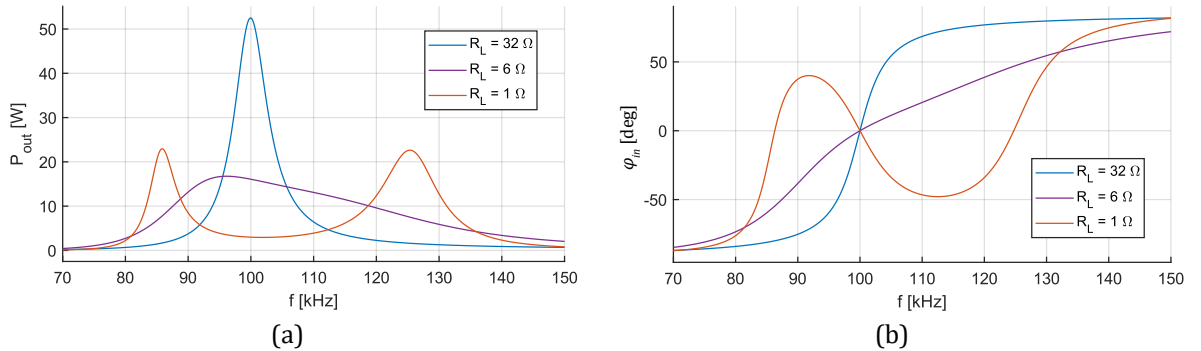
Fig. 10 (a) Output power-frequency characteristics and (b) phase shift-frequency characteristics of an exemplary IPT system. Source [26], edited.

13

This phenomenon is called frequency splitting, phase bifurcation, and splitting of input, respectively or collectively simply as a bifurcation. They are not three separate phenomena but only three manifestations of a single phenomenon, a growing secondary side influence (the reflected impedance) with heavier loads impacting the primary side.

To avoid the negative effects of the bifurcation, the operating range of a designed IPT device must be properly defined. For that purpose, a diagram like in Fig. 11 can be constructed, which defines five regions RG1-RG5 according to the possible presence of bifurcation [29].

On the x-axis is the load equivalent resistance $R_L$ and on the y-axis is the normalized frequency which is obtained by dividing the switching frequency by the resonant frequency of the IPT system. The green lines represent frequencies with zero phase angle. The pink lines $u_{ao1}$ and $u_{ao2}$ represent the frequencies where output power is maximal and $u_{ao0}$ minimal respectively.

As we proceed within the chart from left to right, we enter region RG1, where no bifurcation happens. One single ZPA frequency and one single output maximum frequency are present and are closely the same.

As we enter the region RG2, the growing secondary side influence occurs. The power output maximum moves away from the original resonant frequency to lower frequencies (as can also be seen in Fig. 10 (a), the purple curve). However, the phase bifurcation does not occur.

By entering the region, RG3 output power maximum splits to two (in Fig. 10 (a) the red curve). In the region RG4, the phase bifurcation also starts to occur – creating another two ZPA frequencies besides the original resonant frequency. The RG5 is labeled as a region of very deep bifurcation where all bifurcations appear, and their frequencies are stabilized at their asymptotes.
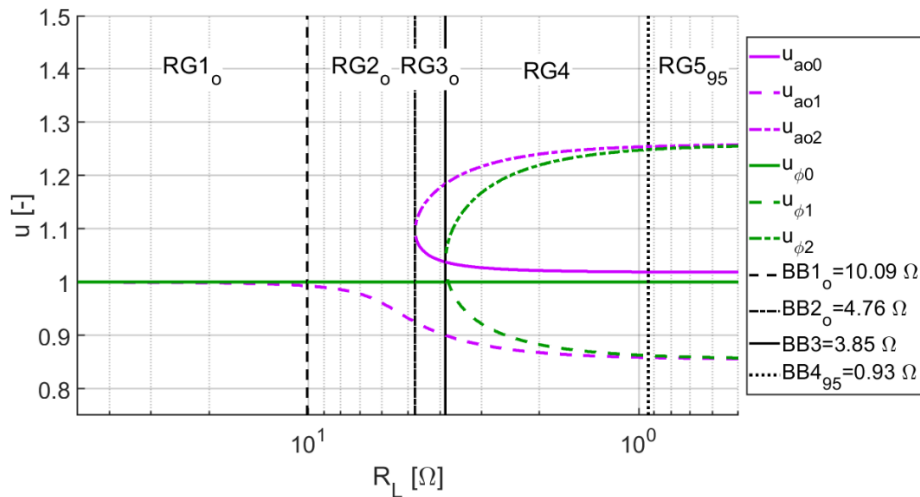


Fig. 11 Operating regions defined by bifurcation occurrence. Green lines represent the phase bifurcation and purple lines represent the output amplitude bifurcation. Source [29].

### 2.4.4 Operation of IPT System

In the implementation of a practical IPT system, both input and output parameters must be clearly defined, as well as the type of output control for the proper operation of the IPT system. These parameters state the operating range of the IPT device.

#### 2.4.4.1 Input & Output Parameters

The input parameters represent the limits of the system design. Those are specified by the application and the application environment. Typical input parameters are input voltage and current or distance of the air gap.

The output parameters, such as the range of output power, output voltage, or output current, represent the desired parameters of the IPT system. The IPT device should be designed to meet the desired parameters. The output parameters can be obtained from the load specification and

based on the device's requirements. It is essential to know these values since they define the behavior of the load during the operation.

For example, in the Fig. 12 we can see a typical Li-ion battery cell charging characteristic. We can see how the equivalent resistance equal to the load resistance raises as the battery is charged. First, the battery is charged in the constant current (CC) mode, and when the voltage on the battery reaches a certain threshold, the battery should be charged in constant voltage (CV) mode.
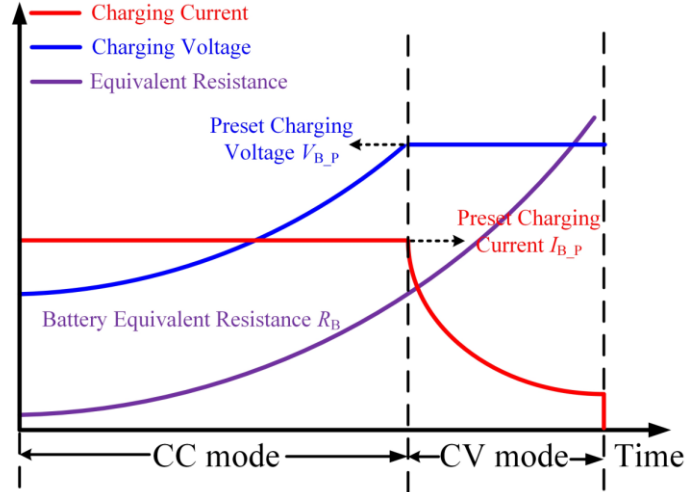


Fig. 12 Li-ion battery cell charging characteristics and its equivalent resistance. Source [30].

The designed IPT charger should respect the fact that the load resistance varies over time and should be able to provide enough power.

### 2.4.4.2  Output Control

The IPT system controls the operation process using regulation to maintain the desired output parameters. Without proper control, the device could not be operated in different operating points than the one it was designed for.

The control problem involves specifying the regulated variables, system constants, system variables, and control variables. The system variables are dynamic system quantities that can vary during the operation, such as the mutual inductance or coupling coefficient, while system constants are fixed system quantities that are constant by design. Typically regulated variables include the amplitude of the output voltage, current, output power, or efficiency. Control variables within the regulation process are circuit parameters continuously adjusted by the control system to meet performance objectives [29].

If we consider the proposed system in Fig. 6, where only the inverter on the primary side is capable of changes during the operation of the IPT system, possible control variables for such a system could be the inverter's switching frequency, duty cycle, or the phase shift between input current and input voltage. Placing a dc-dc converter on the secondary side would allow secondary control. However, in the proposed system, only primary side control is employed instead, reducing the number of components which leads to minimizing losses in the system.

Primary side control strategies in an IPT system like this can be categorized into three main types [31]:

1. Phase Shift Control: This method involves adjusting the phase shift between the primary current and voltage. By Changing the phase, we can modify the output voltage characteristics to regulate the power delivered to the load.

2. Frequency Control: Frequency control is a common strategy where the switching frequency of the inverter is adjusted to control the output power. By varying the switching frequency, the system can operate in different regions to optimize the power transfer efficiency.

3. Dual Control: Dual control combines phase shift and frequency control methods. It detects zero crossings of the primary current and triggers the gate signals of the switches accordingly. This control scheme ensures inductive operation and minimizes switching losses.

Although there are also other control strategies, these are the most employed. The further text describes the frequency control with output voltage as a regulated variable as it is most relevant for our application.

### 2.4.4.3 Regulation to Constant Output Voltage by Frequency Control

The connection between the reflected impedance and frequency plays a crucial role in regulating the output voltage in an IPT system, as described at the beginning of 2.4. If we take the Fig. 11 where bifurcation regions are displayed, and we add phase shift $\varphi_{in}$ between the input current $\hat{I}_{in}$ and input voltage $\hat{V}_{in}$ on the y-axis we will get a Fig. 13 (a). In this plot, we can see how the $\hat{Z}$ changes from inductive to capacitive around borders specified by the ZPA frequencies for different loads. And if we take the same diagram from Fig. 11 with bifurcation regions and on the y-axis, we will plot an absolute value of the output voltage we will get a Fig. 13 (b). The isolines where the output voltage is constant are marked within the diagram.
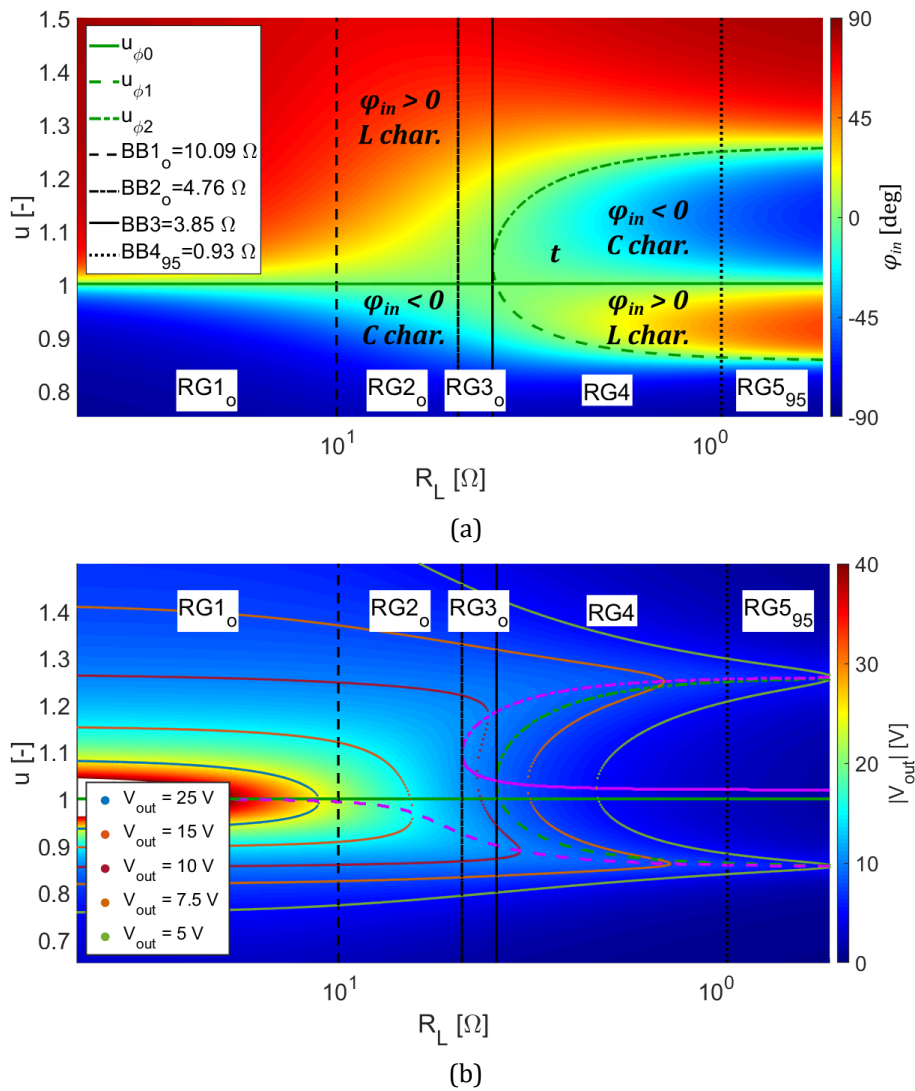


Fig. 13 (a) Phase shift and (b) output voltage in the diagram section with boundaries respecting the occurrence of bifurcation. Source [29], edited.

From Fig. 13 (b), we could say that the desired output voltage can be reached for different loads with different frequencies. For example, for the value $V_{out}$ = 25 V and $R_L$= 10 Ω we can set the frequency both to approximately 1.4 and 0.8 times the original resonant frequency, and the output voltage would be the same. However, if we take those operating points and display them in the Fig. 13 (a) we can see that for one frequency, the operating point is in the region where $\varphi_{in}$ is > 0, i.e., the input impedance is inductive and for the second frequency, the operating point is in the region where $\varphi_{in}$ is < 0, i.e., the input impedance is capacitive.

To avoid losses in MOSFETs caused by the hard-switching and achieve Zero Voltage Switching (ZVS), a necessary condition is that the input impedance $\hat{Z}$ should be inductive. Hence, from the two possible frequencies, only the first, where u = 1.4 is possible. If we take a closer look at Fig. 13 (a) and focus on how phase shift changes within the figure, we can see that the input impedance is inductive in the regions where the frequency is above common resonant frequency (u>1) until reaching the ZPA frequency in the region RG4. Similarly, the $\varphi_{in}$ < 0 is in the region RG4 and RG5 where u<1. However, those regions represent the regions with high bifurcation and should be avoided.

Thus, the operating range of the IPT system frequencies is placed above the common resonant frequency (u>1). However, if the operating frequency is too close to the border where u = 1, the input impedance might easily change from inductive to capacitive by a sudden change in load and/or coupling, which causes the inverter to lose ZVS. Additionally, the control algorithm should detect the change of the impedance character. Otherwise, it would not correctly react, and the stability of the control would be lost. By placing other components or algorithms responsible for detecting the change in the phase shift $\varphi_{in}$, we would achieve a dual control as mentioned in 2.4.4.2. However, this is not the case with frequency control.

From the bifurcation point of view, in the case of frequency control, the operating frequency is selected higher than all three ZPA frequencies (green lines within the Fig. 11), i.e., the regions RG1-RG3 to guarantee the soft-switching operation and stability of the control process. From the designer's point of view, if we consider the exemplary system from the Fig. 13, this means that the only possible output voltage levels are the isolines where $V_{out}$ = 15 or 25 V where the second one is more convenient in terms of control. If the output voltage cannot be reached within these regions, the IPT system parameters must be adjusted, or the overall output parameters must be reconsidered. Otherwise, the system would be designed incorrectly.

Overall, the IPT system operating range should be set to ensure the stability of the control process and allow soft-switching to maximize the overall DC-DC efficiency. However, the switching losses are not the only losses within the IPT system. The significant losses within the proposed IPT system (Fig. 6) are thoroughly discussed in the upcoming section.

### 2.4.5    Power Losses and DC-DC Efficiency

To determine the losses within the proposed IPT system, as illustrated in Fig. 6, we must determine the losses of each component within the circuit. The same circuit is thoroughly discussed in the study of the optimization method for systems with variable frequency [32].

The losses caused by the ESRs of the components within the resonant circuits, as depicted in Fig. 7 can be calculated as:

$$\Delta P_{ESR} = \frac{1}{2} R_p \left| \hat{I}_{in} \right|^2 + \frac{1}{2} R_S \left| \hat{I}_{out} \right|^2. \tag{2-23}$$

Next, we must consider every significant loss within the full-bridge inverter and the full-bridge rectifier, as depicted in Fig. 6. We can calculate the losses of the full-bridge inverter as a sum of losses on each MOSFET:

$$\Delta P_{inv} = 4(\Delta P_{sw} + \Delta P_{cond}) \tag{2-24}$$

where $\Delta P_{sw}$ are the switching losses, $\Delta P_{cond}$ are the conduction losses of a single MOSFET.

The switching losses $\Delta P_{sw}$ depend on whether the inverter is operating in "hard switching" mode or "soft switching" mode. If soft switching occurs, switching losses $\Delta P_{sw}$ can be calculated as follows:

$$\Delta P_{sw} = \frac{1}{2} C_{oss} V_{inDC}^2 f \tag{2-25}$$

where $V_{inDC}$ is the input voltage on the DC-link and $C_{oss}$ is the output capacitance of the single MOSSFET which can be found in the datasheet. If the soft switching turns into hard switching, then switching losses $\Delta P_{sw}$ can be calculated as:

$$\Delta P_{sw} = \frac{1}{2} V_{iDC} I_{inDC} (t_r + t_f) f + \Delta P_{rr} \tag{2-26}$$

where $I_{inDC}$ is the DC input current within the DC-link, $t_r$ and $t_f$ are the rise time and fall time respectively, $\Delta P_{rr}$ are the losses of the freewheeling diode reverse recovery. $\Delta P_{rr}$ can be calculated from the reverse recovery charge of the freewheeling diode $Q_{rr}$ specified in the datasheet as:

$$\Delta P_{rr} = \frac{Q_{rr}}{I_F} I_{inDC} V_{inDC} f. \tag{2-27}$$

The conduction losses are calculated as:

$$\Delta P_{cond} = \Delta P_{Rds(on)} + \Delta P_{ds(off)} \tag{2-28}$$

Where $\Delta P_{Rds(on)}$ are the forward losses of MOSFET when turned on:

$$\Delta P_{Rds(on)} = \frac{1}{2} I_{in}^2 R_{ds(on)} t_{on} f \tag{2-29}$$

where $I_{in}$ is the primary side current amplitude, $R_{ds(on)}$ is the equivalent resistance of MOSFET channel and $t_{on}$ is the time when MOSFET is turned on. $\Delta P_{Rds(off)}$ are the losses of the body diode during the deadtime and can be calculated as:

$$\Delta P_{ds(off)} = V_F I_{off} t_{dt} f \tag{2-30}$$

where $V_F$ is the freewheeling diode forward voltage drop and $t_{dt}$ is the deadtime. In case of soft switching, the $\Delta P_{ds(off)}$ can be neglected as there is no current $I_{off}$ flowing during the $t_{dt}$.

The losses of the full-wave rectifier are given by the voltage drop at the Schottky diodes and can be calculated as:

$$\Delta P_{rct} = 2 V_{fwd} I_{outDC} \tag{2-31}$$

where $V_{fwd}$ is the diode's forward voltage drop specified in the datasheet. Finally, the total losses of an IPT system are calculated as:

$$\Delta P_{tot} = \Delta P_{ESR} + \Delta P_{inv} + \Delta P_{rct} \tag{2-32}$$

and the DC-DC efficiency of the IPT system as:

$$\eta_{DC-DC} = \frac{P_{outDC}}{P_{outDC} + \Delta P_{tot}} = \frac{P_{outDC}}{P_{inDC}} \tag{2-33}$$

where $P_{inDC}$ is the input power before the Inverter and $P_{outDC}$, measured at the load.

## 2.5 The Optimization Method

The novel optimization method used in this project aims to maximize the efficiency of a variable frequency IPT system while meeting design constraints such as current and voltage ratings and maximal flux density. The optimization variables are the number of layers and the number of turns per layer, and the input DC voltage. The method is thoroughly described in a separate article, and its full form can be seen in [3].

### 2.5.1 The Procedure of the Method

The brief procedure of the optimization method can be described in the following steps (step numbers in the following list correspond to the step numbers in Fig. 14):

1. Define the IPT system, including load, resonance frequencies, components, and coupling coil materials and geometry to determine the geometry model, equivalent circuit parameters, and design constraints.

2. Optimize the geometry parameters, including the number of layers and turns per layer.
3. Calculate inductances using Finite Element Method Magnetics (FEMM) and coil ESRs based on the length and material of winding wire and the losses in the coil ferrite.
4. Calculate the remaining equivalent circuit parameters, with input DC voltage taken out of the parameters controlled by the optimization algorithm.
5. Obtain the power-frequency characteristic using a numerical bracketing method to find frequencies where the output DC power range gains the target value for each point in the range.
6. Evaluate the power-frequency characteristic, component current and voltage ratings, and maximal magnetic flux densities in primary and secondary ferrites and remove unsuitable design variants.
7. Evaluate the design variants given by input DC voltage values, discard those not meeting design constraints, and select the variant with maximal average efficiency.
8. Test the different combinations of coil geometry parameters with the result input voltage from the Step 7 to find the combination with the maximal average $\eta_{DC-DC}$.
9. The optimization algorithm is successful in the computed average $\eta_{DC-DC}$ is greater than the set threshold resulting in an IPT system with optimized geometry and $V_{inDC}$. If the threshold isn't met, replace the problematic components and/or revise design constraints by returning to Step 1.
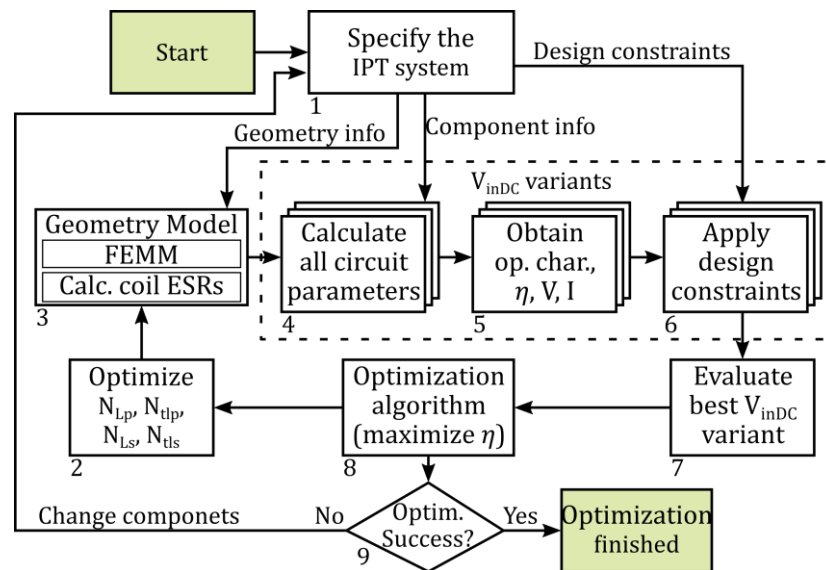


Fig. 14 The optimization method flowchart. Source [3], edited.

## 2.5.2    Requirements for the MCU

The optimization method also considers the influence of discretization of power-frequency characteristics caused by digital signal processing. The power-frequency characteristic $f = f(P_{out})$ is a characteristic used in the control process which relates the operating frequency to the output power, where the output voltage $V_{outDC}$ is equal to the target value.

The MCU usually controls the frequency using a timer, where the period of the switching signals can be adjusted in minimal steps given by the resolution of the timer. If we take the ideal power-frequency characteristic within the operating range of the IPT system (Fig. 15. (a)) and transform it into a power-period characteristic, we will get a chart like in Fig. 15 (b). If we consider each possible period that the timer of the MCU can generate, we will get separate operating points as marked in the figure resulting in a discrete period power-period characteristic.

19
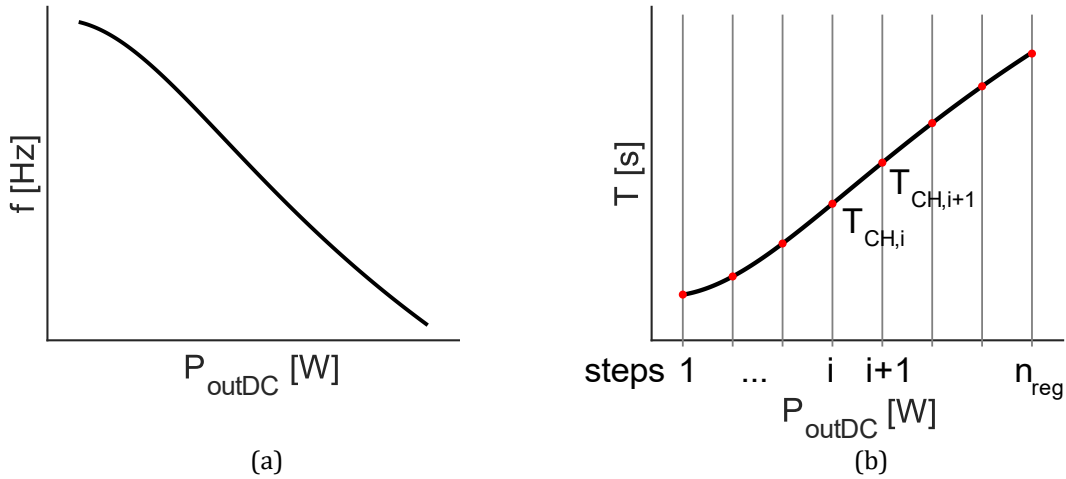
Fig. 15 (a) Typical power-frequency characteristic and (b) Power-period characteristic with timer steps of an IPT system. Source [3].

Hence, selecting an MCU whose timer's resolution is high enough to ensure smooth regulation in the whole power-frequency characteristic is essential.

## 2.6     Qi Standard

The Qi wireless charging standard, developed by the Wireless Power Consortium (WPC), is an IPT standard based on IPT technology that enables wireless power transfer over short distances. The standard ensures the compatibility of transmitters and receivers from various manufacturers and includes complete documentation of the Standard, including tests and methods for validation.

The initial version of the Qi Standard, released in July 2010, featured a transmitter of 5 watts of power, which was capable of charging Qi-compatible devices. Since then, the standard has undergone several revisions, with the current version being 1.3, introduced in January 2021 [33].

The standard operates at a frequency of 110-205 kHz and power levels of up to 15 watts, depending on the device's design and the charging pad's capabilities. With such electrical parameters, the standard focuses mainly on consumer electronics, including smartphones, tablets, smartwatches, and other portable electronics [34].

To ensure compatibility with other devices using the standard, a producer must register the device and list it in the Qi-certified products. The device must also undergo a series of tests by an authorized test lab to ensure compliance with the Qi Standard. These tests include testing for interoperability, electromagnetic compatibility, and safety. Once certified, a device can bear the Qi logo, indicating its compatibility with other Qi-certified devices.

### 2.6.1     Qi Standard Terminology

In the standard Qi documentation, specific terminology is used across the whole documentation. Additionally, we can find a list of all definitions used across the entire Standard documentation in the glossary [35]. Below is a short version of a list and their short description:

- Analog Ping: A short-duration Power Signal applied by a Transmitter to detect the presence of an object without waking up a Receiver.
- Digital Ping: A Power Signal applied by a Power Transmitter to wake up a Power Receiver.
- Guaranteed Load Power: A Load Power level agreed between the Power Receiver and the Power Transmitter.
- Load Power: The power dissipated to the Load.
- Operating Point: The combination of the frequency and the input voltage
- Power Signal: An alternating magnetic field generated by Power Transmitter.
- Primary Coil/Cell: The Transmitter Coil.

20

- Secondary Coil/Cell: The Receiver Coil.

The standard Qi terminology will be used in the following sections for better compliance with the Standard documentation.

## 2.6.2    Internal Communication between the Transmitter and the Receiver

The Qi standard defines the internal communication between the Transmitter and the Receiver. Internal communication is used to configure and control the power transmitted across an air gap. Additionally, the standard allows using the so-called Extended Power Profile (EPP) to transfer application-level data using the internal communication from the transmitter to the receiver and the other way[36].

The standard distinguishes the direction of the data flow. Two different types of modulation techniques are used. To transfer data from the Transmitter to the Receiver, the Transmitter uses a Frequency Shift-Keying (FSK) modulation technique to modulate the data into the Power Signal. For the opposite direction of the data transfer, from Receiver to Transmitter, the Receiver uses an Amplitude Shift-Keying (ASK) modulation.

## 2.6.3    ASK Modulation

Amplitude Shift-Keying modulation or load modulation is a backscatter modulation technique used in Qi standard for communication purposes in Receiver to Transmitter direction. The Receiver modulates the amount of power drawn from the Power Signal (the carrier wave) between the power supply on the transmitter side and the load on the receiver side. The Power Transmitter detects the variations in the amplitude of the Power Signal by sensing the current through and/or voltage across the Primary Cell with or without an additional demodulation circuit.

The Receiver uses a differential bi-phase encoding scheme to modulate data bits onto the Power Signal. The Receiver encodes ONE bit using two transitions in the Power Signal and a ZERO bit using a single transition in the Power Signal. The transition is a change from the state where the additional load is connected to the state where it is disconnected and otherwise. In [37] we can see an example of a bit encoding scheme.
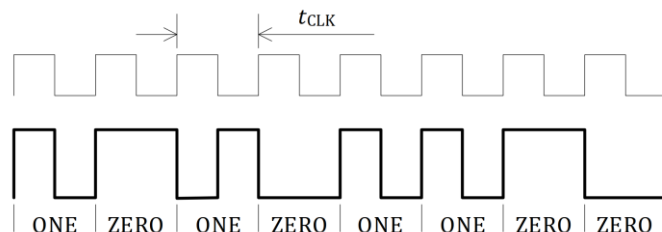


Fig. 16 ASK Bit encoding scheme. Source [37].

The modulation scheme used is such that the Primary Cell current and/or Primary Cell voltage assume two states: a HI state and an LO state. The difference in the amplitude of the Primary Cell current in the HI and LO state should be at least 15 mA, or the difference in the amplitude of the Primary Cell voltage in the HI and LO state should be at least 200 mV.

The frequency of the modulated signal is (2 ± 4%) kHz or (2000 ± 4%) Bd. The actual speed of communication is lower due to the additional parts within the data packet structure in which the actual data are wrapped in.

The physical implementation of the ASK modulation may vary. We can find many examples in the Power Receiver Reference Designs of ASK implementation [38]. In the Power Receiver, Example 3 within the [38] an additional load to the ground in form of capacitors is connected on the AC side on both lines entering the full bridge rectifier. In example 4, there are resistors instead of capacitors. Example 2 uses a single resistor connected between the two output lines on the rectified side.
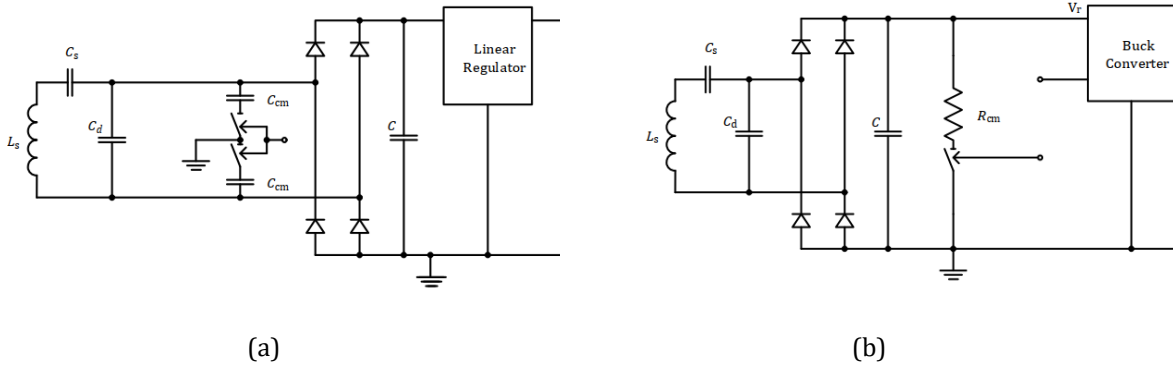
Fig. 17 Examples of different implementations of ASK Modulation (a) Modulation on the AC side (b) Modulation on the DC side. Source [38].

### 2.6.4 FSK Modulation

Frequency Shift-Keying Modulation is a modulation technique that is based on encoding the information into the frequency shifts within the carrier signal. The Transmitter uses this modulation technique to communicate with the Receiver.

The Transmitter switches its frequency between the Operating Frequency $f_{op}$ in the unmodulated state and the Operating Frequency $f_{mod}$ in the modulated state based on the modulated data. However, the Operating Frequency changes during the power transfer as well due to the output regulation as described in 2.4.4.3 and the Receiver should be able to distinguish between the change in frequency due to the output control and the modulated data. For that, Qi standard defines a restricted timeframe in which the frequency of the Power Signal can be changed only by the FSK modulation, and output regulation cannot interfere [37].

Similarly, as in the case of ASK Modulation, the Transmitter uses a differential bi-phase encoding scheme to modulate data bits in the Power Signal. On the other side, the frequency of the modulated signal differs and varies with the frequency of the Power Signal. The transmitter aligns each data bit to 512 periods of the Power Signal, as depicted in Fig. 35.

The ONE bit is encoded using two transitions in the Power Signal frequency (meaning changes between the Operating Frequency in modulated and unmodulated state). The first transition should be done in the middle of the modulated period corresponding with the 256th period of the Power Signal. The ZERO bit is encoded using a single transition in the Power Signal frequency at the start of the bit.
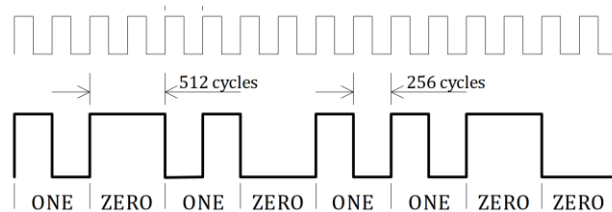


Fig. 18 Example of bit encoding in FSK Modulation. Source [37].

The realization of the FSK modulation is usually implemented directly in the Transmitter's MCU, as it can be controlled by changing the period of the switching signals.

# 3    DESIGN CONCEPT

This section outlines the following concepts characterizing the wireless charger operation. The system architecture specifies the device's basic structure and its interactions with surrounding systems. The charging sequence overview outlines the charger operation by a state diagram. The software architecture represents the charger functionality by interactions between the signals, HW peripherals of the control unit, and SW functions in a hierarchical fashion. Finally, the 3D model of the transmitter and receiver presents a proposed mechanical design for the wireless charger.

## 3.1    System Architecture

Fig. 19 depicts the system architecture of the designed Wireless Charger, which implements the IPT system as depicted in Fig. 2 and Fig. 6 into a real device with additional functional blocks needed for the proper operation of the wireless charger.

The Wireless Charger consists of two main modules: the Transmitter and the Receiver. The surrounding modules, i.e., Head Unit, Ground Station, External Voltage Source, and Other Rocket Units, are captured to illustrate the charger's operation. The system can be divided into general blocks based on their function, which may represent separate hardware blocks but does not necessarily have to. The illustration also captures power supply lines and power and data flow.
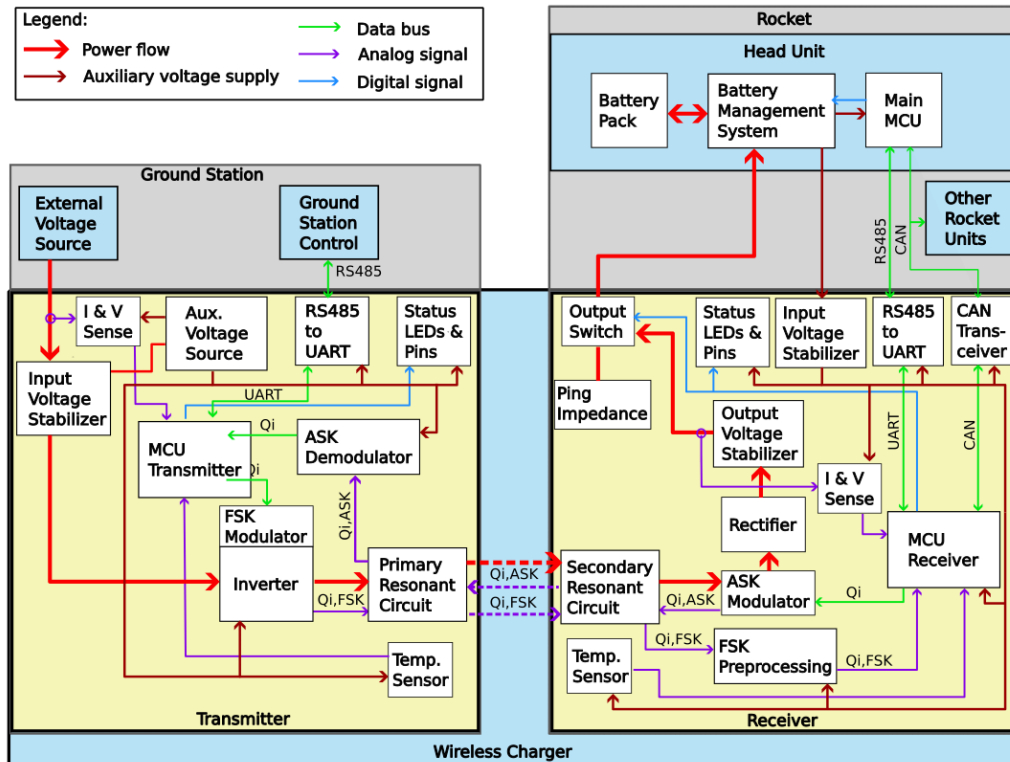


Fig. 19. Diagram of the system architecture. Gray blocks indicate parts of the Ground Station and the rocket. Blue blocks are separate devices with individual functional blocks marked by a white background.

The primary function of the Wireless Charger is to provide the regulated DC voltage at the Receiver output. This regulation is achieved through adjustments in the operating frequency described in 2.4.4.3, which is the switching frequency of the Inverter located in the Transmitter. Communication between the Transmitter and the Receiver is achieved with FSK Modulation by the Transmitter and ASK Modulation by the Receiver. Because the charger is designed for a specific application and compatibility with third-party devices is unnecessary, some parts of the Standard were omitted or adjusted to ease the final implementation. The Primary and Secondary

23

Resonant circuits are tuned to the same frequency of 100 kHz. The fixed position of the coils achieved by permanent magnets (see 3.4) provides constant coupling.

### 3.1.1 Transfer of Power

The Power Transmitter is powered from the External Voltage Source of 48 V DC. The input voltage ripple and potential fast transients are stabilized using the Input Voltage Stabilizer. Since the control and measurement components need +3,3 V and +12 V DC voltage, the Auxiliary Voltage Source is included. The full-bridge Inverter converts the input 48 V DC voltage to rectangular voltage with a constant duty cycle set to 0.5. The switching frequency is regulated from 160 to 210 kHz to keep constant DC voltage at the Power Receiver's output. The Inverter is connected to the Primary Resonant Circuit formed by a capacitor and coil generating the magnetic field, which transfers the power across the air gap to the Receiver. The AC voltage is induced in the receiving coil of the Secondary Resonant Circuit. It is then rectified by a full-wave Rectifier and stabilized using an Output Voltage Stabilizer to minimize voltage ripple. The Receiver has an Output Switch alternating between the Ping Impedance and direct output connection to the rocket's Battery Management System. The Ping Impedance is used in Analog and Digital Ping [39], [40] and enables the communication between the Transmitter and Receiver when the power transfer is shut off. In contrast to the Qi Standard, the Receiver is powered directly from the rocket's battery through an Input Voltage Stabilizer and remains constantly on.

### 3.1.2 Control and Measurement

Device control is split between two separate MCUs to control both the Transmitter and Receiver. STM32F334C8T6 from ST Microelectronics was selected for this task. These MCUs operate within the operational states specified in 3.2.

The input current and voltage are measured on the DC link before the Inverter and the Input Voltage Stabilizer, using the Voltage and Current Sense. The output current and voltage are measured on the Receiver side after the Output Voltage Stabilizer using the same Voltage and Current Sense. With these positions of measuring circuits, it is possible to measure the total input and output power correctly. By measuring current and voltage on the DC side, instead of the AC side, the demands on measurement evaluation are reduced. In addition, temperature sensors have been placed under the Transmitter and the Receiver coil pads. The measured data are essential for output regulation and fault state detection, such as overload or overvoltage.

The output voltage is regulated using the frequency control as described in 2.4.4.3. The Transmitter's MCU adjusts the switching frequency based on the current actual value of the DC current at the inverter input and the control error from the Receiver regularly sent in the corresponding data packets.

### 3.1.3 Communication

The Wireless Charger serves as a link in the main communication line between the Ground Station and the Head Unit of the rocket which uses the Modbus protocol. The Ground Station acts as the master device, while the Head Unit functions as the slave device. To pass the air gap, Modbus messages are "packed" in Qi message format [39] using the data transport stream feature [40] by Transmitter MCU and then "unpacked" by Receiver MCU. Communication speeds provided by Qi are sufficient for this application.

The physical layer of communication can be divided into two separate channels. The first channel includes communication between the Ground Station and the Head Unit. The Transmitter uses a full-duplex serial communication RS485 which is converted to a Universal asynchronous receiver-transmitter (UART) and processed by the Transmitter's MCU. The message is modulated to Power Signal in the Inverter using FSK modulation and transmitted across the air gap by magnetic field. The Receiver demodulates the signal at FSK Preprocessing and MCU and subsequently converts the received data back to UART and then back to RS485 via a converter.

Communication in the opposite direction – from Receiver to Transmitter is similar but back scattering based ASK is used to transfer the data across the air gap [39].

An additional communication channel based on Controller Area Network (CAN) is implemented in the Receiver, to allow fast communication between the Wireless Charger and the Head Unit in case of a battery error or additional faults. In such a case, the Output Switch rapidly disconnects the Receiver power output, and Ping Impedance is connected to maintain communication with the Transmitter and the Ground Station. Additionally, the Receiver can transmit information such as incoming power levels and current temperatures to the Head Unit.

A set of status LEDs visually indicates the charger's current state.

## 3.2 Charging Sequence Overview

The state diagram in Fig. 20 summarizes the charger's operation from power-on to shut-off, including the resolution of fault states. It is an adapted state diagram for the Qi Extended Power Profile (EPP) [40]. Certain states have been omitted or modified to fit the application's specific requirements. The data packet tags mentioned in the diagram correspond to their equivalents in Qi Standard described in [40]. The state diagram captures the operation of both the Transmitter and the Receiver. The charger operates in seven main states.
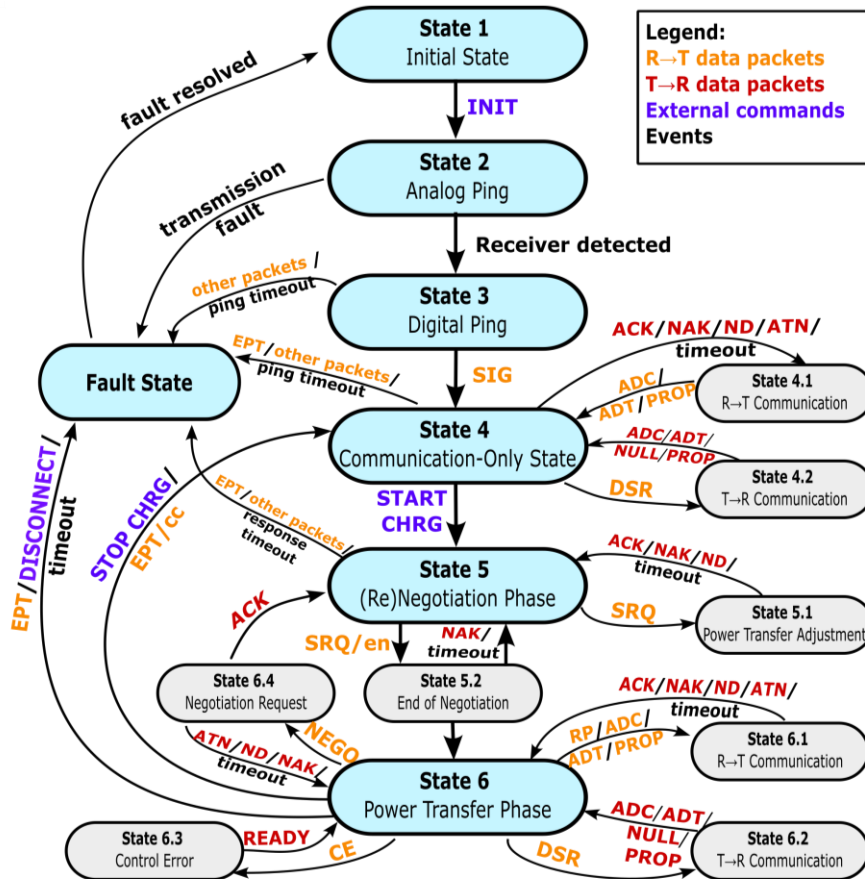


Fig. 20. The state diagram of the charging sequence.

### 3.2.1 Initial State

In the Initial state (State 1 in Fig. 20), the Transmitter is connected to the External Voltage Source and the Ground Station through RS485. The Receiver and Transmitter coils are properly aligned, and the Output Switch is connected to the Ping Impedance. No power transfer or communication occurs through the air gap, and the charger waits for a command from the Ground Station via RS485 to initiate the connection between the Transmitter and Receiver.

### 3.2.2　Analog Ping

In State 2, the Transmitter evaluates the presence of the Receiver. The Transmitter applies a series of short pulses of a duration defined in [41] to the Primary Resonant Circuit. The Transmitter measures the current during the pulse duration and compares it to the value corresponding when no other object is present in the surrounding of the Transmitter coil. If the value of the current is greater than the threshold value, the Transmitter evaluates that the Receiver may be present, and the operation state is changed to the Digital Ping.

### 3.2.3　Digital Ping

In State 3, the Transmitter starts to transmit a Digital Ping. That means the transmitter applies a longer pulse to the Primary Resonant Circuit and waits for the Receiver to response. The signal's frequency is set to the value corresponding to the operating point of the Ping Impedance where the output voltage is 30 V. If The receiver does not respond at a given time defined by the standard [36], the Transmitter stops transmitting the signal and enters the Fault State. If the Receiver responds with a SIG data packet in which information about signal strength is carried, the device moves to the next state 4.

### 3.2.4　Communication-only State

In the Communication-Only state (State 4), the Transmitter and the Receiver establish two-way communication without charging the battery. The output is still disconnected. Instead, the ping impedance is connected as a load. The frequency of the Power signal remains the same as in the case of State 3. However, Transmitter and Receiver can create a communication canal to transfer application-level data. The surrounding of the wireless charger is informed that it is now possible to transfer the data. To move to the next state, both Head Unit and the Ground Station must allow to do so. The Head Unit sends status messages in regular time intervals containing information about the battery's current state of charge and any potential faults that would forbid starting the charging process. The end authorization to move to the next state to begin the charging process must come from the Ground Station. However, if the battery is in the state where charger maintains the full charge condition and the Ground Station authorized the charging before, it is not needed to ask for permission again.

### 3.2.5　(Re)Negotiation Phase

In the (Re)Negotiation Phase (State 5), the Receiver negotiates the guaranteed power level for charging. The guaranteed power level should be set to the maximum possible since it states the maximum possible power level. However, if the temperature of the coils is close to their operating maximum safe values or the Head Unit requests a lower power, the guaranteed power level should be lowered accordingly. After the new power level has been agreed upon, the Receiver shall enter the next state by sending the SRQ/en data packet. The output of the Receiver is connected to the BMS within the rocket, and the Ping Impedance is disconnected in this sequence.

### 3.2.6　Power Transfer Phase

In the Power Transfer Phase (State 6), the transferred power charges the battery pack while regulated by a PID regulator [41]. Communication and power transfer (but not the regulation action) can coincide. The power transfer is terminated if the battery is fully charged or upon external request from the Ground Station or the Head Unit. This leads to connecting the ping impedance, disconnecting the output, and returning to the Communication-Only State (State 4).

### 3.2.7　Fault State

If a fault occurs in any of the states listed above, the device will enter the Fault state, where the fault must be resolved before communication can be restored. After the fault is resolved, the device returns to the Initial state, and the sequence repeats.

Upon initiating the rocket's liftoff, the Ground Station sends a corresponding message to the Transmitter, which is then forwarded to the Receiver. After receipt of an acknowledging data

packet from the Receiver, the Transmitter terminates the power signal, causing the device to enter the Fault state. Subsequently, the Transmitter is moved away from the rocket, and the rocket's liftoff is initiated. The whole charging sequence is repeated when conditions of the Initial State are met.

## 3.3    Software Architecture

Software architectures of the Transmitter and the Receiver are depicted in Fig. 21 (a) and (b), respectively. These diagrams represent the connection (from bottom to top) of signals, MCU peripherals, interrupts, and SW functions, which ensure the device functionality outlined in the previous sections. Arrows mark the direction of information flow.

At the very top is the Charging Sequence Evaluation, which implements the state diagram from 3.2. The individual diagrams are organized into larger blocks based on their functionality within the program corresponding to 3.1. Most blocks, such as Communication, Fault State Detection, and Measurement, are common for both Transmitter and Receiver. On the other hand, the Output Control block is present only in the Transmitter.

Layer "peripherals" contains peripherals corresponding to STM32F334C8T6 MCU [42]. This MCU was selected because it met the application's requirements and provided all necessary peripherals, including CAN and multiple UART units, but critically, the high-resolution timer (HRTIM), which enables fine control of switching frequency. Layer "hardware-related functions", shown above the "peripherals" in Fig. 21, represent functions directly controlling these peripherals. Higher layers represent the main and auxiliary functions of the application.

The Communication Block consists of its main functions, Communication with the Transmitter or Receiver and the Ground Station or the Head Unit. The ASK Modulation controls the switching of an additional load in the ASK Modulator in regular time intervals specified in 2.6.3. For that purpose, a compare unit is used; specifically, the HRTIM compare unit, for better resolution to assure smooth regulation as described in 2.5.2. FSK modulation adjusts the switching frequency of the Transmitter's Inverter, obtained by the output voltage control. For the demodulation, both ASK (Transmitter) and FSK (Receiver) use HRTIM capture units which trigger an interrupt when detecting the edge of a connected signal, where further processing is done. For ASK, the capture unit counts the number of transitions of the demodulated signal within the ASK period, while for FSK the capture unit is utilized to measure the frequency of the pre-processed signal as described in [39].

The Measurement Block consists of both devices' current, voltage, and temperature measurements. Measurements are taken at regular time intervals controlled by Timer 2, which are divided into two priority levels. The critical measurements, such as current and voltage, are taken with higher frequency, while the surface temperature of the coils is measured less often as it does not require frequent monitoring. The measured values are distributed to Fault State Detection or Output Control.

The Fault State Detection block evaluates potential faults based on the measured current, voltage, temperature, and the current state of the charger. To catch fast fault events within the Transmitter in case of a short circuit current or any non-operational faults, the Comparator Unit (COMP) is used. The first COMP input is the same as the ADC2 input where current is measured. The second input of the COMP is the output of the Digital-to-Analog Converter Unit (DAC) which output voltage value serves as a reference voltage for the comparator. The reference voltage corresponds to the maximum possible input current (a bit higher value than the operational value of the maximum power level). If a fault is detected, the main loop is notified, and appropriate actions are taken to resolve it.

The Auxiliary function Output Update in the Receiver disconnects the BMS and connects Ping Impedance by means of signals "Ping Imp" and "Output EN" controlling the Output Switch. It also updates the status of LEDs.

In terms of the regulation process, it was necessary to define the control variable. The Qi Standard is open in this case. It can be both output power or output current or output voltage. Since the output power is not constant during the charging process of a battery (as described in 2.4.4.1) and based on the requirements (1.3), the control variable is the output voltage. The Output Control block regulates the output voltage level. First, a data packet with a control error sent by the Receiver is processed in the Communication block, and the actual DC current value at the Inverter input is measured in the Measurement block. The new current value is calculated using the actual current value and the control error (according to Qi standard [43]) in the main function of the PID Control Algorithm. The new current value then enters the PID regulator control loops, which returns a new switching frequency value at the end. The Frequency Update function adjusts the Inverter switching frequency based on the frequency value calculated by PID and the FSK modulation from the Communication block. Finally, the HRTIM compare unit is updated to the new Inverter switching frequency.
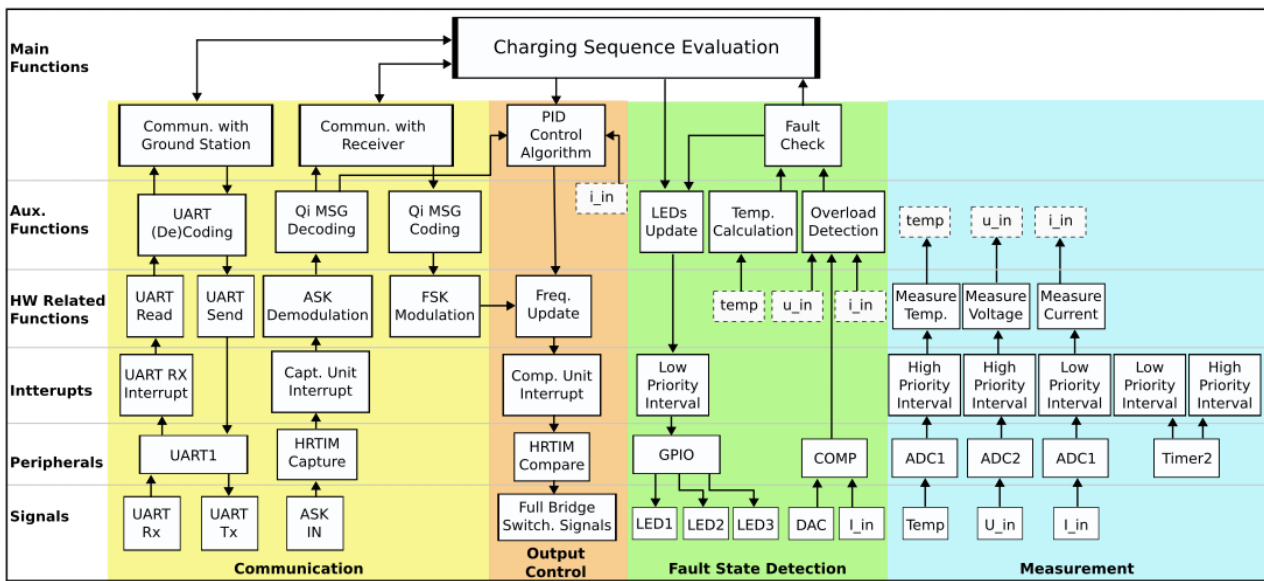


(a)
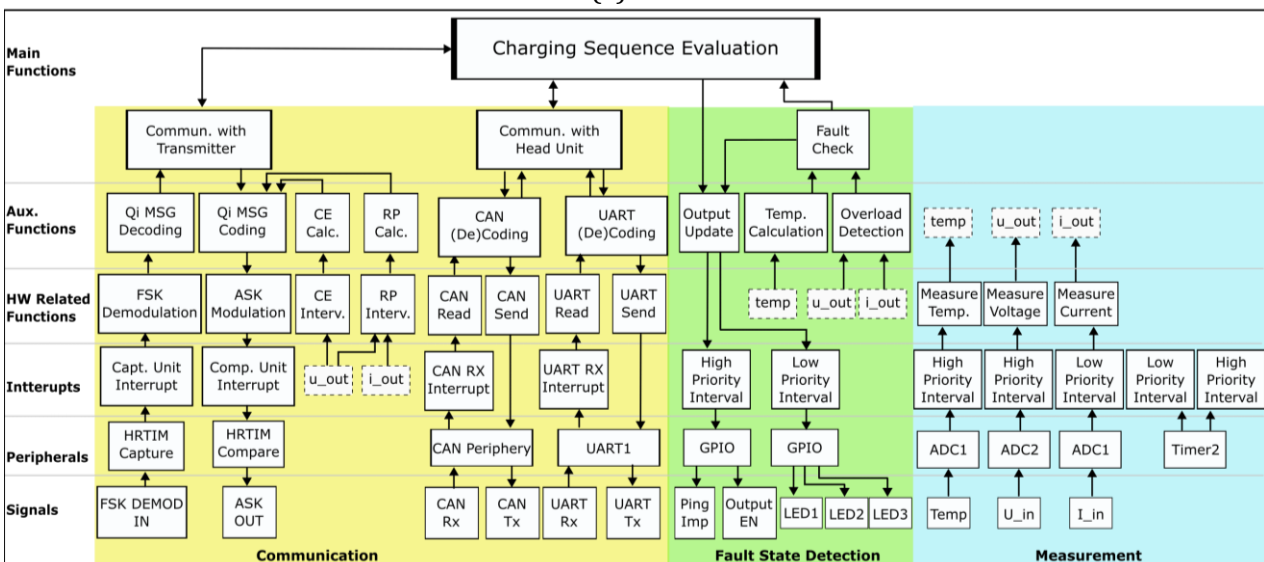


(b)

Fig. 21. The software architecture of (a) the Transmitter (b) the Receiver. The dashed squares with variable name replace connections to make diagram easier to comprehend.

## 3.4　Transmitter and Receiver Positioning

To determine the operating parameters of the wireless power transfer, such as the distance of the air gap and interference of the wireless charger with the surrounding, a simple 3D model was created, which was provided and further processed by the CTU Space Research team members responsible for Receiver and Transmitter positioning within the inner structure of the rocket and the outer construction respectively. In the Fig. 22 is a view of the final 3D Model and the cross-section illustrating the position of the Receiver and the Transmitter within the Rocket and its surroundings. The air gap between the coils is 8 mm.



(a)　　　　　　　　　　　　　　　　　　(b)
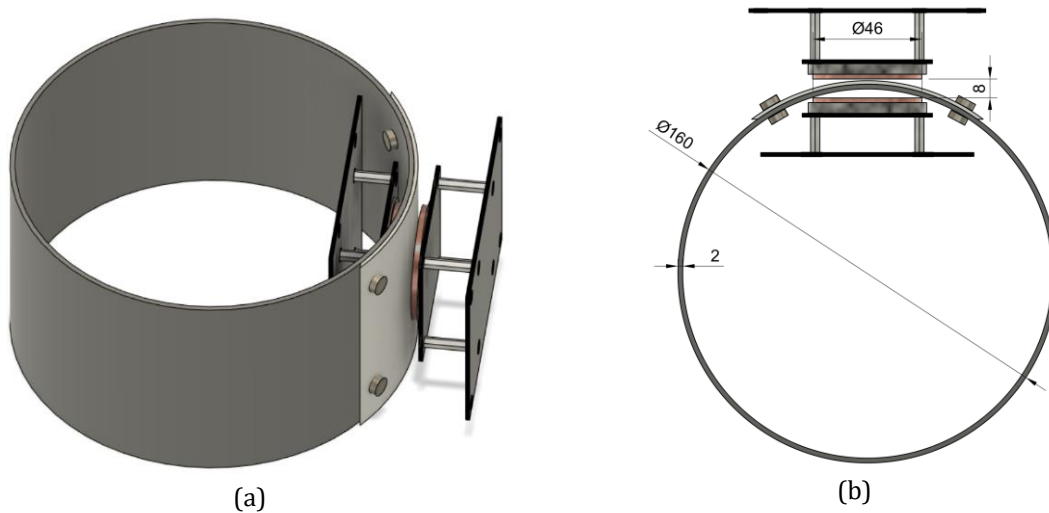
Fig. 22. A model of the positioned Wireless Charger with respect to the rocket. (a) General view. (b) Cross section. Dimensions are in mm.

For the best coupling between the coils, the Receiver coil had to be placed as close to the rocket's shell as possible to minimize the air gap. The PCB layout and board dimensions had to be adjusted to fit in the rocket and reduce the weight and occupied volume. The Receiver is attached to the rocket using the 3D-printed blocks glued to the rocket shell.

The Transmitter is secured to a round plastic cradle that encircles the rocket shell. Four pairs of small neodymium magnets are placed at sufficient distance around the coils to avoid interference with the coils. This combination of magnets and the cradle ensures a stable position of the coils, thereby maintaining a constant coupling coefficient. While developing the wireless charger, a structural team worked on a mechanism that would detach the transmitter from the rocket during launch, but the final design had not been determined at the time of writing this thesis. Nevertheless, several designs were proposed during our meetings, and the options were restricted by the EUROC regulations governing the competition in which the rocket would compete. Construction beyond the launch pad was prohibited, limiting the solutions for the separating mechanism. One proposal was a spring-loaded mechanism that would create a force greater than that of the alignment magnets, pushing the transmitter to a safe distance from the rocket. The transmitter would be attached to a movable unit with pipes that pressurize the fuel tanks, which must also be detached during launch, and this unit would be moved away on the string stretched between the ground and the launch structure.

In addition to adjusting the dimensions of the wireless charger to suit the rocket's environment, it was also necessary to consider the aerospace environment when selecting components for the PCB design. The design had to be as lightweight as possible and simultaneously solid enough to withstand the vibrations during the launch of the rocket. For that reason, the number of screw connections had to be minimized, and only connectors with a lock system were picked to ensure that connections were safe and secure.

# 4 IMPLEMENTATION OF THE DESIGN CONCEPT

In this section, the implementation of the design concept will be presented. The implementation is divided into individual functional blocks of the wireless charger. The order of individual subsections is based on the importance of individual functional blocks to initiate a power transfer.

The schematics relevant to the functional blocks and the main idea of the SW function and initialization are presented. The code itself is not shown in this section to save space but is available for viewing in the appendix together with the PCB layout and complete schematics.

To realize the proposed design architectures, various manufacturers' solutions in the form of reference designs were researched. These reference designs inspired some functional blocks of the wireless charger, while others were developed from scratch. The wireless charger parameters were determined based on the system requirements.

Furthermore, an optimization method described in 2.5 was used to determine circuit parameters such as the input voltage and the geometry of the coils.

## 4.1 Voltage Supply & Protection

The Transmitter is powered through the External Voltage Source, which is connected to the Transmitter's Input Voltage Stabilizer through the J2 connector, as shown in Fig. 23. The SMD fuse holder F1 contains a fast fuse with a nominal current rating of 1.5 A to protect against short circuits. If the input voltage is connected in reversed polarity, the current will flow through the fuse F1 and a Zener diode D7, causing the fuse to burn out and disconnect the input from the voltage supply. In the opposite direction, this combination also provides overvoltage protection, causing the fuse to burn out if the voltage exceeds the Zener voltage of the D7.

The LDO regulator IC3 provides an auxiliary voltage of +3.3V for all ICs within the Transmitter board. The same regulator is used in the case of the Receiver, as depicted in Fig. 24. The regulator's input voltage is stabilized using a pair of ceramic capacitors with 10 and 0.1 µF capacity. Tantalum and ceramic capacitors with 100 and 0.1 µF capacity, respectively, are placed at the regulator's output. The diode D8 protects the LDO regulator when the board is supplied from an external source connected directly to +3.3 V. Resistor R3 and low-current diode LED9 provide a visual indication that the power supply is connected.
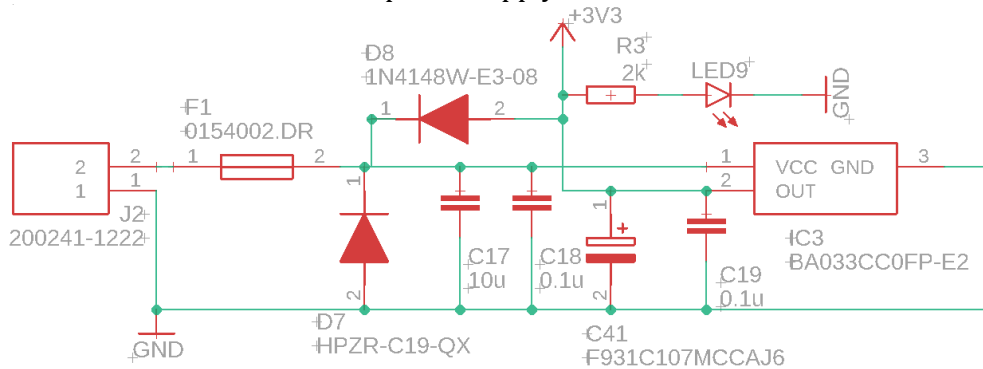


Fig. 23 Transmitter power input & protection.

In the case of the Receiver, the components used for the Input Voltage Stabilizer and the Auxiliary Voltage Supply are almost identical. However, since the gate drivers IRS2008SPBF require a higher voltage than +3.3 V for generating switching signals for MOSFETs, an additional voltage supply PS1 is placed between the Input Power Connector and the LDO regulator IC5. It is a non-isolated DC-DC converter SRH05S12 of 12 V DC output voltage and wide input range. The benefit of the converter is its compact size, thanks to the convenient SIP-3 package. Between the wire VCC_PROTECTED and INVERTER_IN is a measuring block described in Fig. 24.
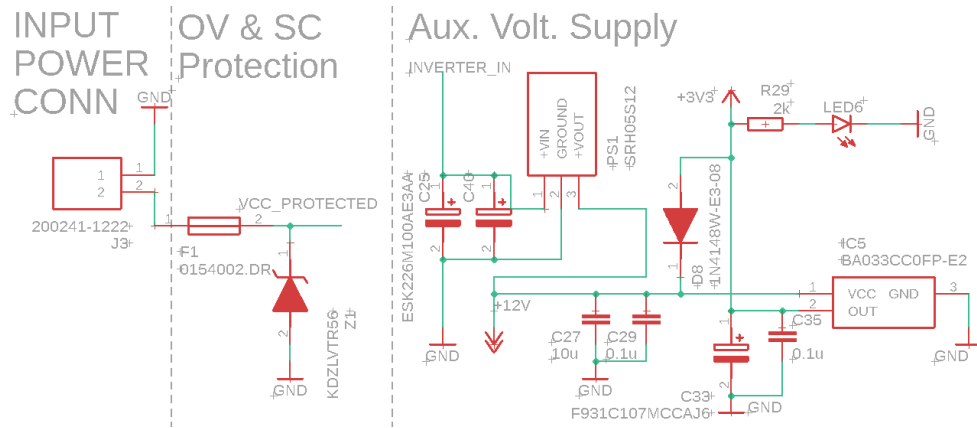
Fig. 24 Receiver power input & protection.

## 4.2    Inverter & Primary Compensation

The full-bridge inverter in Transmitter uses the selected MOSFETs IPD050N10N5ATMA1, which are switched diagonally with a duty factor of 0.5 and a constant deadtime of 520 ns. The inverter input is 48 V DC from External Voltage Source. MOSFETs are controlled by two half-bridge drivers IRS2008SPBF. The inverter supplies the Primary Resonant Circuit, which includes three compensation capacitors: C18, C20, and C21, with a total value of 71.6 nF and a transmitter coil (further described in 4.4), connected to a connector terminal J1 and placed above the transmitter PCB as depicted in Fig. 22. The capacitors in both the Transmitter and Receiver were picked to establish a resonant frequency as close to 100 kHz as possible within the tolerance specified by the manufacturers.
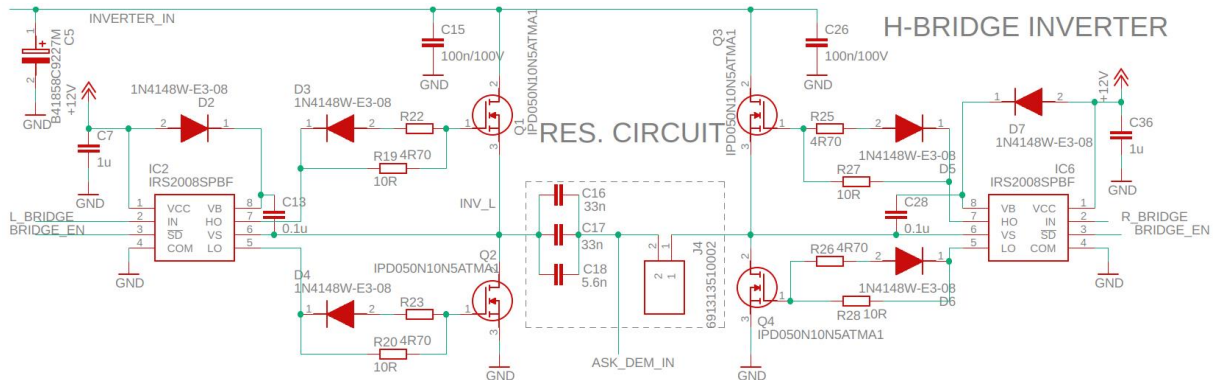


Fig. 25 The Inverter, Gate Drivers, and Primary Resonant Circuit of the Transmitter.

The Switching signals L_BRIDGE and R_BRIDGE are directly connected to the MCU, and those are the output pins of the Timer C within the HRTIM1 – channels TC1 and TC2. The HRTIM1 clock is set to 144 MHz which is further multiplied by 32. In this configuration, the resolution of the timer is 217 ps which is the maximal possible. The TC1 and TC2 Outputs are set as complementary with "half mode" enabled, i.e., the generated signals are inverse square waves with constant duty cycle 0.5. The switching signals are controlled inside the code using the HAL library, specifically the HAL_HRTIM functions. When switching signals L_BRIDGE and R_BRIDGE are configured, the output of the gate driver is finally allowed by setting the BRIDGE_EN signal to HIGH, which results in transferring the complementary square wave signals to switching signals of the required shape and a constant deadtime of 520 ns.

## 4.3    Rectifier, Secondary Compensation & Output Switch

Fig. 26 depicts the Secondary Resonant Circuit consisting of two capacitors of a total value of 69.5 nF and a resonant coil connected to terminal J4 (see 4.4). The full-wave rectifier consists of

the selected Schottky diodes MBRS360 with low forward voltage drop and a pair of 10 μF filter ceramic capacitors. Rectifier output is then connected to the Output Voltage Stabilizer block (see Fig. 19) and consequently to the Output Switch at the Receiver output (Fig. 26 b).

The Output Switch enables fast switching over between the Ping Impedance of 560 Ω (R7) and the load, which is the BMS of the rocket. The BMS is connected directly to the J1 connector. When the p-channel MOSFETs Q4 and Q2 controlling the output bases are not grounded by Q5, the Output Switch is in the OFF state preventing current from flowing to the Receiver even when the battery voltage is higher than the voltage at Rectifier output (i.e., when the battery is fully charged, and Ping Impedance is connected). Q5 is controlled directly from the MCU output pin. To protect the p-channel MOSFETs from high voltage between gate and source, the Zener diode in parallel with R38 is used. The Ping Impedance is connected to the Rectifier output using a Q3 MOSFET TSM120N06LCP_ROG. This MOSFET does not require a gate driver and can be controlled directly from the dedicated output pin of the MCU as well.
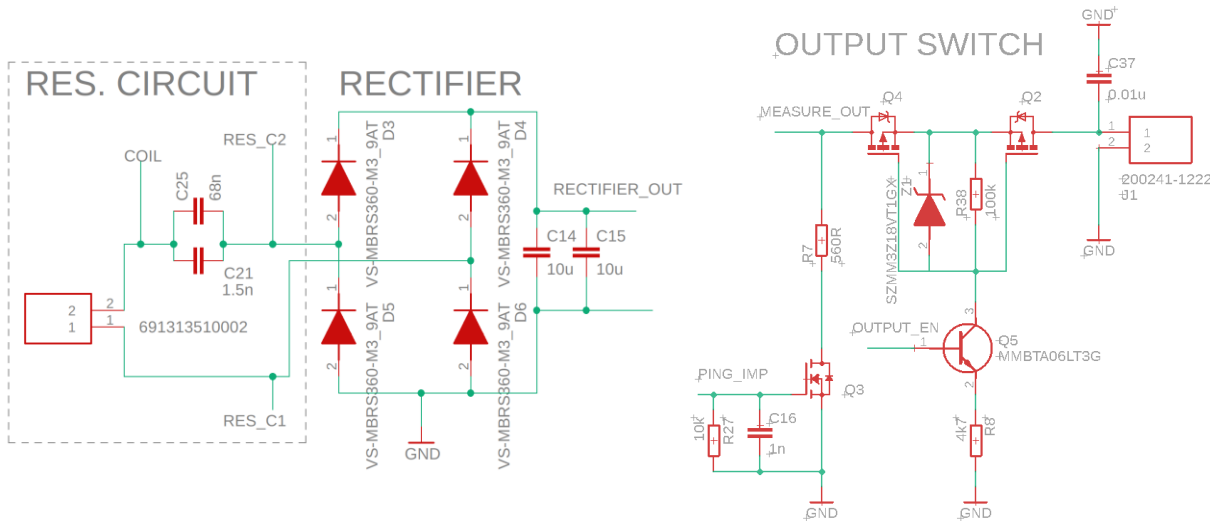


Fig. 26. The power circuits of the Receiver: (a) the Secondary Resonant Circuit and the Rectifier. (b) The Output Switch.

Since the Output Switch is realized using two separate circuits – one (dis)connecting the Ping Impedance and the second (dis)connecting the output, it can be controlled separately. This is useful in case of transition between the state where Ping Impedance is connected and the output will be connected and vice versa. The transition is realized that initially, one of the Ping Impedance or output is connected, then for a short while (1 ms), both are connected, and the transition is completed by disconnecting the other. The disadvantage of such a solution is that inside the code, it must be handled that one of the switches is always in the ON state. Otherwise, the Receiver would be unloaded, and the output voltage of the Rectifier could potentially rise before reaching the Zener voltage of Zener Diode Z2 connected between the output of the Rectifier and Measuring Circuits (not present in the figures, check the appendix for the complete schematics).

## 4.4    The Wireless Charging Coils

The coils are an essential component of the Resonant Circuits in the wireless charger. Their dimensions were determined through an optimization method explained in section 0. Since the parameters are specific for this application, the coils had to be wounded from scratch. However, we needed specific ferrite pads before running the optimization, which proved difficult to find. Despite our efforts to source the pads individually, we couldn't find any that met our requirements. Consequently, we decided to get commercially available coils, separate the windings from the ferrite pads, and use them to rewind Transmitter and Receiver coils.

We have separated the ferrite pads from the 760308100110 coils manufactured by WE [44] to be used as the magnetic cores for the coils. The dimensions of the pad were suitable for our needs. The pad's thickness of 3.2mm ensured overall robustness for further manipulation and rewinding.



(a)                                                            (b)
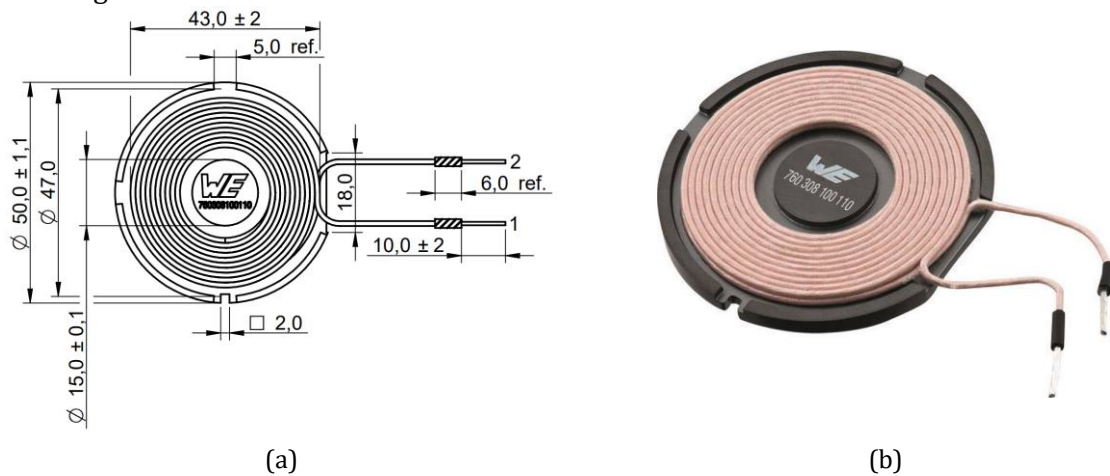
Fig. 27 The Original coil 760308100110 from WE which ferrite pad was used for the rewinding process. (a) Dimensions of the coil. (b) A picture of the coil. Source [44].

## 4.4.1    Coils Geometry from the Optimization Method Results

After the ferrite pads were known together with other input parameters described in 0, the optimization method was run. The optimization method results concerning the parameters of the coils are specified in the Tab. 4-1.

Tab. 4-1 Optimization Results – Parameters of the Transmitter and Receiver Coils

| Type of Coil | Receiver Coil | Transmitter Coil |
|---|---|---|
| Coil Inductance* [µH] | 36.5 | 35.5 |
| ESR [mΩ] | 166.9 | 163.5 |
| Quality factor [-] | 136.6 | 137.3 |
| Number of Turns per Layer [-] | 15 | 13 |
| Number of Layers [-] | 2 | 2 |
| Inner Radius of the Coil [mm] | 4.5 | 7.2 |
| Outer Radius of the Coil [mm] | 24.5 | 24.5 |
| Total Length of the Wire [m] | 2.6 | 2.55 |
| Nominal Diameter of a Single Wire [mm] | 0.1 | 0.1 |
| Number of Individual Wires [-] | 90 | 90 |

* The self-inductance of the single coil was measured in a position where coils were aligned and the terminals of the second coil were open.

The coil geometry defined by the results of the optimization method were used for rewinding the coils (described in 4.4.3). Additionally, the coil inductances from were further used to determine the capacity of the capacitors within the resonant circuits (see 4.2 and 4.3) and to create a simulation model (see 5.1).

## 4.4.2    Modeling in ANSYS

The coil arrangement with the winding parameters from the Tab. 4-1 and the ferrite pad from 760308101141 was modelled using ANSYS Maxwell to verify the coil inductance values and

magnetic flux density values in ferrites (Fig. 28). The air gap between the coils 8 mm was taken from the 3D model of the device described in 3.4. Certain modifications, such as modelling the ferrite without cut-outs or using lumped winding, were applied to speed up the simulations. The simulation also included the surrounding components, such as the rocket shell and the Transmitter cradle, but they were omitted from the view for clarity.



<div align="center">(a)        (b)</div>
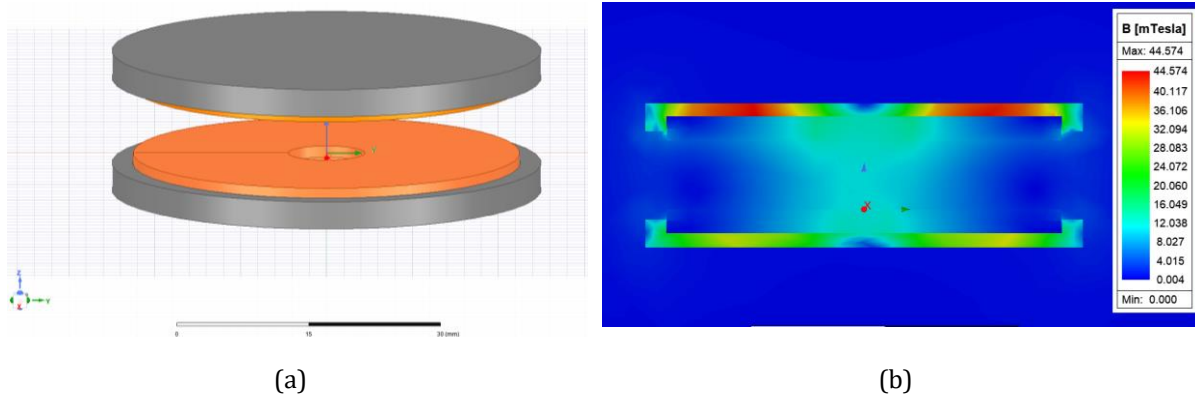
Fig. 28. Ansys Model of the Transmitter and the Receiver Coils. Note that the Transmitter is at the top. (a) The 3D model. (b) Magnetic flux density in section of the coils.

The simulation was performed for maximal currents within the Transmitter and Receiver coils (3.26 and 1.83A), and a corresponding operating frequency of 166.49 kHz. Resulting inductances of the Transmitter $L_{P\_ANSYS}$ and the Receiver coil $L_{S\_ANSYS}$ are 34.55 and 36.08 µH, respectively. The maximal value of magnetic flux density in ferrites $B_{MAX\_ANSYS}$ is 44.57 mT in the Transmitter's ferrite. The obtained coupling coefficient is $k_{ANSYS}$ 0.48. The primary inductance value $L_{P\_ANSYS}$ differs from the optimization method results by 1 µH, which can be caused by the overall simplifications made in the ANSYS model.

As the optimization results were double-checked using the ANSYS simulations, I could start to rewind the coils to a desired geometry as listed in the Tab. 4-1.

### 4.4.3    Coils Rewinding Procedure

The old winding from the 760308100110 coils needed to be removed first. For that purpose, coils were put in the isopropyl alcohol and left for one day to dissolve the glue that holds together the winding and ferrite pads. After that, the winding was removed from the pad using a knife. The coils were then rewound using a copper Litz wire RUPALIT 90x0.1 from PACK Feindrähte. First, the bottom layer was wound from the center to the outside, followed by a second layer on top. The wire was secured in place using a quick-drying adhesive.

Once the winding was complete, the terminals were done, and the inductance and ESR of the coils were measured using an LCR meter GW Instek LCR-6300 over a frequency range of 100 to 240 kHz, which covers the entire operational range. The coils were aligned, and the air gap between the coils was set to 8 mm. Both the Transmitter and the Receiver coils were measured, with the second coil having open terminals. To determine the coupling coefficient, another measurement was performed with measuring clamps connected to the Transmitter and the Receiver coil terminals shorted. In the Tab. 4-2, there are measured values relevant to the operational range.

For the operation range, the values of $L_p$ ranges from 35.82 to 35.86 µH the values of $L_s$ ranges from 35.17 to 35.2 µH. Compared to the values obtained from the optimization method and ANSYS simulation in 4.4.2, the measured inductances are close to the calculated and simulated values. Although the simulation and optimization results have shown that the inductance of the Receiver Coil should be greater than the inductance of the Transmitter Coil, the measured results show the opposite. This is probably caused by the fact that the actual outer diameter of the real

Transmitter Coil is slightly larger due to the winding procedure than was calculated by the optimization method.

The ESRs of both primary and secondary coils gradually increase from 253 to 374 mΩ and from 256 to 390 mΩ, respectively. The increase in ESR can is caused most probably due to the skin effect and saturation of the ferrite pad. The quality factors $Q_p$ and $Q_s$ ranges from 142.33 to 126.51 and 138.11 to 119.09. Compared to the optimization method results, the measured results show lower values of quality factors due to higher ESR for some frequencies more than two times higher. However, it is worth noting that the optimization method takes one single ESR for all frequencies.

If we compare the measured values with the values of the original winding within the 760308101141 coils [44], the quality factor of the original winding is greater than 200 in this frequency range. The measured quality factor is also smaller because the Litz wire used for rewinding has a smaller diameter than the original, increasing the coil's overall ESR.

Tab. 4-2 Parameters of the Rewound Transmitter and Receiver Coils

| Parameter | Unit | Values | | | | | |
|---|---|---|---|---|---|---|---|
| frequency | [kHz] | 160 | 170 | 180 | 190 | 200 | 210 |
| $L_p$ with secondary open | [μH] | 35.82 | 35.83 | 35.84 | 35.84 | 35.85 | 35.86 |
| $L_p$ with secondary shorted | [μH] | 27.60 | 27.61 | 27.61 | 27.61 | 27.61 | 27.62 |
| $L_s$ with primary open | [μH] | 35.17 | 35.17 | 35.18 | 35.19 | 35.19 | 35.2 |
| ESR of primary | [mΩ] | 253 | 277 | 301 | 326 | 349 | 374 |
| ESR of secondary | [mΩ] | 256 | 283 | 308 | 337 | 363 | 390 |
| $k$ | [-] | 0.479 | 0.479 | 0.479 | 0.479 | 0.479 | 0.479 |
| $M$ | [μH] | 17.00 | 17.00 | 17.02 | 17.02 | 17.03 | 17.03 |
| $Q_p$ | [-] | 142.33 | 138.16 | 134.66 | 131.25 | 129.08 | 126.51 |
| $Q_s$ | [-] | 138.11 | 132.74 | 129.18 | 124.66 | 121.82 | 119.09 |

After the coils were measured and approved, the coils were then glued to the dedicated PCBs. A temperature sensor is located on the other side of the PCB, in the middle. The coils were then filled with epoxy, which better protects the winding and the ferrite edges.

## 4.5 Qi Communication

The internal communication between the Transmitter and the Receiver was implemented on the recommendations of the Qi Standard. Some hardware structures were inspired by available reference designs and others were designed from scratch. The SW implementation of the internal communication is based on the Qi standard documentation.

The ASK modulation and demodulation were successfully implemented and tested, as described further in this text. The FSK preprocessing circuit and hardware peripherals were also successfully implemented. However, the SW implementation was not fully completed by the deadline for submitting this work, as the FSK demodulation became more complicated than initially proposed. However, FSK Demodulation is expected to be fully configured before the rocket's wireless charger is fully implemented into the rocket.

### 4.5.1 Implementation of ASK Modulation and Demodulation

The ASK Modulator circuit in Fig. 29 (a) is linked to the Receiver's Resonant Circuit (pins COIL and RES_C2, see Fig. 26). MOSFETs Q7 and Q8 switch the capacitors C11 and C12 to ground, altering the total impedance of the Secondary Resonant Circuit. The capacitor values were selected to meet the Qi Standard, ensuring that the amplitude difference of the Transmitter coil voltage in the HI and LO states is at least 200 mV. Both capacitors are simultaneously switched at a frequency of 2 or 4 kHz during the communication [39].

(a)                                                                 (b)
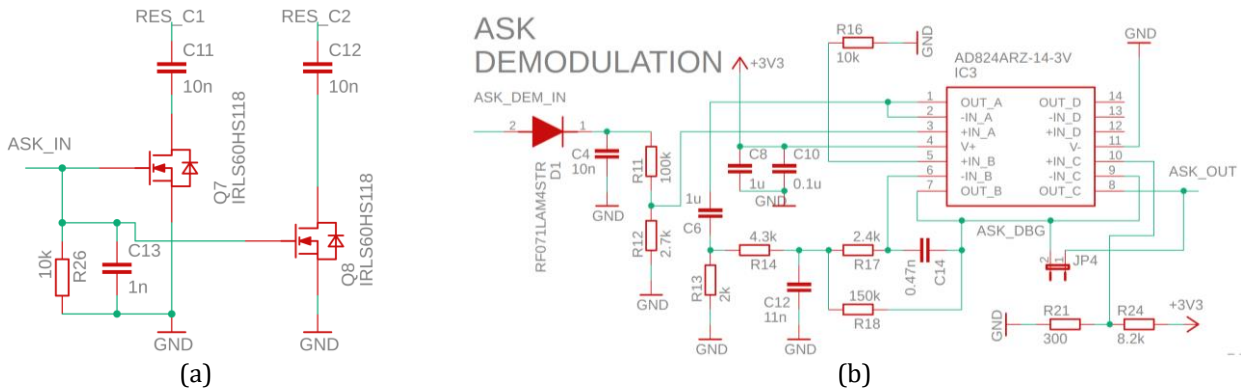
Fig. 29. (a) The ASK Modulator in the Receiver. (b) The ASK Demodulator in the Transmitter.

The ASK Demodulator in Fig. 29 (b) was inspired by [45]. The purpose of the circuit is to convert the high-frequency ASK modulated signal at the input to the low-frequency square wave corresponding to the input signal envelope, with voltage levels that the Transmitter's MCU capture unit can accept. The integrated circuit AD824ARZ-14-3V labeled as IC4, is a four-channel precise operational amplifier that is used in the following sequence. At first, the voltage on the coil ASK_DEM_IN is rectified using diode D7. The capacitor C9 is charged to the voltage level equal to the amplitude of the coil if a positive wave is present otherwise, the voltage on the capacitor slowly decreases as it discharges through the voltage divider consisting of R9 and R14. The lowered voltage from the voltage divider enters the first channel of the amplifier which is wired as a voltage follower. The signal then enters a high-pass filter formed of C12, and R26 which takes out the DC offset of the signal. Next, a signal is filtered from the high-frequency noise using a second-order low-pass filter formed of R28, C13, R29, R33, and C22, entering the input of the second channel of the amplifier. The final stage is to transfer the signal to a square wave using the third channel used as a comparator, where the reference voltage level for the comparator is defined by the voltage divider formed by R34 and R35. The fourth channel of the amplifier is not used.

### 4.5.1.1   ASK Message Structure

Individual data bits are encoded using as described in 2.6.3 by switching the C11 and C12 capacitors. The individual data bits are sent in bytes using the following format defined by the Qi standard documentation. One data byte is encoded using an 11-bit asynchronous serial format, consisting of a start bit, the 8 data bits of the byte, a parity bit, and a single stop bit. The data bits are in LSB first order. The start bit is always ZERO, and the parity bit is set to ONE if the number of ONES inside the transmitted data byte is even. Stop bit is always ONE. All 11 bits are sent in a contiguous sequence without a pause between two consecutive bits.
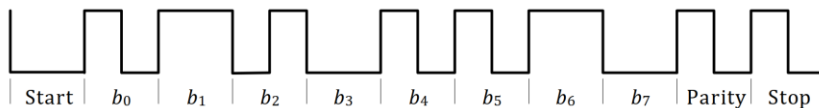


Fig. 30 Example of ASK Modulated byte. Source [37].

The data bytes are packed in a data packet encoded according to the [37] and sent as a contiguous sequence. The data packet consists of 4 parts, as depicted in Fig. 31 of a minimum length 4 and a maximum 24 bytes total.

| Preamble | Header | Message | Checksum |
|----------|--------|---------|----------|
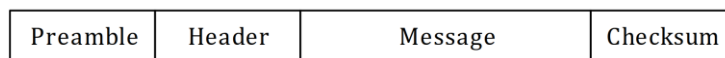
Fig. 31 ASK data packet format. Source [37].

The first part is called a preamble and it is a series of a minimum 11 and a maximum of 25 ONES. The preamble lets the Power Transmitter know about the incoming message and stabilizes

the transients within the demodulation circuit. The length of the preamble was set to 22 bits as it assures best the stabilization of the demodulation circuit.

The second part – the header, is an identifier of the incoming data. The header length is 1 byte, and its value indicates the data packet type and, in addition, the overall size of the data packet. The documentation [36] contains a table of all pre-defined header types.

The third part is the actual message. This is the part of the packet where the main information is stored. The size of the message can be from 1 up to 20 bytes long. The message has its own structure, different for different header types, defined by [36].

## 4.5.2 Implementation of the FSK Modulation and Demodulation

The FSK Modulation is realized by software in the Transmitter MCU. The Power Signal frequency is switched between the frequency in modulated $f_{mod}$ and the unmodulated state $f_{op}$ (the standard operating frequency). The Qi standard defines the difference between the $f_{mod}$ and $f_{op}$ using the two parameters: Polarity and depth. Polarity defines whether the difference between those two frequencies is positive or negative. Depth (also modulation depth) determines how different those two frequencies are in magnitude. There are a total of 4 different predefined depths described in the Fig. 32.

| Polarity | Depth | $\frac{1}{f_{\text{mod}}} - \frac{1}{f_{\text{op}}}$ | | Unit |
| --- | --- | --- | --- | --- |
| | | Minimum | Maximum | |
| positive | 3 | -282.00 | -249.00 | ns |
| positive | 2 | -157.00 | -124.00 | ns |
| positive | 1 | -94.50 | -61.50 | ns |
| positive | 0 | -63.25 | -30.25 | ns |
| negative | 0 | 30.25 | 63.25 | ns |
| negative | 1 | 61.50 | 94.50 | ns |
| negative | 2 | 124.00 | 157.00 | ns |
| negative | 3 | 249.00 | 282.00 | ns |

Fig. 32 Different modulation depths in FSK. Source [36].

Setting a larger modulation depth may result in better reliability of the communication channel. However, it can affect the quality of the regulation process and voltage ripple on the receiver's output. A smaller modulation depth can be problematic for demodulation. The demodulator should be capable of distinguishing between the minimum difference of 30.25 ns corresponding to the 0-modulation depth.

The circuit in Fig. 33 operates as the FSK pre-processing for the FSK demodulator in the Receiver's MCU. It is connected to the Receiver coil (pins COIL and RES_C1, see Fig. 26). Its purpose is to filter any high-frequency noise using a low-pass filter (R4, R6, and C24). Second, to convert the sine voltage at the coil into a rectangular signal with the same frequency and reduced voltage levels. This voltage then enters the differential analog comparator that adjusts the voltage levels further to enable processing in the MCU capture unit which demodulates the signal.
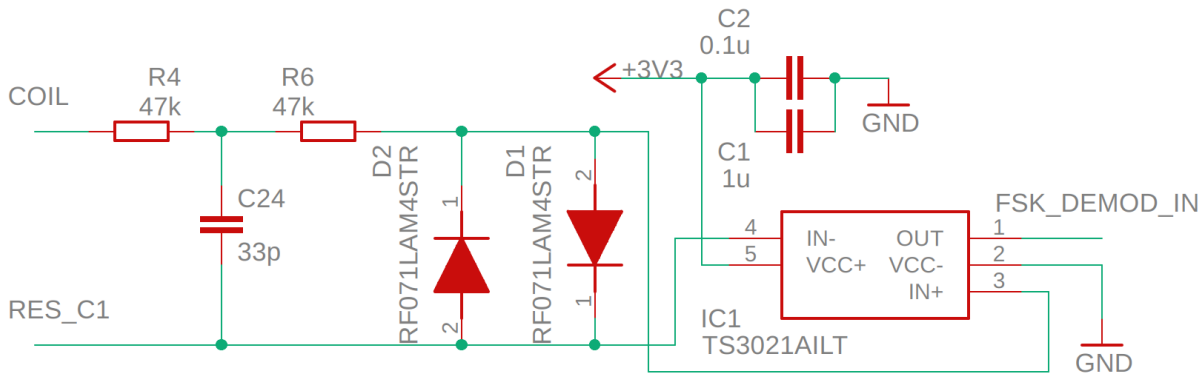
Fig. 33. The FSK Preprocessing for Demodulation.

### 4.5.2.1 FSK Message Structure

The 11-bit asynchronous serial format is used to transmit a single data byte. The first bit is a start bit, always equal to ZERO, then follows a series of the 8 data bits of the byte, a parity bit, and a stop bit. Unlike the ASK modulation, the parity is even, which means that the parity bit is set to ONE if the data byte contains an odd number of ONE bit. The stop bit is always set to ONE. In the Fig. 34, we can see an example of the described data byte format, including a start bit, data byte (0x35 value as an example), parity bit (ZERO in this case), and a stop bit. The bytes are sent in a contiguous sequence without a pause between two consecutive bytes.
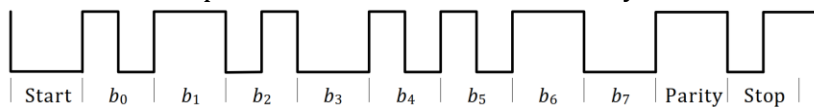


Fig. 34 Example of FSK Modulated byte. Source [37].

A data packet in which the Transmitter wraps the data to be sent to the Receiver consists of a series of bytes sent in a contiguous sequence. The data packet consists of a header – an identifier of the following bytes, the message – the actual data which were supposed to be sent and the checksum – a control sum to determine the consistency of the data packet.

The predefined headers by the Qi standard and their message structures are available in the standard's documentation [36]. The message length can be from 1 to 27 bytes.

### 4.5.3 Communication Hierarchy

From the hierarchy point of view, the Receiver is always the initiator of the communication within the IPT device. This means that the Receiver initiates all data packet communications, and the Transmitter waits to send a data packet until explicitly invited to do so (in regular intervals). The hierarchy helps to avoid mishearing during communication,

The communication hierarchy within the standard can be described as follows:

- Communication within the Qi standard is initiated by the receiver, which sends data packets to the transmitter to adjust the parameters of the Power Signal.
- The Transmitter responds to the Receiver's data packets using a response pattern if needed.
- The Receiver may open a communication canal anytime to transfer auxiliary or user data to the Transmitter using a proper data packet.
- The Transmitter may open a communication canal using a specific response pattern direction only in response to certain data packets sent in regular time intervals by the Receiver. After the communication canal is open, the Transmitter can send the requests or auxiliary or user data to the Receiver [36].

38

The response patterns are simple data packets of only 8-bit size, which the Transmitter uses to respond to certain data packets sent by the Receiver.

In some cases, the Receiver needs to ensure that the data packet was received correctly or the Transmitter made the adjustments proposed in the sent data packet. Four response patterns are defined in the documentation: ACK, NAK, ND, and ATN.

The ACK is a shortcut for "acknowledged" and is mostly used to confirm that the data packet has been processed properly, or if the data packet was a request, then ACK confirms the suggested request. The opposite of ACK is NAK, and it is a shortcut for "not acknowledged". ND is a "not defined" and is often used as a response that a suggested change is not supported within the current power transfer stage. The last response pattern, ATN, stands for "attention" and is used if Transmitter wants to send data to the Receiver. During different operation phases of the wireless charger, several data packets are sent in regular time intervals to which Transmitter may respond with the ATN response. The data transport stream follows, which example can be seen in the Qi Standard documentation [36].

## 4.6    Outer Communication

The Transmitter and Receiver contain a UART to RS485 converter, as shown in Fig. 35 (a). The processor's UART_RX and UART_TX signals are connected to the half-duplex RS485 transceiver. These signals can be observed using an oscilloscope by connecting probes to the JP2 jumper for debugging purposes. The RE and DE pins alternate the output state of the LTC485S between the driver output enable and the receiver output enable. These complementary inputs are connected to and controlled by the MCU. R22, like R16, is a terminating resistor in series with a solder jumper that can be used if the terminating resistor is required elsewhere. During the design of these circuits, the exact topology of the communication networks was unknown, which is why the solder jumpers are included.

The CAN transceiver depicted in the Fig. 35 (b) and located in the Receiver has only one output and one input pin routing to the MCU. The resistor R9 is connected between the RS pin of IC2, and the ground controls the steepness of the signal and can be changed during the testing if needed. The CAN Transceiver is set as always on as the SHDN pin is connected to the ground. RS485 and CAN transceivers are connected to surrounding units (Head Unit in case of Receiver and Ground Station in case of Transmitter) via the 50578-0371, the three circuits connectors with Micro-Lock system ensuring safe and secure connections.
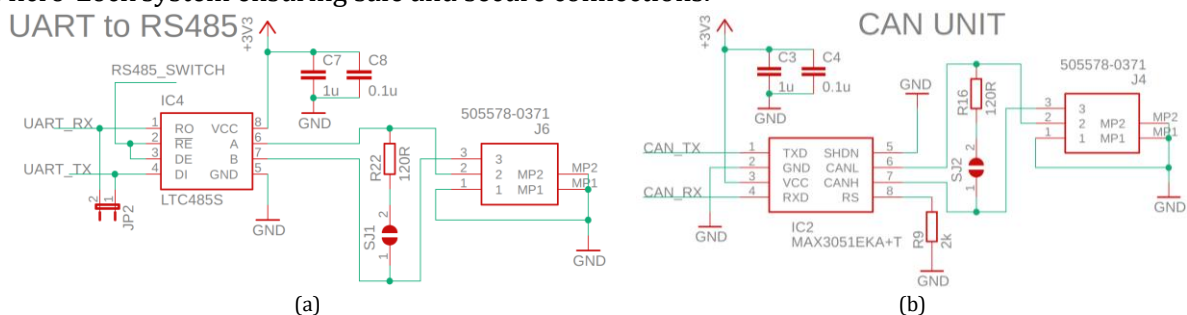


Fig. 35 The outer communication circuits (a) UART to RS485 converter (b) CAN Transceiver

At the time of the realization of this thesis, the communication between the Head Unit and the Ground Station has not yet been specified by the CTU SR. For that purpose, the SW implementation of the outer communication was not yet implemented.

The transmitter and the receiver have another UART interface available for connecting with the PC, which was used for debugging and testing. The Debug UART interface is not shown in the figures, but it can be seen in the appendix, where the whole schematics are available.

## 4.7    Voltage, Current, and Temperature Measuring

The circuits for measuring current and voltage are almost identical for the Transmitter and the Receiver. For clarity, only the Receiver's side is presented in Fig. 36. The current is measured using a shunt resistor and a current sense amplifier INA181A3IDBVR. This amplifier integrates a matched resistor gain network in a fixed-gain 100 V/V, which minimizes gain error and reduces the temperature drift. The voltage is measured using a voltage divider made of resistors that reduces the input voltage to acceptable levels for the MCU's ADC. The Zener diode connected to the rectifier's output (not displayed, see the appendix for a full schematic overview) protects the input ADC pins for the Receiver, while the Transmitter's Zener diode is placed right after the fuse.

Temperature is measured using an LM61BIM3 temperature sensor whose output voltage is linearly proportional to temperature (10 mV/°C) with a fixed offset of 600 mV. The offset allows reading negative temperatures without the need for a negative supply. The temperature sensor is placed in the middle of the other side of the PCB where the coils are located. To ensure sufficient heat conduction in the direction of the sensor, a bunch of vias is placed around it.



(a)                                                        (b)
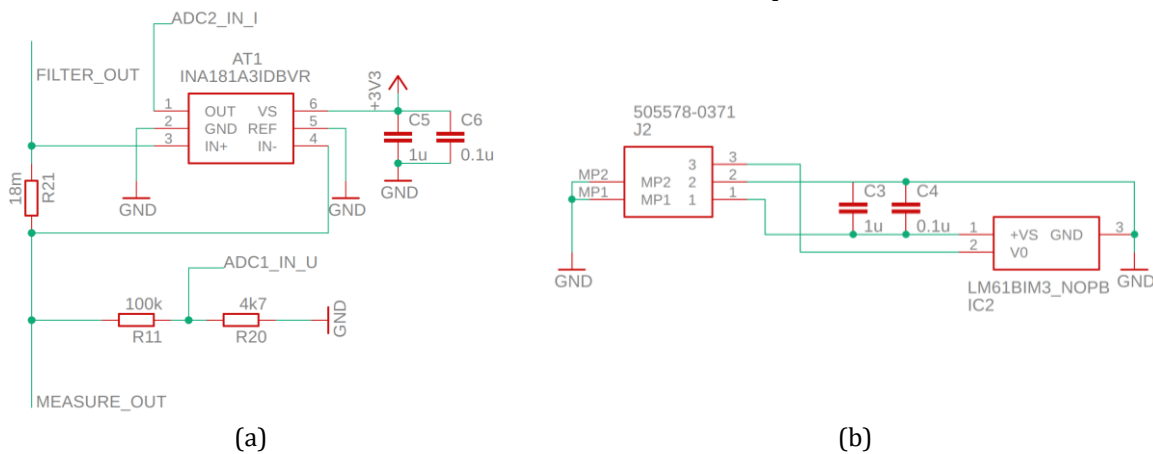
Fig. 36 Measuring Circuits. (a) Current and Voltage. (b) Temperature.

As mentioned in 3.1.2, the measuring is done regularly in two different intervals based on priority. The current and voltage is measured every 25 ms while the temperature is measured once every second. The measured values are obtained as an average of 10 values measured in series. In this 25 ms interval, the measured current and voltage are evaluated to capture a potential fault within the system.

Current and voltage measurement uses two different ADCs to obtain simultaneous values for precise power calculation. For this purpose, a "dual mode" was set in the ADCs configuration, assuring that two ADCs sample the input at the same time. The temperature uses ADC 1, the same as the voltage measurement. The current is measured on ADC 2.

Each measuring circuit was adequately calibrated to eliminate reading errors.

## 4.8    Implementing the PID Control Algorithm

The regulation process was inspired by the Qi standard PID Control Algorithm [43]. In the Fig. 37 is a diagram of a discrete proportional-integral-differential (PID) algorithm used in Qi with corresponding symbols. This algorithm is implemented in the Transmitter. The control algorithm consists of the superior output voltage (i.e., the output DC voltage of the Receiver) control loop with input current (i.e., the input DC current within the Transmitter) control loop inside it. The controlled variable inside the input current control loop can be the switching frequency of the inverter and the input voltage based on the application. However, in our application, the only controlled variable is the switching frequency.
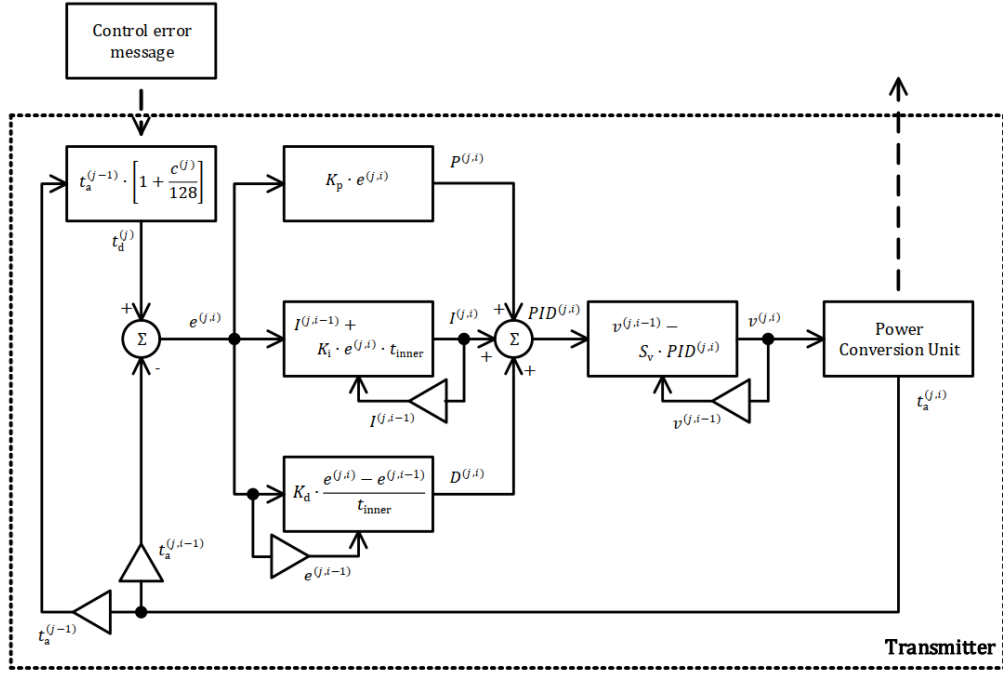
Fig. 37 Diagram of the PID control algorithm by Qi Standard. Source [43].

The input of the algorithm is a control error value from the Receiver. The control error is obtained every $t_{interval}$ (which was set to 250 ms) as a single data packet coming from the Receiver. The control error data packet contains the encoded value of the error between the target output voltage (30 V in our case) and the actual output voltage. The control error is encoded into a single byte with a minimum value of -128 to a maximum of 127. The positive error means the output voltage is less than the target value and the opposite. The standard does not directly define how to calculate the error and is left open to the application.

The control error value $c$ calculation and compressing to a single byte was implemented as follows:

$$c = \frac{V_{target} - V_{actual}}{V_{c\_min} - V_{c\_max}} \cdot 128$$

(4-1)

where $V_{target}$ is the target value of the output voltage (30 V), $V_{actual}$ is the actual voltage on the Receiver's output in the moment the control error is calculated. The range covered by the control value is $V_{c\_min} - V_{c\_max}$.
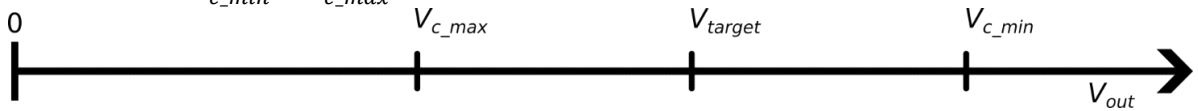


Fig. 38 The voltage range of Control Error value

The range was set so that the resolution of the error is equal to 50 mV. This means that if the error is greater than -50 mV and lesser than 50 mV, the control error is equal to 0. Also, if the control error is beyond the limits of the signed 8-bit integer (-128 to 127), then the control error is equal to the limit value.

The control error is used to calculate the new Primary Coil current as follows:

$$t_d^{(j)} = t_a^{(j-1)} \cdot \left[1 + \frac{c^{(j)}}{128}\right]$$

(4-2)

41

where $t_d^{(j)}$ represents the new target value of the input current, $t_a^{(j-1)}$ is the actual input current and $c^{(j)}$ represents the control error value. The index $j$ stands for the $j^{th}$ control error packet, so the $t_d^{(j)}$ is refreshed every time a new control error packet is received.

Next, if the control error value $c^{(j)}$ is different from 0, the Transmitter shall adjust its input current in a $t_{active}$ (specified as 20 ms) time window. Because receiving a data packet from the Receiver projects in current fluctuation in the Primary Coil, there should be another time window $t_{delay}$ before the primary current control loop is started. The explicit value of $t_{delay}$ is not defined by the standard. However, by measuring the input current fluctuations, the value was set to 100 ms. This value proved to be a long enough period where the ASK Modulation does not affect the current. Simultaneously, enough time is reserved for other communication packets sent between the following two CE packets.

After the $t_{delay}$ comes the series of iterations where the input current is trying to reach the target value of $t_d^{(j)}$ using the PID algorithm loop. The number of iterations is left open, but the control process should be done at the end of the $t_{active}$ time window.

Each iteration consists of calculating the difference between the target Primary Cell and the actual Primary Cell current as the error:

$$e^{(j,i)} = t_d^{(j)} - t_a^{(j,i-1)} \tag{4-3}$$

where $t_a^{(j,i-1)}$ represents the input current measured in the previous iteration. The index $i$ represents the actual iteration. In the first iteration, the $t_a^{(j,0)}$ is equal to the actual input current at the start of the series of iterations.

Next, the Transmitter shall calculate the proportional, integral, and derivate terms:

$$P^{(j,i)} = K_p \cdot e^{(j,i)} \tag{4-4}$$

$$I^{(j,i)} = I^{(j,i-1)} + K_i \cdot e^{(j,i)} \cdot t_{inner} \tag{4-5}$$

$$D^{(j,i)} = K_d \cdot \frac{e^{(j,i)} - e^{(j,i-1)}}{t_{inner}} \tag{4-6}$$

where $K_p, K_i, K_d$ are the proportional, the integral, and the derivate gains and the $t_{inner}$ is the time required to execute a single iteration within the loop. In the first iteration the $I^{(j,0)}$ and $e^{(j,0)}$ are both set to 0.

The Transmitter shall limit the integral term to remain within the restricted range, and if the integral term is outside this interval, it shall replace the calculated integral term $I^{(j,i)}$ with the boundary value.

The individual terms are summed to a single term and limited within the range $(-M_{PID}, +M_{PID})$.

$$PID^{(j,i)} = P^{(j,i)} + I^{(j,i)} + D^{(j,i)} \tag{4-7}$$

Finally, the new value of the controlled variable is calculated as:

$$v^{(j,i)} = v^{(j,i-1)} - S_V \cdot PID^{(j,i)} \tag{4-8}$$

where $v^{(j,i)} = f^{(j,i)}$ is the calculated control variable which is, in our case, the switching frequency of the inverter and $S_V$ is a scaling factor which can be different for different frequency ranges. Typically, in Qi standard reference designs [46], there are 2 to 5 frequency ranges where the scaling factor value ranges from 1 to 5, the larger the frequency is, the larger should be the scaling factor. If the control variable exceeds the given range (corresponding to the operating points of minimum and maximum power levels for example), the control variable is replaced by the appropriate boundary value.

At the end of each iteration, the switching frequency of the inverter is updated with the new value $f^{(j,i)}$ and measure the actual Primary Cell current $t_a^{(j,i)}$.

The customized control algorithm timeline is depicted in the Fig. 39
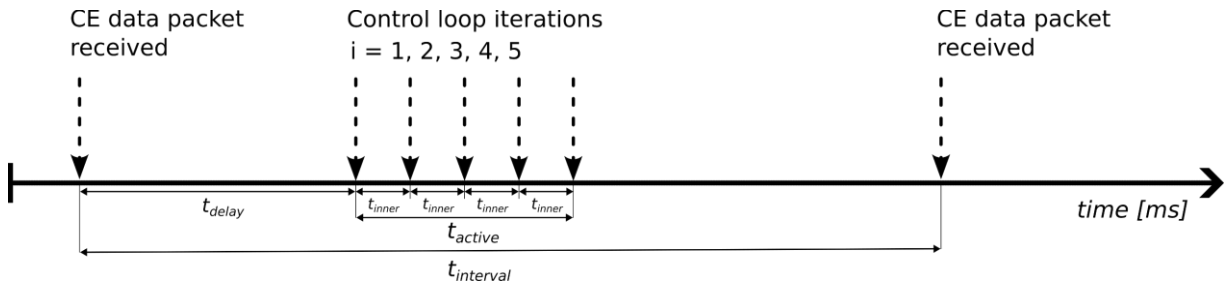


Fig. 39 Regulation process timeline

The number of iterations was set to 5 and $t_{inner}$ to 4 ms. Unlike the Qi Standard, the current is measured at the beginning of each iteration and not at its end. The $K_p, K_i, K_d$ values were achieved using experimentally. First, $K_p$ was increased gradually from zero until the system became unstable. Then $K_i$ was added, and lastly, $K_d$. However, during the tuning of the regulator, it turned out that the system reacted best when the $K_d$ was set to a very low value or equal to zero. The final values of regulator constants were set as follows: $K_p$ = 37, $K_i$ = 6, $K_d$ = 0.1.

## 4.9    The Constructed Wireless Charger

In the Fig. 40 is a top view of the final version of the constructed Wireless Charger. During the device's implementation and testing phase of the device several design issues had to be resolved. The list of the issues is described in Appendix B. In the Appendix C, you will find more pictures of the realized wireless charger. The schematics and PCB layout are in a separate appendix.
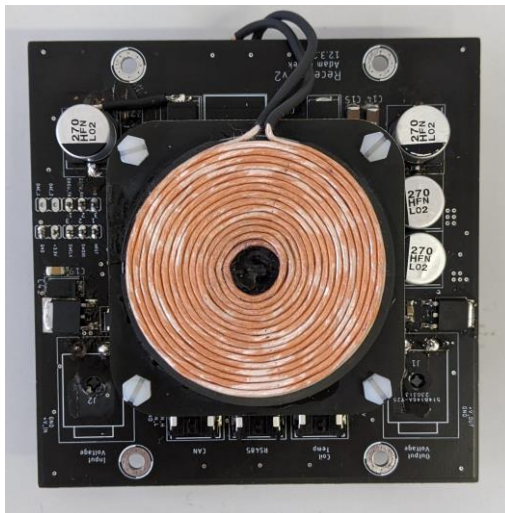


(a)                                                                      (b)

Fig. 40 Top view of the realized wireless charger where (a) is the Receiver and (b) is the Transmitter.

# 5     VERIFICATION OF THE FUNCTIONALITY OF THE DESIGNED DEVICE

This section focuses on the verification of the realized wireless charger design.

First, LTspice model of the wireless charger is introduced, which was used during the design process to verify the validness of the designed circuits focused on ASK and FSK demodulating circuits and the overall power transfer parameters.

Second, the operation of the constructed wireless charger is verified using several scenarios capturing the standard operation of the wireless charger as well as the reaction of the device to several fault states.

Lastly, the power transfer of the constructed wireless charger is tested across the whole operational range. The DC-DC efficiency is measured and compared to the values from the simulations.

## 5.1     LTspice Model

The LTspice model (see Fig. 41) was created to verify the design of the wireless charger. Additionally, the model was used during the testing of the device as it provided a good overview of currents and voltages within the circuits.

The LTspice model was created using the parameters from the optimization method, such as inductances of the Transmitter and Receiver Coils and the capacities of the Primary and Secondary Resonant Circuits. The ESRs of both coils and capacitors were also obtained using optimization. Models of MOSFETs within the Inverter were downloaded from the manufacturer's website, while the Schottky diodes from the Rectifier were already part of the LTspice library.

Only the most significant functional blocks were added to the simulating circuit. Some components were simplified for faster generating of simulation results. For example, gate drivers were reduced to voltage sources and input and output voltage stabilizers to a single capacitor with the equivalent capacity. The load is simulated with equivalent load resistance, which value is set before starting the simulation and variable switching frequency of the Inverter.
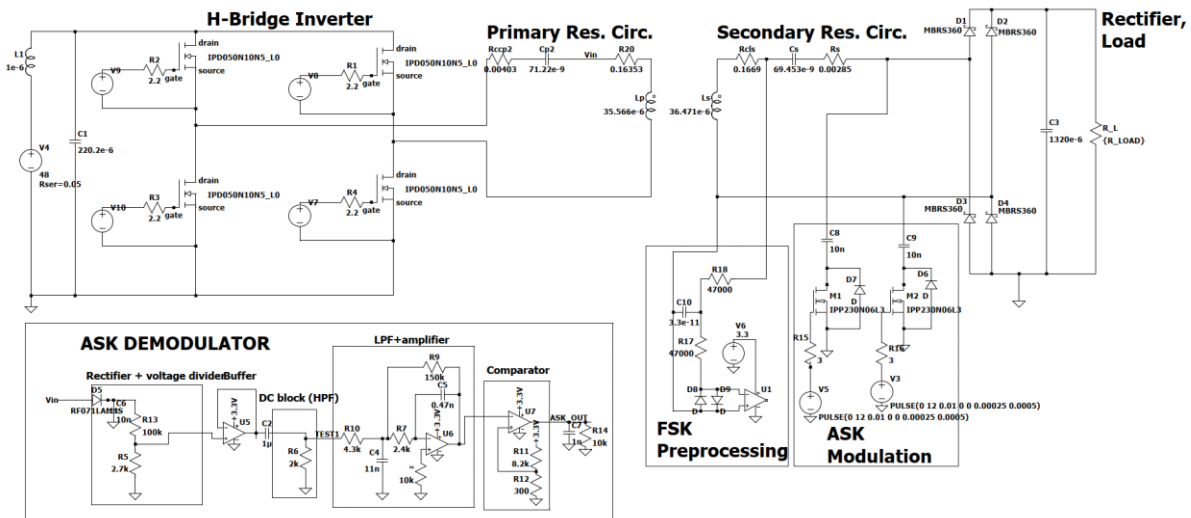


Fig. 41 LTspice simulating circuit.

This LTspice model was mainly used to verify and tune individual components' values within the Qi communication circuits, as described in 4.5. Two simulations were performed to verify the ASK Demodulation and FSK Preprocessing circuit with the final values. For better comparison, the operational characteristics, such as the DC-DC efficiency and the switching frequency for various loads within the operational range, are captured in Fig. 52, together with the measured values of the constructed wireless charger.

### 5.1.1 Simulation 1: ASK Demodulation

The performance of the ASK Demodulator in was evaluated under minimal $P_{outDC}$ of 1.5 W and nominal $P_{outDC}$ of 30 W. To simplify the test, the modulated data bits comprised a series of continuous "ONES" encoded according to the encoding scheme described in [39]. Fig. 42 shows the voltage on the Transmitter coil and the demodulated signal captured during the simulation.
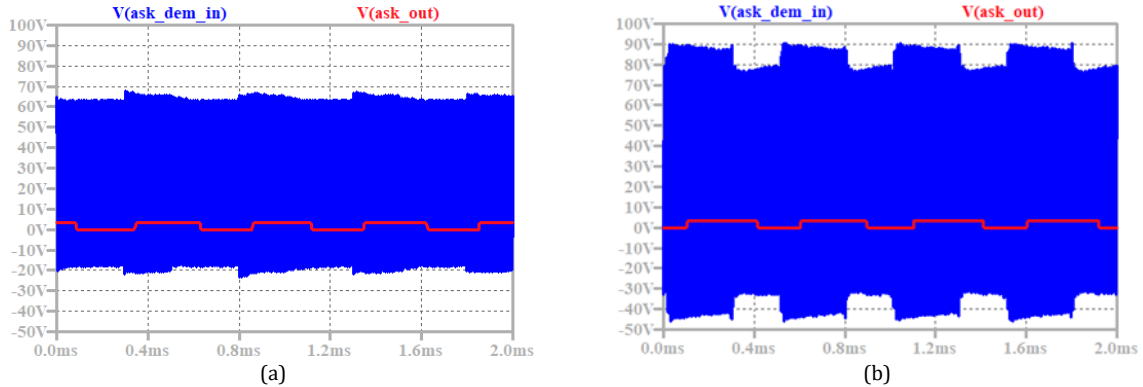


Fig. 42. The ASK Demodulator extracts the data (red) from the modulated Transmitter coil voltage (blue). (a) $P_{outDC}$ = 1.5 W and (b) $P_{outDC}$ = 30 W.

The minimum voltage difference on the Transmitter coil between the modulated and unmodulated states met the requirements specified in [39]. We can see that the output of the demodulator is a bit shifted after the amplitude modulation on the Transmitter coil. However, the phase shift is not an issue.

### 5.1.2 Simulation 2: FSK Preprocessing

The FSK Preprocessing (Fig. 29) was also tested at the minimum and the nominal $P_{outDC}$. Results depicted in Fig. 43 show that in both cases, the FSK Preprocessing successfully converts the Receiver coil voltage waveform to a square wave with levels 0 V and +3.3 V, acceptable by MCU. Again, we can see a phase shift between the output of the FSK preprocessing circuit and the voltage on the coil. However, the phase shift is not an issue as it does not affect the data contained in the signal.

The waveform of the Receiver coil voltage varies with different power levels due to changes in frequency and the strong dependence of circuit impedance on frequency and load, as explained in Section 2.4.2. However, we can see that the different waveform shapes do not affect the output of the FSK Preprocessing circuit.
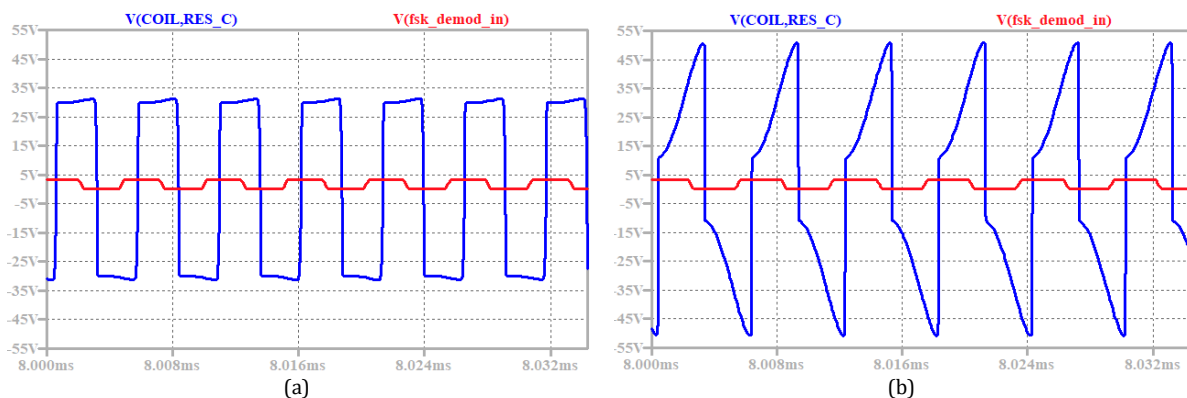


Fig. 43 FSK Pre-processing circuit converts the Receiver coil voltage (blue) to a square wave (red). (a) $P_{oDC}$ = 1.5 W and (b) $P_{oDC}$ = 30 W.

45

## 5.2    Demonstration Scenarios of the Constructed Wireless Charger

In this section, several demonstrational scenarios are presented, capturing the behavior of the realized wireless charger during standard operational conditions labeled as "Use Case" and the behavior of the device under non-standard conditions labeled as "Fault Event".

### 5.2.1    The Measuring Setup

The measurement setup, shown in Fig. 44., was used to capture the waveforms during testing scenarios of the wireless charger integrated into a demonstrational model. The demonstration model consisted of a 3D-printed prototype of the Transmitter casing and a rocket shell cut in the middle to provide a better view of the Receiver. The prototype featured Transmitter and Receiver positioning utilizing permanent magnets, as described in Section 3.4. However, the separating mechanism was not included in this prototype.

It is worth noting that in the verifying phase of the project, the Head Unit nor the Ground Station was not fully developed. Thus, the communication between the Head Unit and the Ground Station was substituted with Debugging UART interface. Both the Transmitter and the Receiver were connected using UART to the PC, as seen in Fig. 44.
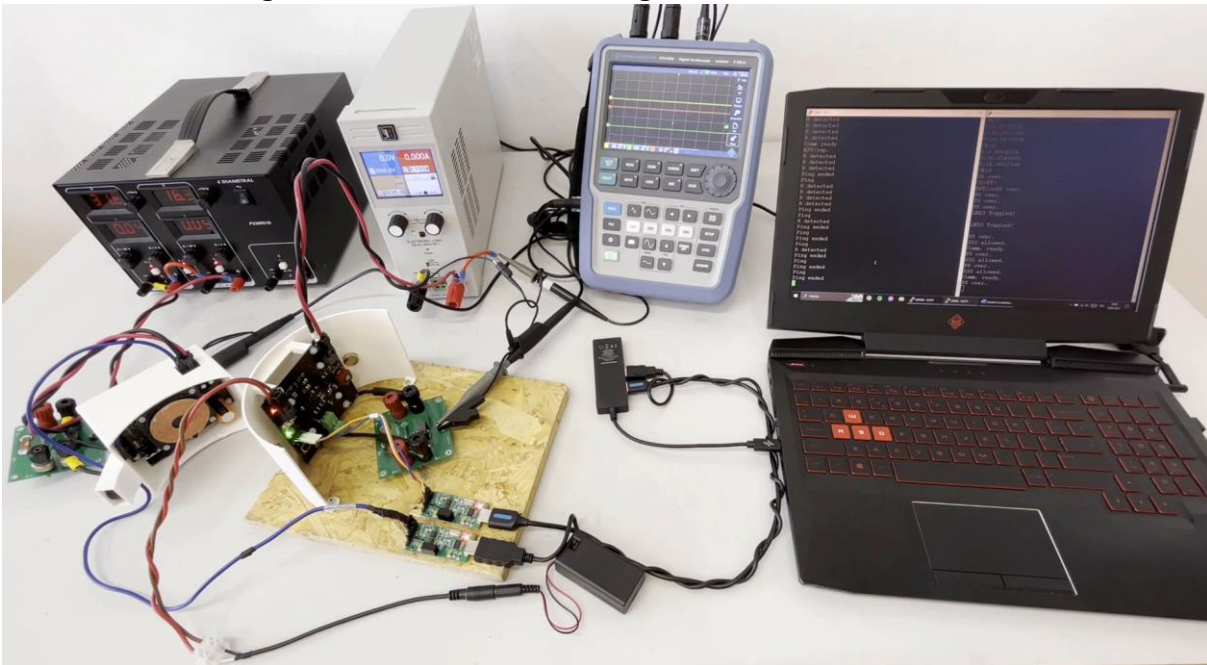


Fig. 44 A measuring setup used to capture the testing scenarios with the Receiver and the Transmitter integrated into a demonstrational model.

The captured waveforms in this section were measured with Rohde & Schwarz RTH1004 oscilloscope. Voltages within these scenarios were measured directly using the RT-ZI10 voltage probes set to 10:1 attenuation. The currents were measured indirectly with the same voltage probes by measuring the voltage on a current shunt. The current shunt parameters are thoroughly described in appendix A2 of [29]. The main purpose of this measurement was to capture the waveform shape, so the voltage values measured on the current shunt were not further recalculated to current values. Nevertheless, suppose we neglect the inductance of the current shunt (the absolute value of the impedance phase of the shunt was less than 0.1 ° for the measured frequency range) for the purpose of these scenarios. In that case, it is possible to consider the value of the current shunts as 30 mΩ within the measured frequency range since both current shunts consist of three 10 mΩ shunts connected in series.

## 5.2.2 Use Case 1: Detecting the Receiver Presence Using Analog Ping

This scenario provides a detailed view of the Transmitter's Coil voltage during the Analog Ping. The Receiver Coil was not in the position with the Transmitter Coil.

### 5.2.2.1 Initial Conditions

The signal from the "Ground Station" to initiate the Analog Ping is sent, and the Transmitter begins to transmit short pulses corresponding to the Analog Ping in regular time intervals of 500 ms.

### 5.2.2.2 Captured Waveform

In Fig. 45, a detailed timeline of a single Analog Ping pulse is displayed, showing the voltage across the Transmitter Coil. The voltage is measured directly with the voltage probe across the Transmitter Coil terminals.

The pulse frequency is set to 170 kHz, which is low enough to distinguish between the state where the Receiver is present or not but not too low to cause any damage to either the Transmitter or Receiver. The pulse duration is set to 93.7 µs, during which the Transmitter measures the input current five times with minimum delay between individual measurements. At the end of the pulse, an average of these values is calculated, and the average value is compared to the threshold value of 100 mA. If the average value is below that, the Transmitter assumes that the Receiver is not present and proceeds to transmit the next pulse after a delay of 500 ms.

If we look at the beginning of the pulse in Fig. 45, the signal's amplitude is unstable and gradually stabilizes until the end of the Analog Ping. However, before the amplitude stabilizes, the MOSFETs within the Inverter are fully closing. At the end of the pulse, when the MOSFETs are closed, the Primary Resonant Circuit discharges through the substrate diodes of the MOSFETs until the resonant circuit is fully discharged, and the voltage across the Transmitter Coil drops to zero.



Fig. 45 The Analog Ping. Blue waveform is the voltage across the Transmitter coil terminals.

## 5.2.3 Use Case 2: Transition from the Initial State to the Communication-only State

This scenario captures the initialization of the communication between the Receiver and the Transmitter from the Initial State.
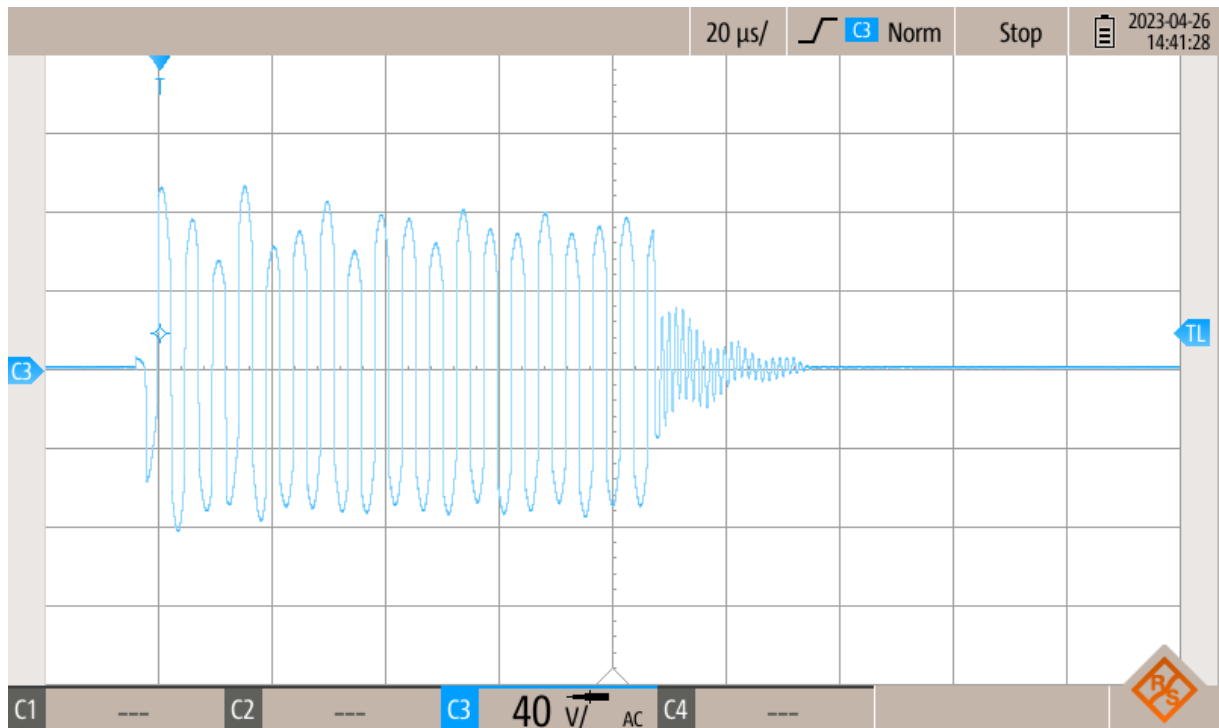
### 5.2.3.1    Initial Conditions

The sequence of events leading up to the captured waveforms can be described as:

1. The Receiver coil is moved away from the position with the Transmitter coil.

2. A command from the "Ground Station" is sent to the Transmitter to initiate transmitting of Analog Ping, locating the Receiver in its surrounding.

3. The command from the "Head Unit" to enable the internal communication is sent to the Receiver, and the Receiver coil is placed in the position with the Transmitter coil.

### 5.2.3.2    Captured Waveforms

In the Fig. 46, we observe the wireless charger transitioning from the Analog Ping State to the Communication-Only State through Digital Ping. Although the Analog Ping pulses are too short to be visible on the timeline, a more detailed scope was provided in the previous scenario in Fig. 45.

The pink waveform in Fig. 46 represents the current through the Primary Resonant Circuit, while the blue waveform displays the output voltage of the ASK Demodulator within the Transmitter. The marks in the form of numbers within the Fig. 46 captures the most important moments and can be described as:

**1:** The first Analog Ping pulse. The Transmitter evaluates that the Receiver is not present, and the device stays in the Analog Ping State. Although the ASK Demodulator output level changes with the Analog Ping pulse, false transitions are successfully handled by the ASK Demodulation software.

**1-2**: Alignment of the coils. The Transmitter is placed in the position where Transmitter and Receiver coils are aligned.

**2:** The second Analog Ping pulse. The second pulse is sent 500 ms after the previous one. Once coils are in position, the Transmitter successfully evaluates the presence of the Receiver. The device is moving to the Digital Ping State.

**3**: The Digital Ping. Here, a longer pulse with a frequency of 210.97 kHz is transmitted, corresponding to the operating point where Ping Impedance is connected on the Receiver side. The voltage on the Ping Impedance is around 30 V. The current amplitude within the Primary Resonant Circuit gradually decreases during the Digital Ping State as the capacitors on the Receiver side charge and the current within the Secondary Resonant Circuit reduces. A stable value is reached at approximately 80 ms after the start of the Digital Ping.

**4:** Reception of the SIG data packet. Once the Receiver detects the Power Signal is stable, it sends a SIG data packet captured by the ASK Demodulator, and the wireless charger successfully moves to the Communication-Only State. This data packet contains a value corresponding to the output voltage to determine the coupling between the coils. Once the transmitter detects an incoming SIG data packet, the Transmitter evaluates that the Receiver is present and moves to the Communication-only State. Communication between the Receiver and the Transmitter is fully restored from this moment. However, if the SIG data packet is not sent within 300 ms of the start of the Digital Ping, the Power Signal is terminated, and the wireless charger reverts to the Analog Ping State.
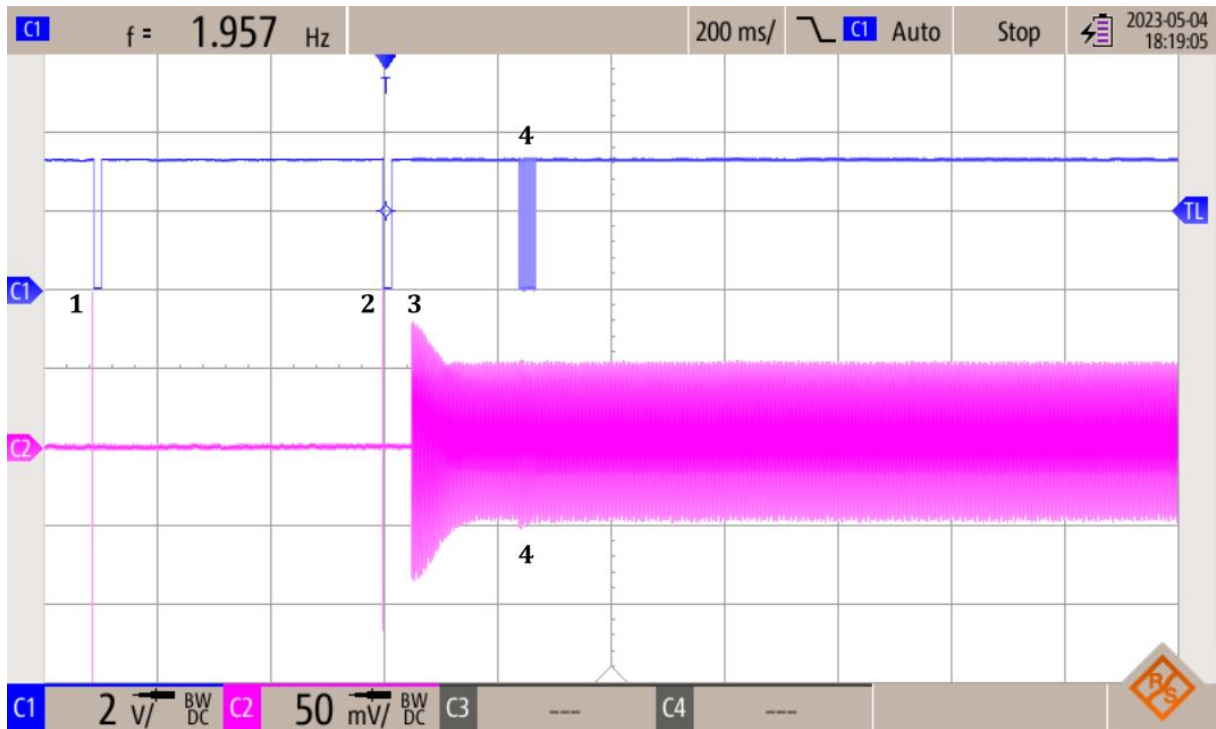
Fig. 46 A Sequence of events leading to successfully restoring the communication between the Receiver and the Transmitter.

## 5.2.4 Use Case 3: Transition to the Power Transfer Phase

This scenario captures the transition from the Communication-only State to the Power Transfer Phase, i.e., connecting the load to the Receiver's output, disconnecting the Ping Impedance, and start of the output voltage regulation. The starting output power level is set to the nominal value of 30 W.

### 5.2.4.1 Initial Conditions

The sequence of events leading up to this scenario can be described as follows:
1. The device is in the Communication-only State, i.e., the output is disconnected, Ping Impedance is connected, and the regulator is disabled.
2. The electronic load resistance is set to 30 Ω, corresponding to the nominal output power of 30 W.
3. "Head Unit" sends a command to start charging the battery.

### 5.2.4.2 Captured Waveforms

Primary and Secondary Resonant Circuit and the output voltage of the Receiver are captured in Fig. 47. The output voltage of the Receiver is the light blue waveform; the current through the Secondary Resonant Circuit is dark blue, and the current through the Primary Resonant Circuit is pink. Both currents are measured on 30 mΩ current shunts, as described at the beginning of this section. The significant moments captured in Fig. 47 are marked with bold numbers and describes the following:

**1**: SRQ/en data packet. The Receiver sends this data packet, enabling the transition to Power Transfer Phase. We can see how the ASK Modulation used to transmit this data packet affects the amplitude of the primary and secondary current. The SRQ/en data packet is basically information for the Transmitter that Control Error (CE) data packets will follow, and the output will be connected to the load.

**2**: Output connected. The output of the Receiver is connected, and the Ping Impedance is disconnected in this order. We can see that the output voltage drops to approximately 20 V, where it settles as the switching frequency is not yet adjusted to the new load.

49

**3**: First CE Data packet. Once the output is connected and the current is stabilized, the Receiver sends the first control error as a CE data packet. The Transmitter processes the data packet in the ASK Demodulator.

**4**: The reaction of the Transmitter to the CE data packet in **3**. The transmitter reacts to the CE data packet after a delay, as described in 4.8. The PID control algorithm is trying to reach the new value of the primary current calculated from the CE data packet value and the primary current measured at the beginning of the algorithm. The Transmitter adjusts the switching frequency in 5 iterations beginning at this moment and following every 4th ms next. The new value of the primary current is reached in the last iteration before the reception of the second CE data packet. Looking at the light blue waveform, the output voltage, we can see how the output voltage begins to return to the desired 30 V. However, more CE data packets must be sent before the output voltage is restored to 30 V.

**5**: The second CE data packet. The Receiver calculates the next control error value, which is now lesser than in the case of **2** as the output voltage deviation is now lesser. The CE is sent, and the Transmitter handles the data packet in the ASK Demodulator.

**6**: The reaction of the Transmitter to the second CE data packet. The Transmitter is again reacting to the last CE data packet, and when the new value is reached, the current is not changing much from this moment on. Similarly, the output voltage now reaches 30 V, and the regulation process is done. From now on, the next CE value is equal to 0 or close to 0, which can be seen at the end of the waveform that the current is not changing anymore.
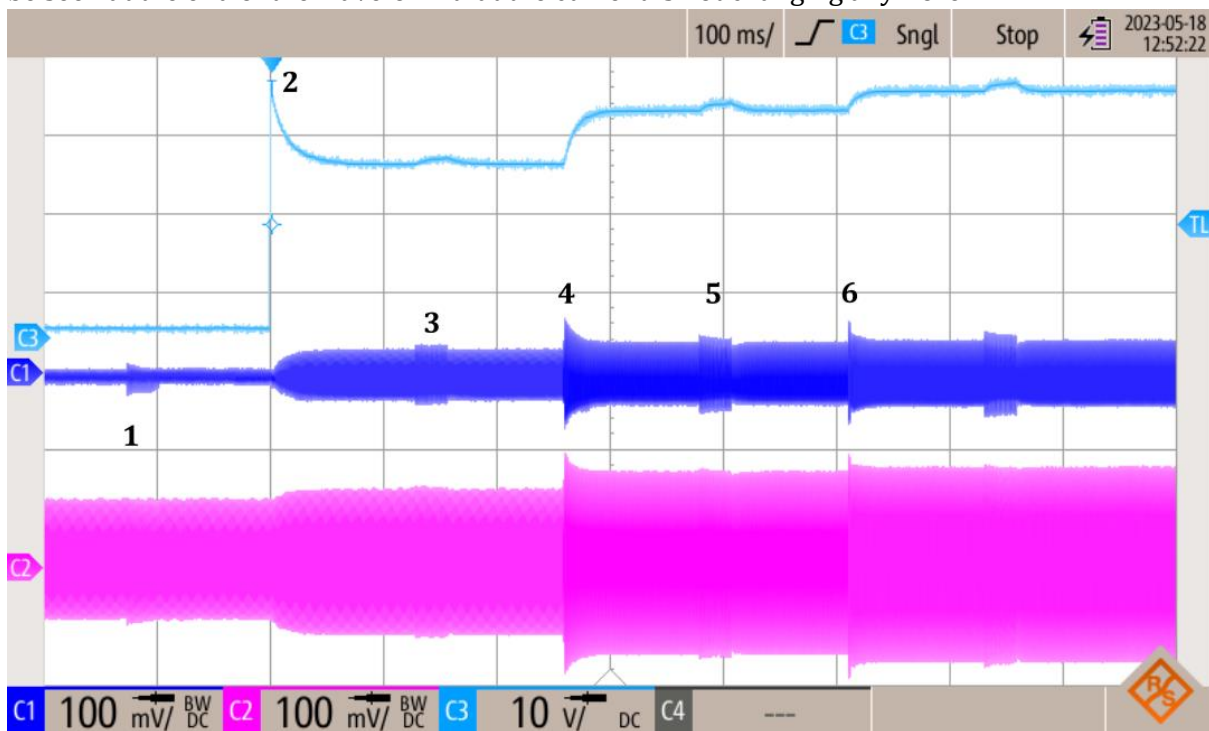


Fig. 47 Transition from the Communication-only State to Power Transfer State (Pout = 30 W). The output voltage is blue, the current measured on a current shunt is pink.

That said, the regulation process is done within less than 600 ms. A similar test (Load Step test) is described in the Qi Standard documentation; their recommendation for stabilizing the regulated variable after performing this sudden load change is 1600 ms. From this point of view, the regulation process is successful [43].

The results were communicated with the CTU SR; from the BMS point of view, it is a good control process. The electronics within the BMS can adjust to the voltage change in this short period, and it is worth noting that this transition is going to happen only in the case when the

almost discharged battery is going to be connected to the Receiver's output so the sudden voltage drop should not be a problem. However, suppose the regulation process took too long, or the voltage was kept low for other reasons. In that case, the current can't flow in the opposite direction since the Output Switch was designed to catch this event (see 4.3).

### 5.2.5 Use Case 4: Communication During the Power Transfer Phase

In this scenario, the output voltage ripple caused by the communication during the power transfer is captured at different output power levels. The communication consists of internal control communication during the power transfer ensuring the output voltage regulation as well as the transfer of application data between the "Head Unit" and the "Ground Station".

The internal communication during the Power Transfer Phase ensures constant output voltage on the Receiver output. It is realized by the Receiver sending the Control Error (CE) packets containing the information about the control error every 250 ms using ASK Modulation. Any application data packets that need to be transferred from the Head Unit to the Ground Station are enqueued in the queue and sent between individual CE packets using ASK Modulation. The delay between the sending of the CE packet and the application data packet is set to 150 ms. This delay ensures that sending those packets will not violate the regulation process which happens 100 ms after reception of the CE packet.

#### 5.2.5.1 Initial Conditions

The wireless charger occurs in the Power Transfer Phase, i.e., the output of the Receiver is connected to the load, and the output voltage is regulated using the PID algorithm as described in 4.8. The communication was tested under three different output power levels:

a. The Minimal Output Power (1,5 W)

b. Half of the Nominal Output Power (15 W)

c. The Maximal Output Power (35 W)

#### 5.2.5.2 Captured Waveforms

In the Fig. 48 (a,b,c) are captured voltage ripples (blue waveform) of the Receiver output and the ASK Demodulator output voltage (pink waveform) for different output power levels. The Oscilloscope probe coupling on channel one was set as AC to capture the ripple in more detail.

Fig. 48 (a) captures the minimal output power level of 1.5 W. The voltage ripple is about 2 V, and compared to the other output levels in Fig. 48 (b,c), it is the worst case in the case of voltage ripple. The voltage ripple is caused by connecting the additional load in form of ASK Modulation capacitors (C11 and C12 in Fig. 29), causing the operational state change. However, the change of the load is fast, and the Transmitter cannot react to this change as the regulation process begins 100 ms after receiving this packet. Although the voltage ripple of 2 V is greater than was initially assumed, as described further in B.6, this value was accepted as it can be further filtered in the input filter of the BMS, which was not yet designed in this phase of the project. Additionally, the voltage ripple timeline is long enough for the BMS to react to these changes if no sufficient filter is used.
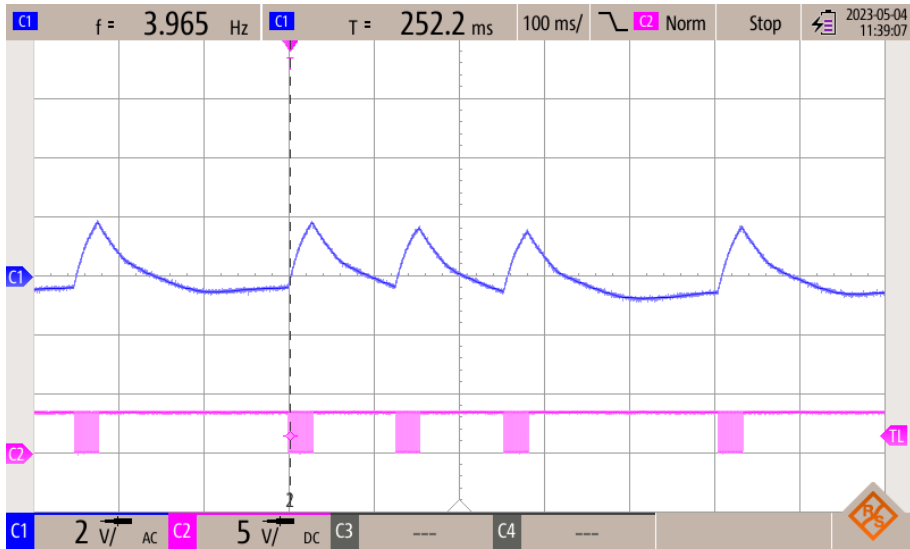
(a)
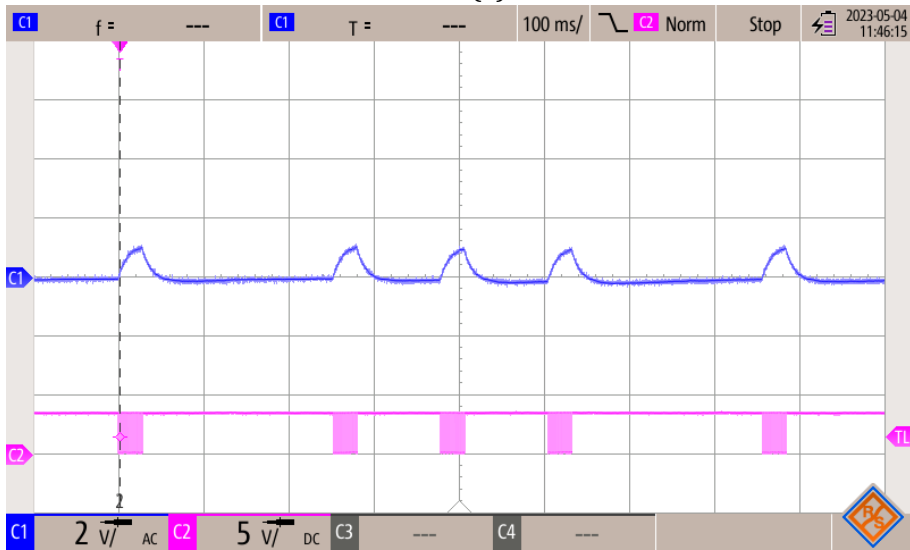


(b)
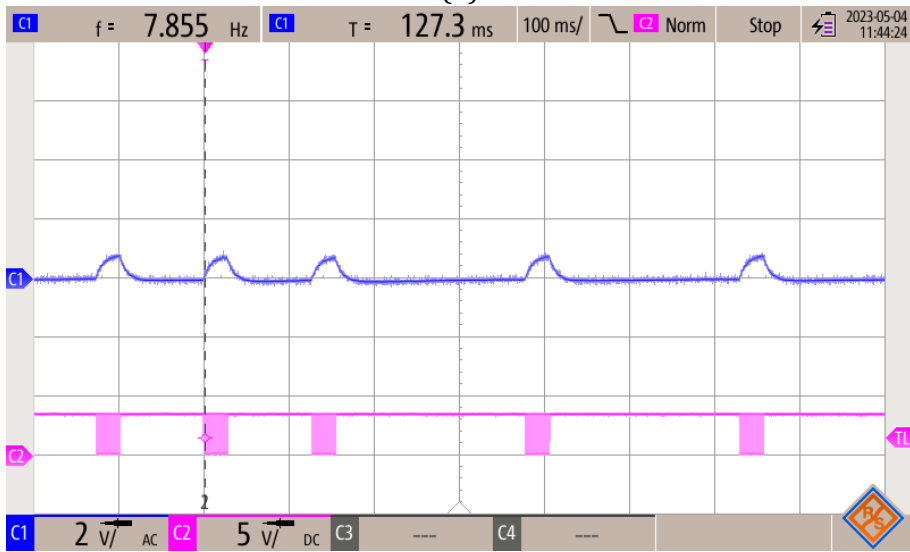


(c)

Fig. 48 Communication during Power Transfer Phase for (a) minimal output power level, (b) nominal output power level, (c) maximal output power level.

## 5.2.6    Fault Event 1: Receiver Removal During the Power Transfer Phase

This scenario aims to test how the wireless charger responds to the Receiver Coil being suddenly removed from its aligned position with the Transmitter Coil. While this is not a standard event within the intended operation of the wireless charger, as the Receiver should first send a closing EPT (End of Power Transfer) data packet before removing the Receiver Coil, this event should still be considered a possible error event and as such, should be appropriately handled.

### 5.2.6.1    Initial Conditions

The wireless charger is in the Power Transfer Phase, and the output power level is set to the nominal output power of 30 W. The coils are properly aligned, and the output voltage is regulated at a constant value of 30 V by sending the CE packets.

### 5.2.6.2    Captured Waveforms

In Fig. 49 are captured the output voltage of the Receiver (blue) and the current through the Primary Resonant Circuit (pink). The significant moments are marked with bold numbers and describe the following:

**1**: CE data packet sent. We can see that one last CE packet is sent before removing the Receiver Coil, causing the voltage to ripple on the Receiver output.

**2**: Removal of the Receiver from its position. The Receiver Coil is removed, causing the voltage on the Receiver output to decrease and the amplitude of the current through the Primary Resonant Circuit to decrease as well.

**3**: The Receiver output disconnection. Now the Receiver disconnects the output and connects the Ping Impedance instead as it detects that the output voltage dropped below the minimum threshold value set to 20 V. However, the measuring loop is made once every 25 ms, as described in 4.7. That is why the actual output voltage is less than 20 V.

**4**: Termination of the Power Signal. The Transmitter detects the removal of the Receiver from its position by not receiving any CE data packet. It removes the Power Signal at 1 500 ms after the reception of the last CE data packet, i.e., the Inverter is shut down.

The Ground Station and the Head Unit are informed about this fault event with a proper error message, and the wireless charger enters the Fault State. Before moving to the Analog Ping State again, the fault must be resolved with the supervising unit as described in 3.2.

Fig. 49 Output voltage of the Receiver (blue) and the current through the Primary Resonant Circuit (pink) during the removal of the Receiver Coil.

## 5.2.7 Fault Event 2: Sudden Disconnection of Load during Power Transfer

This scenario captures the behavior of the wireless charger when the load is suddenly disconnected during the power transfer. This scenario is intended to simulate a sudden and unexpected change in the load caused by a fault in the BMS within the rocket's battery pack or a complete disconnection of the load.

### 5.2.7.1 Initial Conditions

The wireless charger is in the Power Transfer Phase, and the output power level is set to nominal output power of 30 W, which corresponds to load $R_L$ = 30 Ω.

### 5.2.7.2 Captured Waveform

In Fig. 50 are captured the output voltage of the Receiver (blue) and the current through the Primary Resonant Circuit (pink).

The output voltage is kept constant at a value of 30 V during Power Transfer when a step change in load happens, as depicted in the Fig. 50. The disconnection of the load is simulated by step changing the resistance value of the electronic load from a value of $R_L$ = 30 Ω to a maximum possible value of the electronic load $R_L$ = 2044 Ω. This value corresponds to DC output power of $P_{outDC}$ = 0.44 W which is below the minimum output power $P_{MIN}$ = 1.5 W. The wireless charger is not intended to operate at such low power levels as declared in 1.3.

The critical events within the scenario are marked in the Fig. 50. with bold numbers and mean following:

**1**: Last CE data packet. CE data packet is sent before the load is changed.

**2**: Load change. The output voltage suddenly increases as the load is changed from the value of $R_L$ = 30 Ω to $R_L$ = 2044 Ω. As the $R_L$ rises, the output voltage rises as well due to (2-21). The output voltage cannot change immediately due to the capacitors within the output filter. The effect of increased value $R_L$ on the primary side can be explained with the reflected impedance model in 2.4.2. As the $R_L$ increases, the reflected impedance real and imaginary parts (2-22) changes resulting in decrease of its absolute value. Hence, the input current of the Transmitter decreases.

54

It is worth noting that although the change of the $R_L$ is reflected on the primary, since the input impedance (2-18) consist of sum of both the reflected impedance and the impedance of the primary, which is not affected by the secondary, the absolute value of input impedance is not much changing from a certain value of $R_L$ (within this frequency range) and the input current thus does not decrease below a value which corresponds to the case where the secondary is not present at all, and the input is loaded only with the primary resonant circuit.

**3:** Ping Impedance connected. When the output voltage reaches the threshold value of 35 V, evaluated as overvoltage by the Receiver MCU, the Receiver connects the Ping Impedance and disconnects the output in this sequence. The amplitude of the input current is not much changed at this moment and further on, as discussed in the previous paragraph.

**4:** Output disconnected. The output is disconnected, and only the Ping Impedance is now connected, resolving in output voltage drop to zero.

**5:** Power Signal shut down. After 1 500 ms from the last received CE data packet, the Transmitter terminates the power transfer by shutting down the Power Signal.

The wireless charger then moves to the Fault State and notifies the surroundings about the fault that happened. The wireless charger can restore communication and power transfer once the fault is resolved.



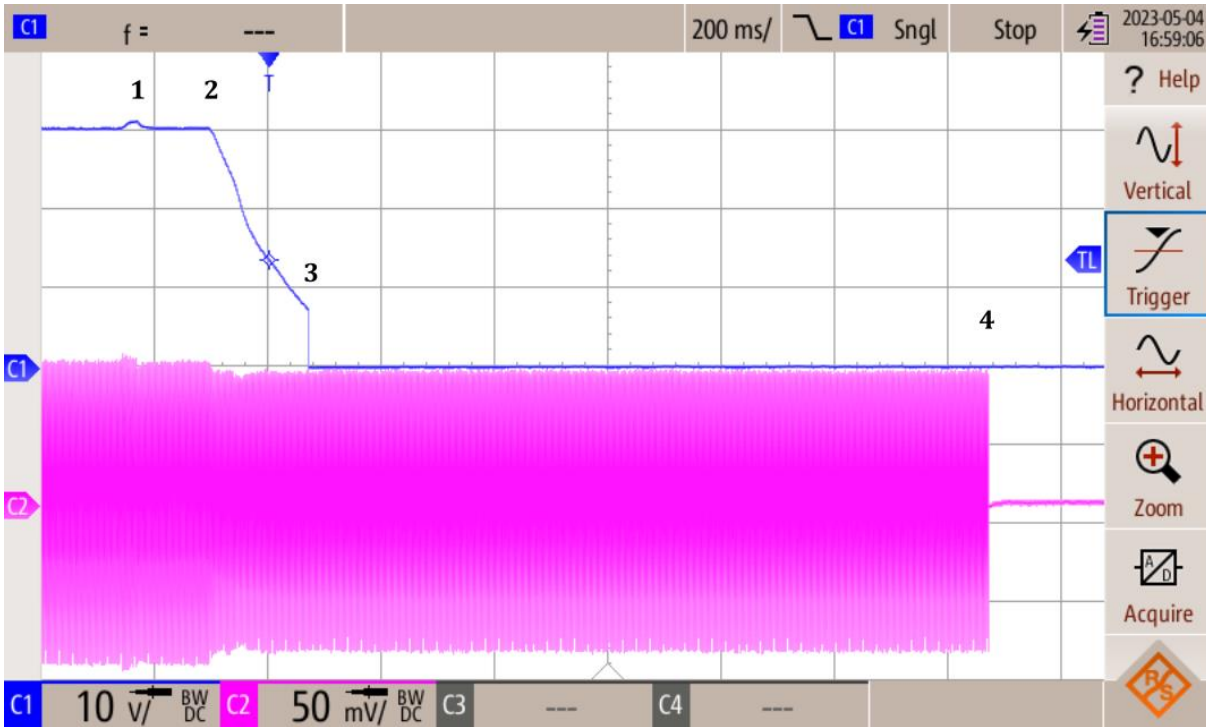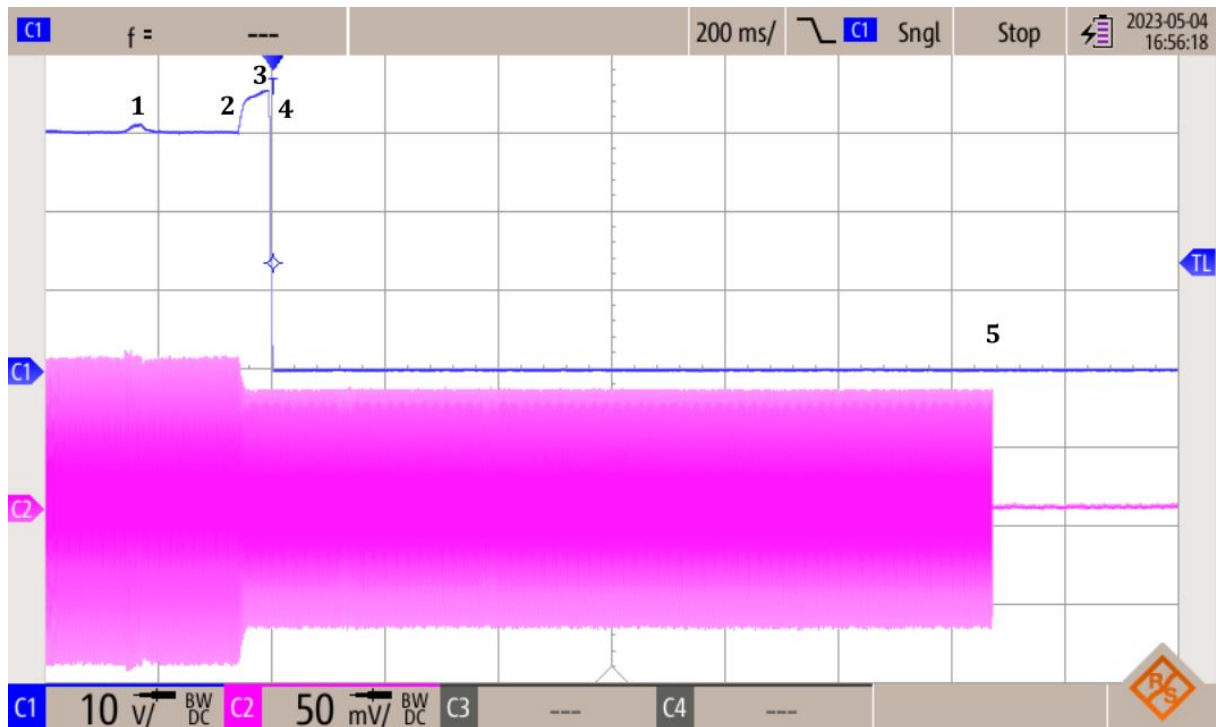Fig. 50 Output voltage of the Receiver (blue) and the current through the Primary Resonant Circuit (pink) during the load disconnection.

## 5.2.8 Fault Event 3: Reaction to Overcurrent

This scenario captures the transmitter's response to an overcurrent caused by a sudden load change. This scenario simulates a fault on the BMS, such as a short circuit or a power demand greater than agreed upon.

### 5.2.8.1 The Initial Conditions

The Wireless Charger is in Power Transfer Phase, regulating the output voltage to a constant value of 30 V. The output power level is set to the nominal value of 30 W, which corresponds to load $R_L$ = 30 Ω. The electronic load resistance is then changed in a step to $R_L$ = 10 Ω.

## 5.2.8.2 Captured Waveforms

For this scenario, both currents in the Primary and Secondary Resonant Circuit were measured, as well as the output voltage of the Receiver. In Fig. 51, the output voltage of the Receiver is the light blue waveform; the current through the Secondary Resonant Circuit is dark blue, and the current through the Primary Resonant Circuit is pink. Both currents are measured on 30 m$\Omega$ current shunts, as described at the beginning of this section. The significant events are marked with bold numbers and can be described as:

**1:** The last control error data packet. Here we can see that the current amplitude change in the secondary is more significant than in the primary.

**2**: The load change. The load resistance is changed to $R_L$ = 10 $\Omega$. Both primary and secondary currents are rapidly increasing, but they are stopped as the comparator detects that the input current rises above the threshold value. The comparator triggers an interrupt where a shutdown signal is sent to the gate drivers, resulting in the Inverter terminating the Power Signal. At the same time, the Transmitter moves to the Fault State and informs the "Ground Station" about the error event.

**2-3**: Discharging of capacitors. In this period, no power is transmitted across the air gap, and the output voltage of the Receiver decreases as the Output Filter capacitors are discharged.

**3**: Disconnection of output. The Receiver detects that the Power Signal is shut down by detecting a voltage drop. The Ping Impedance is connected, the output is disconnected in this order, and the Receiver moves to the Fault State. Simultaneously, the "Head Unit" is notified about the error state.



Fig. 51 Reaction of Transmitter to overcurrent. The light blue waveform is the output voltage of the Receiver, the pink waveform is the voltage on a current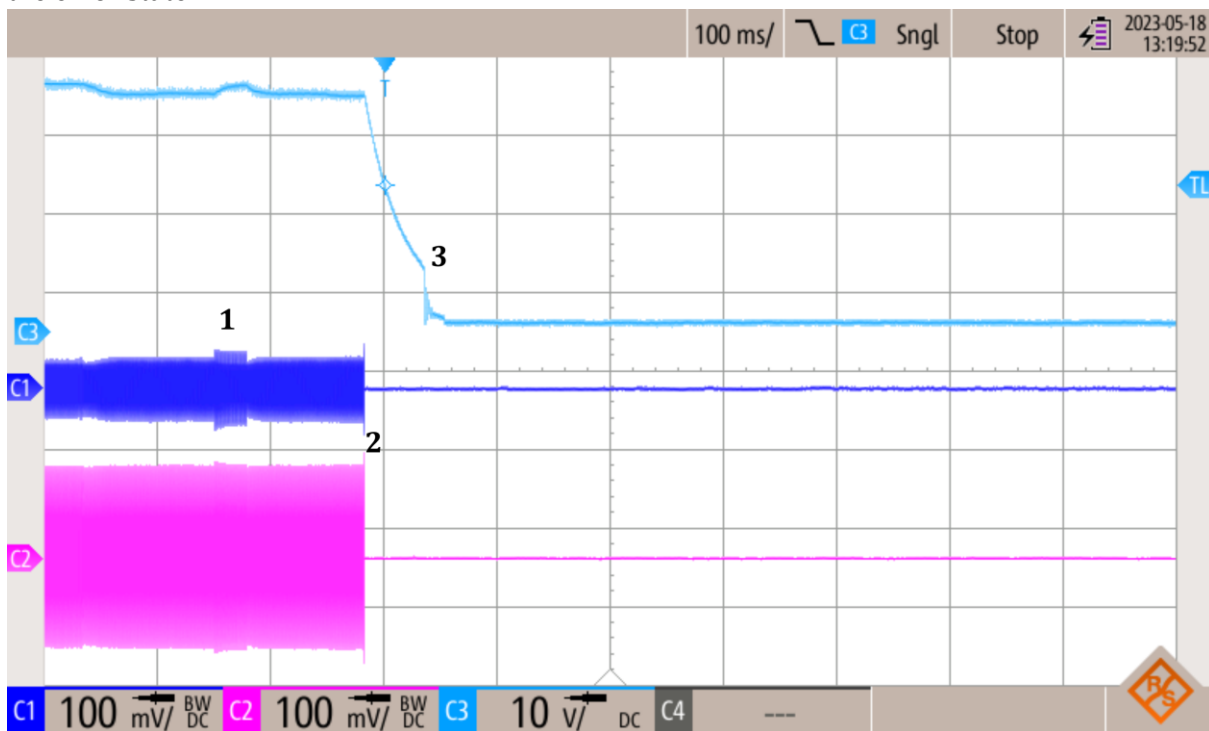 shunt measuring the primary current, and the dark blue waveform is the voltage on the current shunt measuring the secondary current.

## 5.3 Verifying the Power Transfer across the Whole Operational Range

In this section, the DC-DC efficiency $\eta_{DC-DC}$ of the realized wireless charger is measured across the whole operational range, and the results are compared to the results from simulations which were obtained using the LTspice model with parameters from the optimization method as described in 5.1. The measured values were measured using the calibrated built-in Current & Voltage Measuring Circuits in the Transmitter and the Receiver, as discussed in 4.7.

### 5.3.1 Measuring & Simulation Setup

The operational range was defined by the output power with minimal, nominal, and maximal output power (as defined in 1.3) and another 13 operating points linearly distributed across the minimal and maximal output power.

The measured values were obtained as follows:

1. The corresponding $R_L$ was set on electronic load for the desired output power.
2. The PID regulator adjusted the switching frequency, so the output voltage was 30 V with a tolerance of < 0.01 V.
3. Then, the switching frequency was adjusted manually to reach the output voltage of 30 V with a tolerance of < 0.01 V.
4. Input and Output power was measured, and the values were sent to the PC via UART.
5. The $\eta_{DC-DC}$ can be then calculated using the formula in (2-33).

The simulated values were obtained from the simulation where resistance. $R_L$ was set, and the switching frequency had to be adjusted manually to reach the output voltage of 30 V with a tolerance of < 0.01 V.

### 5.3.2 Measured & Simulated Characteristics

If we compare the measured DC-DC efficiency $\eta_{DC-DC}$ of the real device to the simulation results from the optimization method, as depicted in Fig. 52, for nominal and maximal output power, the efficiency of the real device is approximately 10 % less than the simulation results. The difference between the simulation and the real values is greater for lower power levels, and for the minimal output power, the difference in efficiency is approximately 50 %. Let's look at these curves' shapes and observe the curve from right to left (from greater to lower output power). We can see that the point where the curve changes from a shallower slope to a steeper slope and the efficiency starts to decrease rapidly is, in the case of the measured values, around 10 W. However, this point in the case of the simulated values is located at lower output power levels, at approximately 5 W. The simulated chart is thus a bit shifted to the left, which means that the simulated device could operate even at lower output power levels than the real one with greater efficiency.
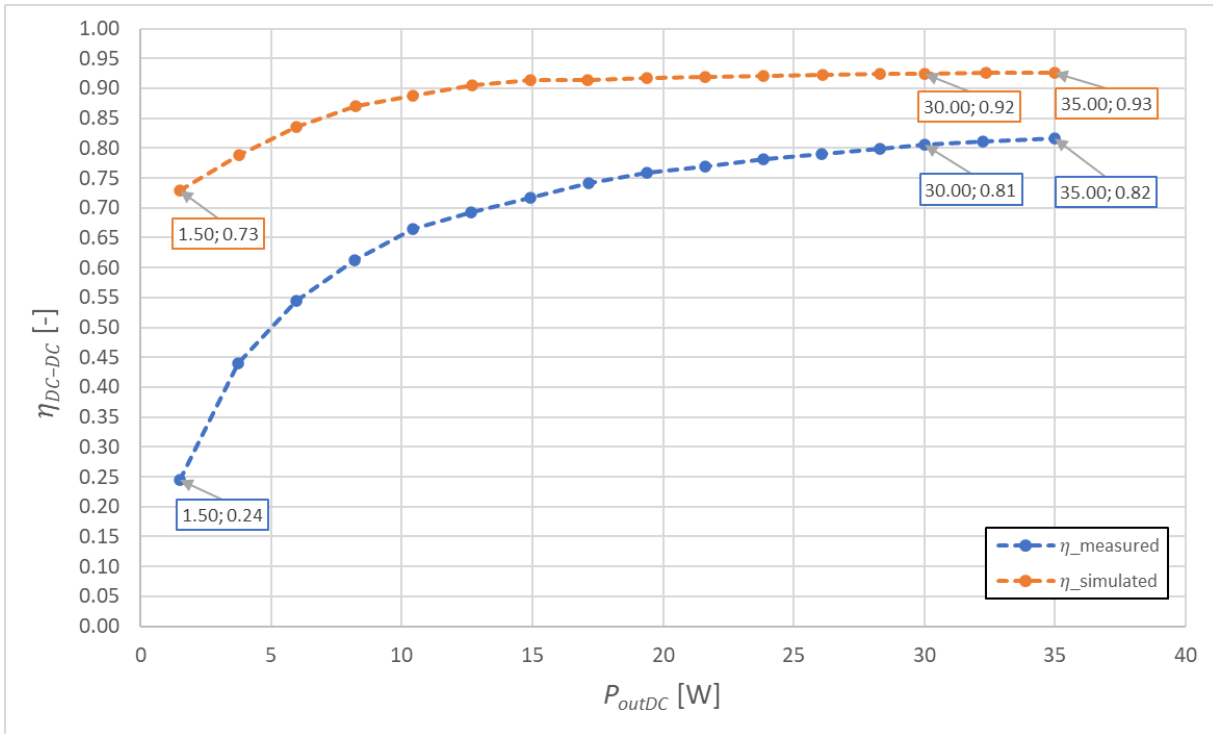
Fig. 52 DC-DC efficiency across the operational range of the realized wireless charger (blue) and the comparison with simulation results (orange). The minimal, nominal, and maximal output power operating points in the form of ($P_{out}$; $\eta_{DC-DC}$) are displayed in boxes.

Each measured and simulated point of the operational characteristics is depicted in the power-frequency characteristics in Fig. 53 which role was described in 2.5.2. If we compare the measured and the simulated values, we see that the simulated frequencies are always a bit larger than the measured frequencies for given output power.
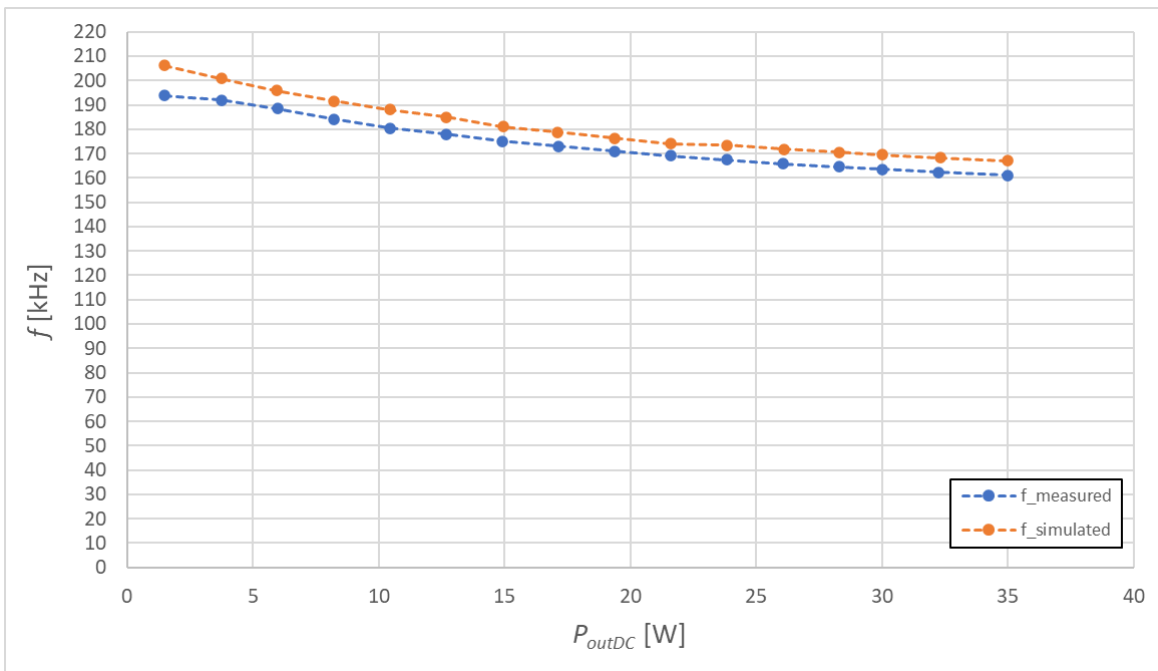


Fig. 53 Comparison of real (blue) and simulated (orange) operating frequencies for the power-frequency characteristics where the output voltage is 30 V.

### 5.3.3      Achieved Results of the Constructed Wireless Charger

Overall, the DC-DC efficiency of the wireless charger is greater than 70 % of output power levels greater than 15 W, corresponding to half of the nominal output power level. For the nominal and maximal output power, the efficiency is 81 and 82 %, respectively. The Qi standard sets the recommended minimum efficiency for devices built on their standard different for different architectures of the Receiver. However, the minimum efficiency recommendation from the Qi standard ranges from 55 to 75 % for maximal output power level. From this point of view, the achieved efficiency is a success since the achieved efficiency is greater than the strictest recommended efficiency value [43].

The low efficiency at the minimum output power of the device is not a significant problem since the wireless charger will operate at this power level only in the case where the battery is or almost is fully charged, and the charge status of the battery is only maintained. Another operation state of the battery on the minimal output power corresponds to the Communication-only state (see 3.2.4), where only Ping Impedance is connected, and no power is transferred to the battery.

The overall losses within the realized IPT System represent 4.75 W for the minimal output power, 7 W for the nominal output power, and 8.2 W for the maximal output power, which is dissipated in the form of heat. During the testing of the device, the heating was not a problem in either the Transmitter or the Receiver. As was observed, most of the heat was produced by the coils. However, the coils are distant from the Receiver and the Transmitter PCBs with nylon spacers 15 and 20 mm long, respectively. The heat is thus dissipated easily to surroundings and is not a threat to other components within the PCBs.

### 5.3.4      Comparison of Measured and Simulated Results

Overall, the differences between the simulated values using the parameters from the optimization method and the measured values of the real device are not negligible. The differences are caused by the overall simplifications within the simulation model and inaccuracies within the optimization method. The most significant differences between the values from the optimization method and the real values are as follows. The difference between the real secondary inductance $L_s$ and the calculated is greater than 3.65 % which may cause the shift of the efficiency-power characteristics as discussed in 5.3.2. Secondly, the ESR of the coils within the optimization is constant for all frequencies. However, as seen in Tab. 4-2, the ESR of the real coils significantly grows with increasing frequency. Lastly, neither the optimization method nor the LTspice model considers the heating of the components, which causes additional losses in the real system.

# CONCLUSION

This thesis presented the design and construction of a wireless charger for a rocket developed by CTU Space Research. The charger maintains a constant output voltage of 30 V for an output power range from 1.5 to 35 W. The nominal output power is 30 W. The BMS processes the output voltage within the rocket to charge the rocket's battery pack until liftoff. Simultaneously, the wireless charger enables transferring data between the rocket's main MCU and the ground station. It replaces the cable connection requiring a flip-up cover integrated into the rocket's shell, and thus it enables a solid rocket shell without any openings.

The charger architecture is based on a full-bridge inverter, of which the switching frequency is regulated to maintain constant output voltage, two circular coupling coils with series compensation, and a diode rectifier. The control strategy and communication across the air gap are based on Qi Standard, adapted for this specific application. The main circuit parameters, such as the self- and mutual inductances or the input DC voltage, were obtained by a novel optimization method developed simultaneously with this project.

The design was implemented on a real device, and the wireless charger functionality was verified throughout the demonstration of the device operation under standard and nonstandard conditions. The wireless charger can successfully operate in these conditions without causing harm to itself or the surroundings.

The power transfer efficiency was measured across the whole operational range and compared to the results from the optimization method. The overall DC-DC efficiency is 82 % for the maximum, 81 % for the nominal output power, and above 70 % for the output power greater than 15 W.

In conclusion, the construction of the wireless charger for the CTU Space Research was successful, fulfilling all requirements except the bi-directional communication. While ASK modulation and demodulation were successfully implemented, FSK demodulation is still under development. The completion of the project is planned for October 2023, before the EUROTEC competition in which the rocket will participate.

This project demonstrates the potential of wireless power transfer in aerospace applications, offering efficient and convenient charging without the need for physical connections. The benefits of wireless charging, such as improved aerodynamics, better structural integrity, reduced maintenance, and battery size, and increased overall safety, make it a promising technology for future applications.

Furthermore, this thesis provided valuable data for further enhancements to the optimization procedure used to maximize the overall DC-DC efficiency of IPT systems.

# REFERENCES

[1]    P. Machura and Q. Li, "A Critical Review on Wireless Charging for Electric Vehicles 1."

[2]    Z. Zhang, H. Pang, A. Georgiadis, and C. Cecati, "Wireless Power Transfer—An Overview," *IEEE Transactions on Industrial Electronics*, vol. 66, no. 2, pp. 1044–1058, Feb. 2019, doi: 10.1109/TIE.2018.2835378.

[3]    M. Košík, A. D. Scher, A. Pešek, and P. Skarolek, "A Study of a Novel Optimization Method for IPT Systems with Variable Frequency," San Diego, USA: Wireless Power Technology Conference and Expo, Jun. 2023.

[4]    Portuguese Space Agency, "Europen Rocketry Challenge, Rules & Requirements," Jun. 2023. Accessed: May 21, 2023. [Online]. Available: https://euroc.pt/rules-and-requirements/

[5]    T. K. Sarkar, R. J. Mailloux, A. A. Oliner, M. Salazar, P. Dipak, and L. Sengupta, *History of Wireless*. New Jersey: John Wiley & Sons, Inc., 2006.

[6]    N. Shinohara, *Wireless Power Transfer via Radiowaves*. Hoboken, NJ, USA: John Wiley & Sons, Inc., 2013. doi: 10.1002/9781118863008.

[7]    IEEE Wireless Power Technologies, "WPT History," *https://wirelesspower.ieee.org/wpt-history/*, May 05, 2023.

[8]    N. Tesla, "Experiments with Alternate Currents of Very High Frequency and their Application to Methods of Artificial Illumination," *Transactions of the American Institute of Electrical Engineers*, vol. VIII, no. 1, pp. 266–319, Jan. 1891, doi: 10.1109/T-AIEE.1891.5570149.

[9]    H. Feng, R. Tavakoli, O. C. Onar, and Z. Pantic, "Advances in High-Power Wireless Charging Systems: Overview and Design Considerations," *IEEE Transactions on Transportation Electrification*, vol. 6, no. 3, pp. 886–919, Sep. 2020, doi: 10.1109/TTE.2020.3012543.

[10]   L. W. Y. Liu and S. N. Thành, "Towards the Feasibility of Long Range Wireless Power Transfer over an Ocean Surface," *Applied Sciences*, vol. 12, no. 17, p. 8751, Aug. 2022, doi: 10.3390/app12178751.

[11]   EFYMAG, "All About Transferring Power Wirelessly," *Electronics For You*, Aug. 2003.

[12]   A. Karalis, J. D. Joannopoulos, and M. Soljačić, "Efficient wireless non-radiative mid-range energy transfer," *Ann Phys (N Y)*, vol. 323, no. 1, pp. 34–48, Jan. 2008, doi: 10.1016/j.aop.2007.04.017.

[13]   A. Q. Cai and L. Siek, "A 2-kW, 95% Efficiency Inductive Power Transfer System Using Gallium Nitride Gate Injection Transistors," *IEEE J Emerg Sel Top Power Electron*, vol. 5, no. 1, pp. 458–468, Mar. 2017, doi: 10.1109/JESTPE.2016.2632743.

[14]   A. Foote and O. C. Onar, "A review of high-power wireless power transfer," in *2017 IEEE Transportation Electrification Conference and Expo (ITEC)*, IEEE, Jun. 2017, pp. 234–240. doi: 10.1109/ITEC.2017.7993277.

[15]   A. Kurs, A. Karalis, R. Moffatt, J. D. Joannopoulos, P. Fisher, and M. Soljačić, "Wireless Power Transfer via Strongly Coupled Magnetic Resonances," *Science (1979)*, vol. 317, no. 5834, pp. 83–86, 2007, doi: 10.1126/science.1143254.

[16]   A. Abdolkhani, "Fundamentals of Inductively Coupled Wireless Power Transfer Systems," in *Wireless Power Transfer - Fundamentals and Technologies*, InTech, 2016. doi: 10.5772/63013.

[17]   P. R. Eberhard Waffenschmidt, "KNOWLEDGE BASE," *Wireless Power Consortium*, 2023. https://www.wirelesspowerconsortium.com/knowledge-base/magnetic-induction-technology/how-it-works/coupling-factor.html (accessed May 06, 2023).

[18]   M. Frivaldsky, V. Jaros, P. Spanik, and M. Pavelek, "Control system proposal for detection of optimal operational point of series–series compensated wireless power transfer system," *Electrical Engineering*, vol. 102, no. 3, pp. 1423–1432, Sep. 2020, doi: 10.1007/s00202-020-00963-2.

[19] P. R. Eberhard Waffenschmidt, "Qi Quality Factor," *https://www.wirelesspowerconsortium.com/knowledge-base/magnetic-induction-technology/how-it-works/quality-factor.html*, 2023.

[20] M. Budhia, G. A. Covic, J. T. Boys, and C.-Y. Huang, "Development and evaluation of single sided flux couplers for contactless electric vehicle charging," in *2011 IEEE Energy Conversion Congress and Exposition*, IEEE, Sep. 2011, pp. 614–621. doi: 10.1109/ECCE.2011.6063826.

[21] W. Andrä and R. Hergt, "Magnets: Biomedical Applications," in *Encyclopedia of Materials: Science and Technology*, Elsevier, 2001, pp. 5107–5110. doi: 10.1016/B0-08-043152-6/00887-1.

[22] K. Chen, J. Pan, Y. Yang, and K. W. E. Cheng, "Optimization of ferrites structure by using a new core-less design algorithm for electric vehicle wireless power transfer," *Energies (Basel)*, vol. 14, no. 9, May 2021, doi: 10.3390/en14092590.

[23] T. Campi, S. Cruciani, and M. Feliziani, "Magnetic shielding of wireless power transfer systems," in *2014 International Symposium on Electromagnetic Compatibility, Tokyo*, 2014, pp. 422–425.

[24] S. Varikkottil, F. D. J. Lionel, M. K. Srinivasan, S. Williamson, R. Kannan, and L. I. Izhar, "Role of Power Converters in Inductive Power Transfer System for Public Transport—A Comprehensive Review," *Symmetry (Basel)*, vol. 14, no. 3, Mar. 2022, doi: 10.3390/sym14030508.

[25] Siqi Li and C. C. Mi, "Wireless Power Transfer for Electric Vehicle Applications," *IEEE J Emerg Sel Top Power Electron*, vol. 3, no. 1, pp. 4–17, Mar. 2015, doi: 10.1109/JESTPE.2014.2319453.

[26] C.-S. Wang, G. A. Covic, and O. H. Stielau, "Power Transfer Capability and Bifurcation Phenomena of Loosely Coupled Inductive Power Transfer Systems," *IEEE Transactions on Industrial Electronics*, vol. 51, no. 1, pp. 148–157, Feb. 2004, doi: 10.1109/TIE.2003.822038.

[27] Michal Košík, Aaron D. Scher, and Jiří Lettl, "General Parameter Model of Bifurcation and Frequency Splitting in Series-Series Compensated Inductive Power Transfer," *IEEE Access*, 2017.

[28] Michal Košík, "BIFURCATION ANALYSIS AND CONTROL METHODS FOR INDUCTIVELY COUPLED POWER TRANSFER Doctoral Thesis," 2021.

[29] L. Yang, X. Li, S. Liu, Z. Xu, C. Cai, and P. Guo, "Analysis and Design of Three-Coil Structure WPT System with Constant Output Current and Voltage for Battery Charging Applications," *IEEE Access*, vol. 7, pp. 87334–87344, 2019, doi: 10.1109/ACCESS.2019.2925388.

[30] R. Bosshard, U. Badstubner, J. W. Kolar, and I. Stevanovic, "Comparative evaluation of control methods for Inductive Power Transfer," in *2012 International Conference on Renewable Energy Research and Applications (ICRERA)*, IEEE, Nov. 2012, pp. 1–6. doi: 10.1109/ICRERA.2012.6477400.

[31] M. Košík, P. Skarolek, A. D. Scher, and A. Pešek, "A Study of a Novel Optimization Method for IPT Systems with Variable Frequency," 2023.

[32] M. Košík, A. D. Scher, and J. Lettl, "Novel method of coupling coefficient estimation based on the bifurcation phenomena in inductive power transfer," *Electronics (Switzerland)*, vol. 10, no. 20, Oct. 2021, doi: 10.3390/electronics10202548.

[33] Wireless Power Consortium, "About Qi," *https://www.wirelesspowerconsortium.com/qi/*, 2023.

[34] Qi Wireless Charging, "All Phones With Wireless Charging – Qi Enabled Phones & Compatible Devices," *https://qi-wireless-charging.net/qi-enabled-phones/*, 2023.

[35] Wireless Power Consortium, "Qi Specification Glossary Definitions, Acronyms, and Symbols," 2021.

[36]     WPC, "Qi Specification, Communications Protocol," 2021.
[37]     WPC, "Qi Specification, Communications Physical Layer," 2021.
[38]     Wireless Power Consortium, "Qi Specification, Power Receiver Design Examples," 2021.
[39]     The Wireless Power Consortium, "Qi Specification, Communications Physical Layer," Version 1.3, 2021
[40]     The Wireless Power Consortium, "Qi Specification, Communications Protocol," Version 1.3, 2021
[41]     The Wireless Power Consortium, "Qi Specification, Power Delivery," Version 1.3, 2021
[42]     STMicroelectronics, "RM0364 Reference Manual STM32F334xx advanced Arm-based 32-bit MCUs," Jun. 2020.
[43]     WPC, "Qi Specification, Power Delivery," 2021.
[44]     Würth Elektronik eiSos GmbH & Co. KG, "760308101141 Datasheet," 2017. Accessed: May 08, 2023. [Online]. Available:
         https://www.we-online.com/components/products/datasheet/760308101141.pdf
[45]     G. Xiang, "Demodulating Communication Signals of Qi-Compliant Low-Power Wireless Charger Using MC56F8006 DSC," *Freescale Semiconductor*, Mar. 2013.
[46]     WPC, "Qi Specification Power Transmitter Reference Designs," 2021.

# APPENDIX A NOMENCLATURE

## General Symbols

| | |
|---|---|
| $\hat{x}$ | phasor |
| $x^*$ | the complex conjugate of the phasor |
| $x$ | instantaneous scalar quantity |

## Symbols and Variables

| | |
|---|---|
| $\hat{I}_{in}$ | input current (A) |
| $\hat{I}_{out}$ | output current (A) |
| $\hat{V}_{in}$ | input voltage (V) |
| $\hat{V}_{out}$ | output voltage (V) |
| $\hat{Z}_p$ | the total impedance of the primary (Ω) |
| $\hat{Z}_r$ | reflected impedance (Ω) |
| $\hat{Z}_s$ | the total impedance of the secondary (Ω) |
| $C_p$ | the capacity of the primary resonant capacitor (F) |
| $C_s$ | the capacity of the secondary resonant capacitor (F) |
| $I_F$ | diode forward current (A) |
| $I_{inDC}$ | input DC current (A) |
| $I_{off}$ | current through MOSFET when turned off (A) |
| $I_{outDC}$ | output DC current (A) |
| $K_d$ | the derivative constant of the PID regulator within the current control loop (A) |
| $K_i$ | the integral constant of the PID regulator within the current control loop (A) |
| $K_p$ | the proportional constant of the PID regulator within the current control loop (A) |
| $L_p$ | self-inductance of the transmitter coil (H) |
| $L_{p\_ANSYS}$ | ANSYS result of the self-inductance of the transmitter coil (H) |
| $L_s$ | self-inductance of the receiver coil (H) |
| $L_{s\_ANSYS}$ | ANSYS result of the self-inductance of the receiver coil (H) |
| $P_{inDC}$ | input DC power (W) |
| $P_{outDC}$ | output DC power (W) |
| $Q_{rr}$ | reverse recovery charge of the freewheeling diode (C) |
| $R_L$ | equivalent load resistance (Ω) |
| $R_p$ | the equivalent series resistance of the primary (Ω) |
| $R_s$ | the equivalent series resistance of the secondary (Ω) |
| $S_V$ | scaling factor (-) |
| $V_{Cp}$ | the voltage on the primary resonant capacitor (V) |
| $V_{Cs}$ | the voltage on the secondary resonant capacitor (V) |
| $V_F$ | forward voltage drop of the freewheeling diode (V) |
| $V_{actual}$ | actual value of the output voltage (V) |
| $V_{c\_max}$ | the output voltage corresponding to the maximal value of control error (V) |
| $V_{c\_min}$ | the output voltage corresponding to the minimal value of control error (V) |
| $V_{fwd}$ | forward voltage drop of rectifier diode (V) |
| $V_{inDC}$ | input DC voltage(V) |
| $V_{outDC}$ | output DC voltage (V) |
| $V_{target}$ | the target value of the output voltage (V) |
| $\hat{Z}$ | input impedance (Ω) |
| $c^{(j)}$ | j-th control error value (-) |
| $e^{(j,i)}$ | j-th control error for the primary cell current control loop in i-th iteration (A) |
| $k_{ANSYS}$ | ANSYS result of the coupling coefficient (-) |

| | |
|---|---|
| $t_a^{(j-1)}$ | measured value of the input current for the (j-1)-th control error (A) |
| $t_d^{(j)}$ | the target value of the input current for the j-th control error (A) |
| $t_{delay}$ | delay between receiving the control error and starting the regulation process (ms) |
| $t_{dt}$ | deadtime (s) |
| $t_f$ | fall time during switching of a MOSFET (s) |
| $t_{inner}$ | time required to execute a single iteration within the current control loop (ms) |
| $t_r$ | rise time during switching of a MOSFET (s) |
| $\phi_M$ | mutual magnetic flux (Wb) |
| $\phi_T$ | the magnetic flux generated by the transmitter coil (Wb) |
| $\eta_{DC-DC}$ | DC-DC efficiency of the IPT system (-) |
| $\omega_0$ | resonant angular frequency (rad s$^{-1}$) |
| $\Delta P_{ESR}$ | power losses within the primary and secondary resonant circuits (W) |
| $\Delta P_{Rds(off)}$ | forward losses of MOSFET when turned off (W) |
| $\Delta P_{Rds(on)}$ | forward losses of MOSFET when turned on (W) |
| $\Delta P_{cond}$ | conduction losses of a single MOSFET (W) |
| $\Delta P_{inv}$ | power losses of the full-bridge inverter (W) |
| $\Delta P_{rr}$ | power losses of a reverse recovery freewheeling diode (W) |
| $\Delta P_{sw}$ | switching power losses of a single MOSFET (W) |
| $\Delta P_{tot}$ | total power losses of the IPT system (W) |
| $D$ | derivative term of the PID regulator within the current control loop (A) |
| $I$ | integral term of the PID regulator within the current control loop (A) |
| $M$ | mutual inductance (H) |
| $P$ | proportional term of the PID regulator within the current control loop (A) |
| $Q$ | quality factor (-) |
| $R$ | electrical resistance ($\Omega$) |
| $f$ | frequency (Hz) |
| $f_{mod}$ | modulated frequency (Hz) |
| $f_{op}$ | operating frequency (Hz) |
| $k$ | coupling coefficient (-) |
| $\nu$ | controlled variable value within the current control loop (-) |
| $\omega$ | angular frequency (rad s$^{-1}$) |

## Abbreviations

| | |
|---|---|
| ABS | Acrylonitrile Butadiene Styrene |
| ACK | Acknowledged |
| ADC | Analog-Digital Converter |
| ASK | Amplitude Shift-Keying |
| ATN | Attention request |
| BMS | Battery Management System |
| CAN | Controlled Area Network |
| CC | Constant Current |
| CE | Control Error |
| COMP | Comparator |
| CPT | Capacitive Power Transfer |
| CV | Constant Voltage |
| DAC | Digital-Analog Converter |
| DFOC | direct FOC |
| EMC | Electromagnetic Compatibility |
| EPP | Extended Power Profile |
| ESR | Equivalent Series Resistance |

| | |
|---|---|
| EUROC | European Rocketry Challenge |
| FEMM | Finite Element Method Magnetics |
| FHA | First Harmonic Approximation |
| FSK | Frequency Shift-Keying |
| HAL | Hardware Abstraction Layer |
| HI | High |
| HRTIM | High-Resolution Timer |
| HW | Hardware |
| IC | Integrated Circuit |
| IPT | Inductive Power Transfer |
| LCC | inductor-capacitor-capacitor topology |
| LCL | inductor-capacitor-inductor topology |
| LDO | Low Dropout |
| LO | Low |
| MCU | Microcontroller Unit |
| NAK | Not Acknowledged |
| ND | Not Defined |
| PC | Personal Computer |
| PCB | Printed Circuit Board |
| PID | Proportional-Integral-Differential |
| PP | Parallel-Parallel topology |
| PS | Parallel-Series topology |
| SP | Series-Parallel topology |
| SS | Series-Series topology |
| SW | Software |
| UART | Universal Asynchronous Receiver-Transmitter |
| VA | Volt-Ampere |
| WPC | Wireless Power Consortium |
| WPT | Wireless Power Transfer |
| ZPA | Zero Phase Angle |

# APPENDIX B LIST OF ISSUES

During the implementation and testing phase, several issues were encountered because of design flaws. These errors were documented to facilitate future enhancements in a possible next version of the wireless charger.

## B.1 Issue #1: The Isolated Cathode of LED7

**Description**: The cathode of LED7 in a Transmitter PCB was not connected with the common ground. During drawing of schematics, the LED7 ground was not connected to the ground so the cathode pad did not merge with the common ground plane.

**Solution**: The pad was connected with the ground using an additional wire.

## B.2 Issue #2: The Position of the Current Sense

**Description**: The current measured on the Transmitter is fluctuating due to the current sense position. The shunt resistor is placed before the capacitors which are charged and discharged with fast current peaks.

**Solution**: Ideally, the current sense should be placed after the capacitors, or an input LC filter should be added. However, due to time constraints, the solution was to measure multiple samples and average them to increase the stability of the measurement. This solution lengthens the time needed for a credible measurement and reduces the resolution for measuring fast transients. However, this is not the intended purpose of the current measurement, and a comparator protects the components in case of rapidly increasing current, such as a short circuit in the resonant circuit. The time needed for a single measurement was experimentally measured at 8 microseconds. Therefore, in high priority intervals, taking 10 measurements and averaging them is a short enough time which ensures the trustworthy measurement and avoids overloading the processor with interrupts.

## B.3 Issue #3: Current Sense Amplifier Selection Error

**Description**: The selected Current Sense amplifier (AT1 in both the Transmitter and Receiver) supports input common-mode voltages from -0.2 V to +26 V. However, the actual common-mode voltages are +48 V in the case of the Transmitter and +30 V in the case of the Receiver. The issue was registered when the transmitter was tested with input voltage gradually increasing from +20 V to the nominal value +48 V. The output of the amplifier suddenly changed to a saturation value of +3.3 V at voltages close to the nominal value. Luckily, the MCU input pin was not damaged.

**Solution**: The amplifiers AT1 were changed for MCP6C02 current sense amplifier with a correct common-mode input range from +3 V to +65 V. The amplifier is sold in the same package and also with the same pad location as the original INA181.

## B.4 Issue #4: FSK Preprocessing Circuit Error

**Description**: In this issue a similar problem occurred as in the case of Issue #3. The input common-mode voltage range of the FSK Preprocessing comparator IC1 within the Receiver (see Fig. 33**)** was too small for this application. The comparator was damaged and had to be replaced but first, the FSK Preprocessing circuit had to be adjusted.

**Solution**: The circuit was adjusted as depicted in the Fig. B-1**.** In the current version of the Receiver PCB the soldering pads remaining of the components left were used and the IN- pin of the IC1 was connected to ground with additional wire. The adjusted circuit works as follows. The capacitor C24 connected to one terminal of the Receiver coil is charged through the R6 and of the diodes to and transform the signal to a signal with peak values ±15 V. Next, the signal peak values are transformed to ±threshold voltage of the diodes. Because the comparator VCC- is connected to the ground the resulting signal is in the range +VCC, GND where VCC is +3.3 V.
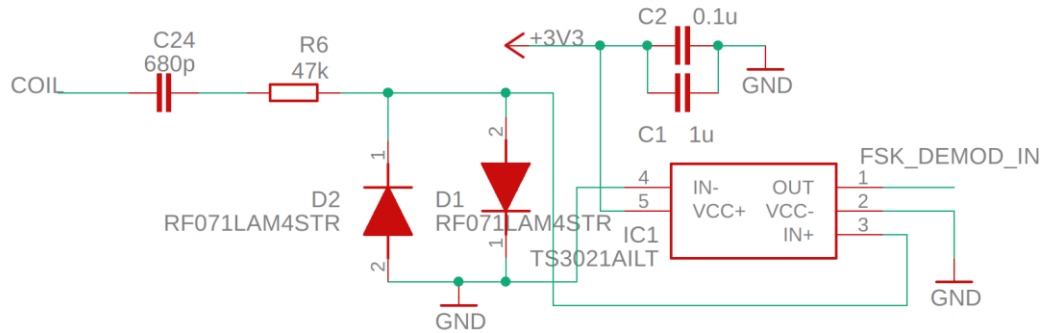
Fig. B-1 The Improved FSK Preprocessing circuit

Another solution would be to keep the current FSK Preprocessing circuit and change the IC1 to a comparator with differential inputs with input voltage ranges compatible with the voltage present on the Receiver coil. However, the proposed solution worked well so no further adjustment needs to be made.

## B.5    Issue #5: Large ESR of the Rewound Coils

**Description**: During the process rewinding coils, one more pair of coils were rewound. For this pair, a thinner ferrite pad was used from the coil 760308101141 from WE. The ferrite pad thickness was 1 mm instead of 3.2 mm. The windings of these coils were the same as the coils mentioned in 4.4.1. However, the PCBs on which the coils were placed and to which they were glued were different.

The PCBs where on the bottom side was the temperature sensor were filled with the cast copper in the middle to transfer heat from the ferrite pad to the temperature sensor on the other side and the copper cast was also on the edges of the PCBs.

The DC-DC efficiency was measured across the whole operational range and the results can be seen in Fig. B-2 with comparison to the coils with the thicker ferrite pad which were used in the final design.
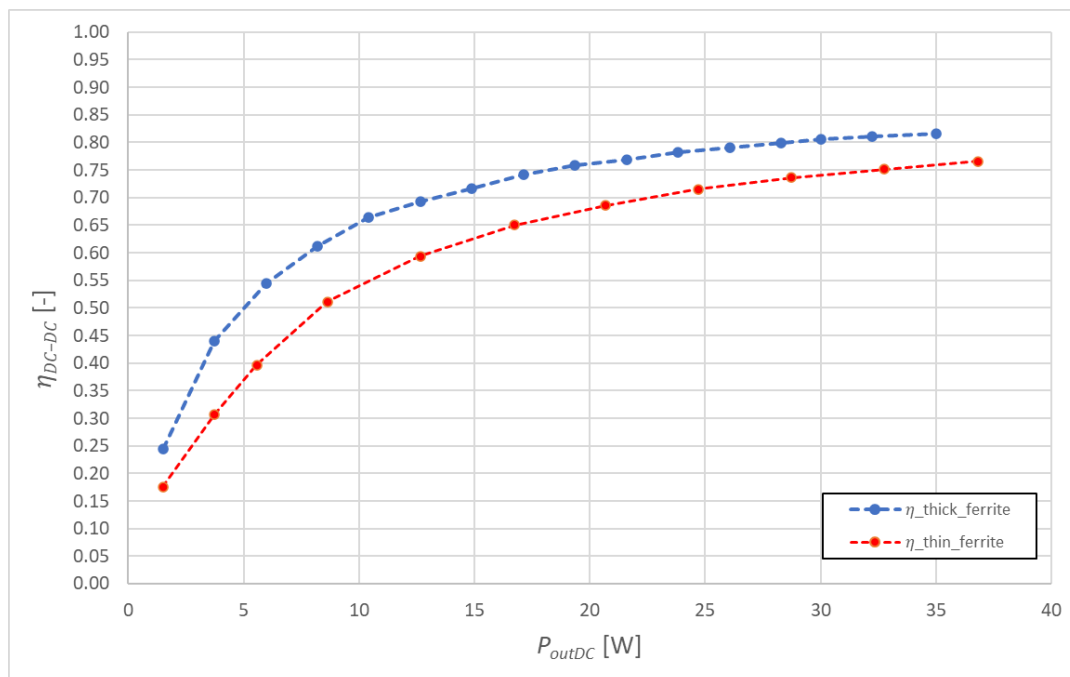


Fig. B-2 Comparison of the measured DC-DC efficiency of the original coil with the thick ferrite pad (the blue line) and the coils with a thin ferrite pad (the red line).

We can see that the measured DC-DC efficiency is much lower than in the case of the coils with the thicker ferrite pads. The reason for such low efficiency is most probably the combination of the thin ferrite pads and the copper cast within the PCB. The thin ferrite as was described in 2.3.1.3 causes increased core losses and lower coupling coefficient. The copper cast acts as a conductive pad under the coil pad which increases the eddy current losses.

**Solution**: Because the overall weight of the Receiver was approximately 103 g which is more than twice less than the maximum which was set in the requirements (see 1.3), it was decided to use the coils with the thicker, heavier ferrite.

## B.6      Issue #6: ASK Demodulator

**Description**: The ASK modulation and demodulation did not work properly for the whole operational range as stated in the requirements. Switching of capacitors C11 and C12 (within the Fig. 29 (a)) during ASK modulation caused too large voltage ripple of output voltage reaching up to 10 V for low output power. Additionally, the ASK Demodulation did not work properly for low output power. The modulated amplitude was attenuated causing the incorrect demodulation of the signal.

The figure Fig. B-3 depicts a voltage ripple of the output voltage (green) during the transmission of a control error data packet from the Receiver to the Transmitter using ASK modulation. The blue signal is measured on the ASK Demodulator corresponding to pin 10 (ASK_DBG) within the IC3 in Fig. 29 (b). This signal is the input to the final comparator which only transfers the signal to a square wave signal with maximum and minimum values of +3.3 V and 0 V respectively as described in 4.5.1.

We observe that for lower output power, the output voltage rises slowly to a steady value that is not reached by the end of the data packet. However, for higher output power, the steady value is reached since it is lower than the steady value in case of Fig. B-3 (a).



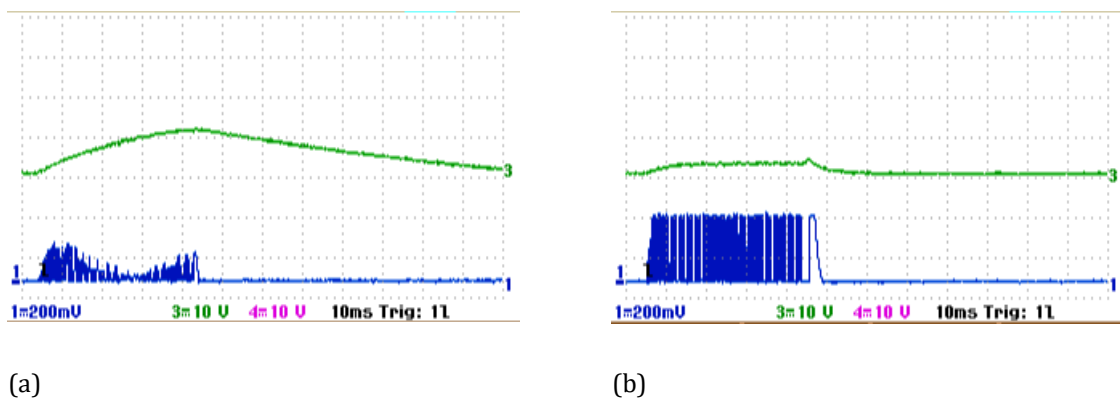(a)                                                        (b)

Fig. B-3 Attenuation within the ASK Demodulation Circuit for (a) 1.5 W of output power (b) 30 W of output power. The green line is the output voltage ripple and the blue line is the ASK_DBG signal from Fig. 29 (b).

**Solution:** The steady value of the output voltage is determined by the capacitance of C11 and C12. To reduce the steady value, the capacitance of these capacitors had to be lowered. However, the capacitance had to be at least large enough to allow the ASK demodulator to detect changes in amplitude. To achieve a best compromise between voltage ripple and the stable function of the ASK demodulator, three parallel capacitors of 1 nF each, giving a total of 3 nF, were used to replace the original 10 nF C11 and C12 capacitors.

Lowering the capacitance of C11 and C12 required adjusting the final comparator threshold voltage within the ASK demodulator. This was accomplished by changing the R35 resistor from 300 Ω to 60 Ω, which changed the threshold value from 116 mV to 24 mV. Since the comparator is located after the low-pass filter, the signal needed to be removed from possible distortion from

the surroundings. Lowering the threshold value did not cause any problems in detecting false signals.

However, the problem of unrecognizable amplitude modulation at certain conditions persisted. Several experiments and simulations were conducted in LTSpice to identify the possible cause. It was discovered that the loss in amplitude during modulation was due to capacitor C4 within the ASK Demodulator. Initially, the capacitor was replaced with one of lesser capacity, but it was found that the demodulation worked best if the capacitor was not present at all. The absence of C4 did not cause any further problems in demodulation.

## B.7    Issue #7: Damaged Soldering Pad

**Description**: During the testing of the constructed device one of the electrolytic capacitors within the Output Filter of the Receiver (C20) was often replaced with a capacitor with larger capacity and otherwise to test the output voltage ripple. The soldering pad was damaged resulting in a short circuit between the output of the rectifier and the ground. The short-circuit did not cause any damage since it only keeps the voltage from the secondary resonant circuit at zero, however this fault had to be resolved.

**Solution:** The conductive pad leading to the damaged pad was interrupted and the pad was taped over with insulating tape for transformers. A replacing wire was soldered to the rectifier output on one of the Schottky diodes pads and the pad of the capacitor. The capacitor was then glued to the same place as before with the second pad undamaged. The result can be seen in Fig. C-2 (a), at the bottom right of the picture.

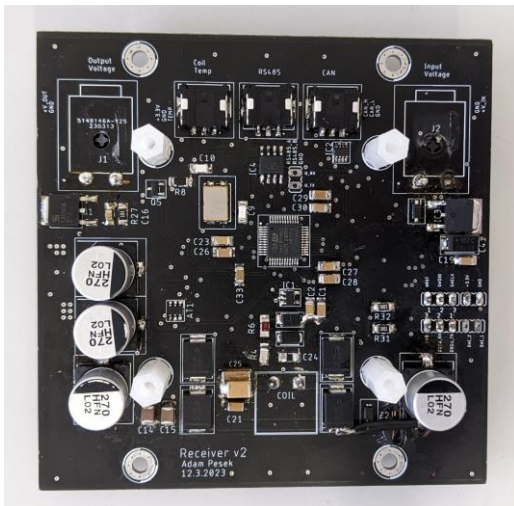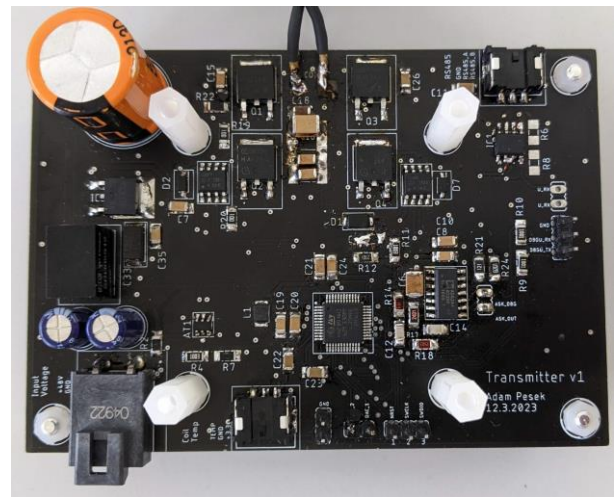# APPENDIX C PICTURES OF THE CONSTRUCTED WIRELESS CHARGER
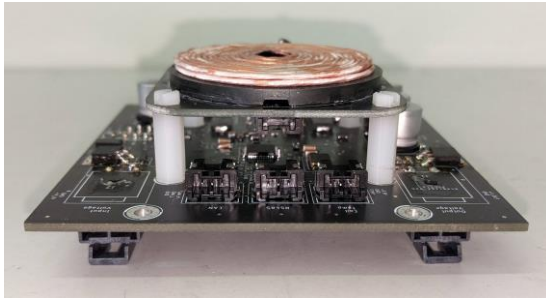


(a)
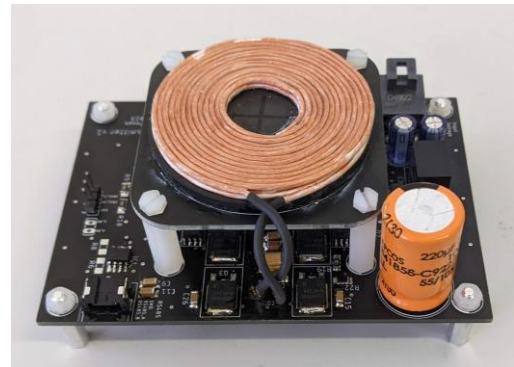


(b)

Fig. C-1 Side view of the realized wireless charger where (a) is the Receiver and (b) is the Transmitter.
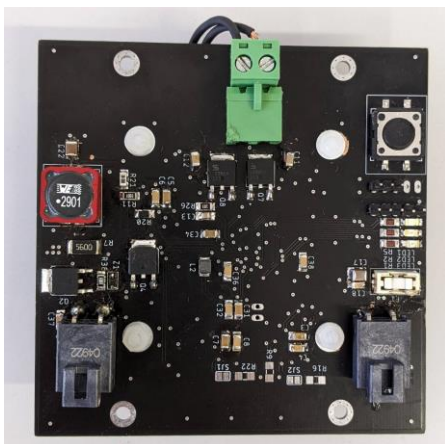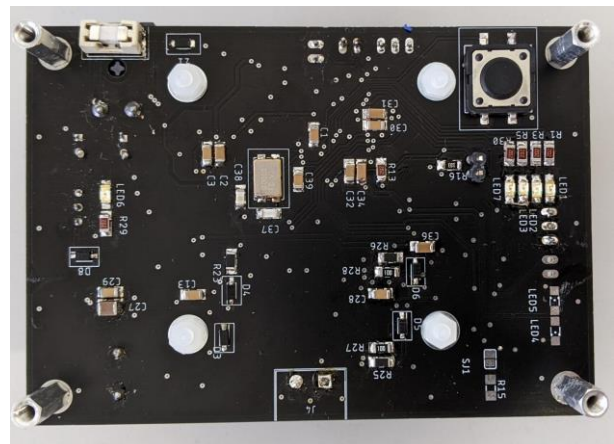


(a)



(b)

Fig. C-2 Top view of the bottom PCB of the realized wireless charger where (a) is the Receiver and (b) is the Transmitter.



(a)



(b)

Fig. C-3 Bottom view of the bottom PCB of the realized wireless charger where (a) is the Receiver and (b) is the Transmitter.

# APPENDIX D ADDITIONAL APPENDIXES

The additional appendixes consist of the following:

1. The Eagle files of the designed Wireless Charger (Transmitter, Receiver, Coil Pads) – concerning both the schematics and the PCB layout.
2. Full version of schematics in the form of the A3 format (pdf).
3. Gerber data of the designed PCBs.
4. The full code of the Transmitter and the Receiver. The code is provided in the form of two separate Keil projects, one for the Receiver and the second for the Transmitter. The projects contain all the necessary files needed to build the project as well as the STM32CubeMX initialization files.

These appendixes are not part of this document but are free to view in separate files.